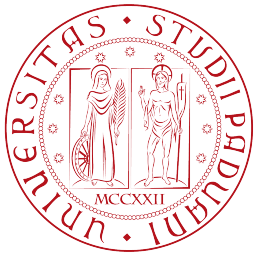

Università degli studi di Padova

DIPARTIMENTO DI SCIENZE CHIMICHE

Corso di laurea magistrale in Chimica / LM-54

TESI DI LAUREA MAGISTRALE

Exciton Topology and Dynamics in CdSe Clusters: Effects of Ligands and Aggregation from Electronic Structure Computation

Relatrice

Prof.ssa Barbara Fresch

Controrelatore

Dott. Stefano Casalini

Candidato

Pietro De Checchi

1206956

Anno Accademico 2019/2020

Acronyms and Abbreviations

Compounds abbreviations

Abbreviation	Chemical Formula
Cd4	$[Cd_4(SePh)_6Cl_4]^{2-}$
Cd8	$[Cd_8Se(SePh)_{12}Cl_4]^{2-}$
Cd10	$Cd_{10}Se_4(SePh)_{12}(PPh_3)_4$
Cd13	$Cd_{13}Se_{13}$
Cd17	$[Cd_{17}Se_4(SePh)_{24}(PPh_2Pr)_4]^{2+}$
DTMT	2,5-di-(dithiolmethyl)-thiophene
PDTC	phenyl-dithiocarbamate
PPNS	2-(dithiol-methyl)thieno-[4,5-f]-N-methyl-isoindole-5,7-dione
4D	$[Cd_4(SeMe)_6Cl_3DTMT]^{2-}$
8D	$[Cd_8Se(SeMe)_{12}Cl_3DTMT]^{2-}$
10D	$[Cd_{10}Se_4(SeMe)_{12}(PMe_3)_3DTMT]^{-}$
13D	$[Cd_{13}Se_{13}DTMT]^{-}$
17D	$[Cd_{17}Se_4(SeMe)_{24}(PMe_3)_3DTMT]^{+}$
8P	$[Cd_8Se(SeMe)_{12}Cl_3PPNS]^{2-}$
17P	$[Cd_{17}Se_4(SeMe)_{24}(PMe_3)_3PPNS]^{+}$
d.4D	$[(Cd_4(SeMe)_6Cl_3)\text{-}\mu DTMT\text{-}(Cd_4(SeMe)_6Cl_3)]^{4-}$
d.8D	$[(Cd_8Se(SeMe)_{12}Cl_3)\text{-}\mu DTMT\text{-}(Cd_8Se(SeMe)_{12}Cl_3)]^{4-}$
d.10D	$[(Cd_{10}Se_4(SeMe)_{12}(PMe_3)_3)\text{-}\mu DTMT\text{-}(Cd_{10}Se_4(SeMe)_{12}(PMe_3)_3)]^{2-}$
d.13D	$[(Cd_{13}Se_{13})\text{-}\mu DTMT\text{-}(Cd_{13}Se_{13})]^{2-}$
d.17D	$[(Cd_{17}Se_4(SeMe)_{24}(PMe_3)_3)\text{-}\mu DTMT\text{-}(Cd_{17}Se_4(SeMe)_{24}(PMe_3)_3)]^{2+}$
d.8P	$[(Cd_8Se(SeMe)_{12}Cl_3)\text{-}\mu PPNS\text{-}(Cd_8Se(SeMe)_{12}Cl_3)]^{4-}$
d.H	$[(Cd_8Se(SeMe)_{12}Cl_3)\text{-}\mu SPPN\text{-}(Cd_{17}Se_4(SeMe)_{24}(PMe_3)_3)]^{-}$

Acronyms

Acronym	
1TDM	One-electron Transition Density Matrix
CI	Configuration Interaction
CIS	Configuration Interaction Singles
CDD	Charge Density Difference
CQD	Colloidal Quantum Dots
CT	Charge Transfer Character
DFT	Density Functional Theory
DOS	Density of States
ECP	Effective Core Potential
EA	Electronic Affinity
EDL	Exciton Delocalising Ligand
ET	Electron Transfer
EET	Excitation Energy Transfer
EMA	Effective Mass Approximation
GGA	Generalised Gradient Approximation
HF	Hartree-Fock
ICT	Inverse Charge Transfer
IE	Ionization Energies
KS	Kohn-Sham
MSC	Magic-Size Cluster
MO	Molecular Orbital
NTO	Natural Transition Orbitals
OEDM	One-electron Density Matrix
PDOS	Projected Density of States
PR	Participation Ratio
QD	Quantum Dot
SCF	Self-Consistent Field
SE	Schrödinger Equation
SVD	Single Value Decomposition
TD	Time Dependent
TD-DFT	Time Dependent Density Functional Theory
TDSE	Time Dependent Schrödinger Equation
TDOS	Total Density of States

Contents

Introduction

Semiconductor nanostructures are characterised by a wealth of interesting features, such as unique optical and electrical properties which can be easily tuned by controlling quantum confinement effects. Because of this, they are a central topic of investigation for several disciplines: chemistry and physics above all, and material science, engineering, medicine and, more recently, information science. The application field is wide, spreading from innovative photovoltaic panels aimed to overcome Shockley–Queisser limit,[1–4] light-emitting devices,[4, 5] non-classical light sources,[6] biological fluorescence marker,[7] quantum information devices[8–15] and quantum neural networks.[16–18]

Colloidal quantum dots (CQD) and sub-nanometer clusters are promising building blocks for nano-structured architectures for all these applications. Because of their fully quantized electronic structure, quantization of charge, robustness and tunability they have been often compared to "artificial" atoms. However, to be useful for applications, these building blocks need to be assembled and the opto-electrical properties of quantum dot materials are influenced by mutual interdot interactions.

A key point to investigate, which is also the main subject of this thesis, relates to the nature and magnitude of interactions between individual nanostructures and how protecting ligand can be used to control and improve such interactions.

Extensive studies have been done on these systems, both experimental and theoretical.[19] In experimental studies, various techniques are employed for characterisation, imaging and investigation of properties and behaviour. Among these, optical spectroscopies are by far the most important and used.[20–23]

From the theoretical point of view, the description of these systems poses several challenges due to the intermediate scale they represents, lying between

the molecular and solid-state (macroscopic solid) regimes.

Physicists and materials scientists usually use a top-down description, approaching the system as a tiny piece of solid bulk material. Chemists, on the other hand, prefer to describe them as big molecules following a bottom-up approach, conceptually related to the synthetic strategies.

Before introducing the methods used in this work, a brief overlook of the most common theoretical approaches used to predict the properties of semiconducting quantum dots is given.

The most important top-down theory is the effective mass approximation (EMA), because of its simplicity together with the ability to efficiently describe most of the experimental results. The base of this method is to consider the motion of a "free" electron, recovering the contributions due to inter-electron interactions using an *effective mass* m^* for the excited electron and for the hole that it leaves in the valence band. This gives rise to a parabolic profile of the energy as a function of the momentum $\mathbf{p}$ of the particle. Then potential barriers are added to confine the movement of electrons in all three dimensions, giving rise to only discrete energy levels on the parabolic band, hence the energy bands converge to atom-like energy states.

This phenomenon is the essence of *quantum confinement* due to the small size of the system. This approach recalls the solution of the particle-in-a-box, and indeed it is, with the difference that the potential is given as an infinite spherical well. Then the solution of the one-particle Schrödinger equations of the radial function associated with each of the particles gives consistently eigenfunctions and eigenvalues.

The major limitations of this method (and the closely related $\mathbf{k}\cdot\mathbf{p}$ method) are: (i) it does not consider at all the surface of the nanostructures which is depicted simply as a potential barrier that is not "flexible" and does not have a chemical structure.[24], (ii) its physical accuracy is reliable only for systems closest to the reference used ($\mathbf{\Gamma}$ point of Bruillon zone of the infinite crystal) and for relatively large sizes (for CdSe QDs it works well for diameter larger than 6-7 nm), (iii) it does not consider shape-dependent features, on the contrary, a spherical symmetry has to be used as an assumption and nevertheless (iv) it was

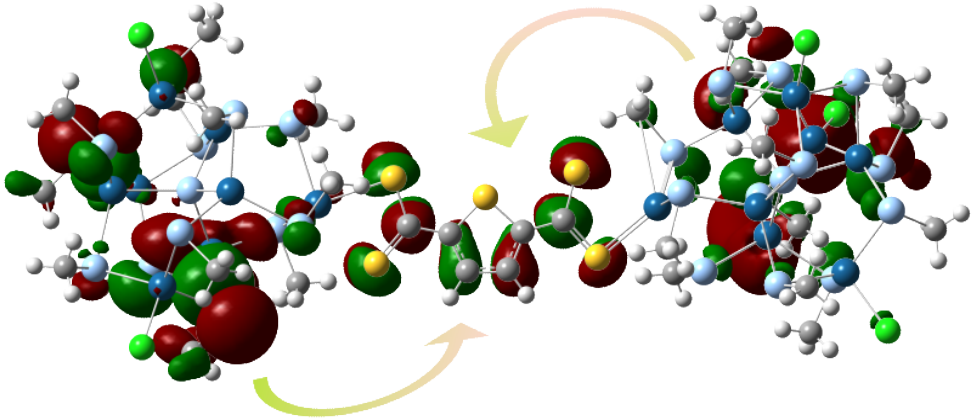

Figure 1: An example of the electron density change upon excitation, as the sum of two particular configurations.

considered the main, not to say the only, theory until the last twenty years (the *Standard Model*), Whereas points (i) to (iii) are clear limitations of this approach, the last point is mentioned because for quite a long time the EMA approach was considered sufficient for the description of quantum dots so hampering the development of other, complementary, methods.

The theoretical bottom-up approaches relied mostly on the use of semi-empirical and plane-wave methodologies. The former is a strongly system-dependent method relying on the good parameterization of the problem and nowadays it is used in tandem with a higher level of theory study to address a specific problem. The latter is more recent and it is based on a particular implementation of the density functional theory (DFT), firstly developed to deal with bulk or very large systems, i.e. in the order of hundreds to thousands of atoms, especially in the field of materials science.

In this thesis we want to focus on interface effects on the electronic structure of CdSe clusters: the interface between the inorganic core and organic ligands and the interface between different clusters. We do so through all-atom electronic structure calculation by DFT using local Gaussian basis, the use of qualitative and quantitative descriptors of the nature of the electronic states, visualisation of the optical transitions through an optimised combination of orbitals for hole and electron and the numerical solution of the time-dependent Schrödinger equation (TDSE).

As aforementioned *"the properties of nanostructured materials are influenced*

by the interactions between individual QDs, between inorganic cores and their organic ligands and their environment". The smallest form of aggregation we can treat is a dimer of nanostructures which, besides being small enough to be calculated with atomistic resolution, is demonstrative of the interactions between first neighbours. The main research question investigated in this work concerns how QDs interact in dimers.

Specifically, to what extent organic exciton delocalising ligands mediate the interaction? How they influence the electronic structure of monomers and dimers? How the presence of a second inorganic core modifies the properties of a cluster? Are excited states delocalized over multiple clusters?

A visual example of excitonic delocalisation, and anticipation of the work, is presented in fig. 1: the isosurface represents the transition density between the ground and a selected excited state in a dimer of clusters connected with a special organic linker. While the hole state is delocalized among the two inorganic cores the electron is localized on the ligand. This excitation describes a photoinduced charge displacement from the cores to the linker.

We investigate a particular series of homologous cadmium selenium (CdSe) clusters, first experimentally studied by Soloviev in [21], which are sub-nanometer to nanosize clusters that can be treated computationally. We assemble dimers using two different bridging ligands, one symmetric and one as a prototype of possible intrinsic push-pull organic likers, to enhance charge transfer features between monomers and the ligand itself and in a heterodimer system.

Organization of the Thesis

To conclude this introduction we give an overview of the organization of the work. In Chapter 1 we describe separately the chemical building blocks which will then be used to build the systems we want to analyse. The clusters of the series under investigation are introduced, with their structural characteristics and their optical behaviour. The organic ligand shell protecting these clusters and its effects are taken into account with a special focus on the influence on the excitation behaviour of the inorganic core. The properties of a particular class of known exciton delocalising ligands are investigated and in Section 1.3 we

propose two bridging ligand molecules: one as a variants of a well known exciton delocalizing ligand and the other as a model of a push-pull system to enhance charge transfer between two clusters in a dimer configuration.

The theoretical tools we use to address the description of our systems, that is the basis of DFT, TD-DFT and the ways to manipulate the transition density matrix to obtain indexes to describe the excitation and to visualise them are presented in Chapter 3.

Following these premises, the results of the analysis of the topology of the excitation are reported and discussed in Chapter 4. In this Chapter we focus on (i) the homologous series of clusters: $[Cd_4(SePh)_6Cl_4]^{2-}$, $[Cd_8Se(SePh)_{12}Cl_4]^{2-}$, $Cd_{10}Se_4(SePh)_{12}(PPh_3)_4$ and $[Cd_{17}Se_4(SePh)_{24}(PPh_2Pr)_4]^{2+}$; (ii) the clusters interacting with two special ligands; (iii) dimers built by connecting two clusters by one special ligand.

As a final point, in Chapter 5 we study the unitary dynamics of a coherent superposition of different electronic states created by the interaction with a laser pulse.

Main Results of the Work

This work is related to a first characterization of the exciton topology in dimers of CdSe clusters which was recently published (Coden, De Checchi, Fresch, Nanoscale, 2020,12, 18124-18136).[25] By using substantially the same methodologies we expanded considerably the scope and the findings of that original work. In particular:

1) We introduce two ligands (DTMT and PPNS, see Chapter 2) showing a remarkable capability of forming charge transfer states when interacting with CdSe clusters. Charge transfer states are important as a first step for charge migration and we expect these ligands to be potentially interesting to enhance carrier mobility in cluster aggregates.

2) Despite the capability of the chosen ligands of moving charges from the semiconducting core, we find that clusters in dimers are only weakly interacting, which highlights the isolating role of the capping ligand shell of the CdSe clusters.

3) We also found another mechanism which reduces electronic coupling in

dimeric structures that we might call "*localization upon aggregation*". Intuition would suggest that the presence of a ligand which delocalise exciton density in an isolated cluster would be also effective in increasing coupling among two clusters connected by the same ligand. We found this expectation is not always true and observe that the exciton density tends to localize back to the inorganic core upon cluster aggregation. The effects of this mechanism on the mobility of charge carriers deserve further investigations.

4) Through the analysis of the "chemical building blocks" at our disposal, we design an effective donor-acceptor heterodimer which is promising for supporting photoinduced charge separation.

Programs

All calculations of electronic structures have been performed using Gaussian16 package,[26] on the C_3P (Computational Chemistry Community in Padova) HPC facility of the Department of Chemical Sciences of the University of Padova. All calculations of indexes are performed with the TheoDORE package.[27] Gaussian16 output have been manipulated mostly with Python personal scripts and programs, and Multiwfn.[28] The dynamics and the final density differences files have been produced by personal scripts.

Chapter 1

Chemical Building Blocks

In this Chapter, the Cadmium Selenide clusters under investigation will be introduced. They are our chemical building blocks which can be ideally connected by bridging ligands to form dimers of nanostructures and even more extended systems. To investigate the key aspects influencing the interactions and the optical properties of aggregates, we will focus on several clusters and bridging ligands.

1.1 The Series of Cadmium Selenide Clusters

A variety of sub-nanometer clusters of semiconducting materials can be synthesised. Similarly to their bigger cousins, i.e. the colloidal semiconducting quantum dots, they are characterized by a core of semiconducting material capped by organic ligands. The cores differ by the choice of the elements used, their stoichiometric composition and their shape. For an exhaustive description of possible systems, synthesis and characterisation please refer to ref. [29].

Among the possible compositions, CdSe systems, a type II-IV semiconductor material, is widely used and CdSe QDs were extensively studied within the framework of EMA.[21, 30–36] Moreover, sub-nanometer CdSe clusters, capped by selenophenols, have been successfully synthesized and characterized by single-crystal X-ray diffraction and UV-Vis spectroscopy already 20 years ago.[37, 38] Since then, they have successfully demonstrated their potential in many of the applications mentioned in the Introduction chapter.[39, 40]

Bulk CdSe presents a direct band-gap of about 1.8 eV,[41] which is increased

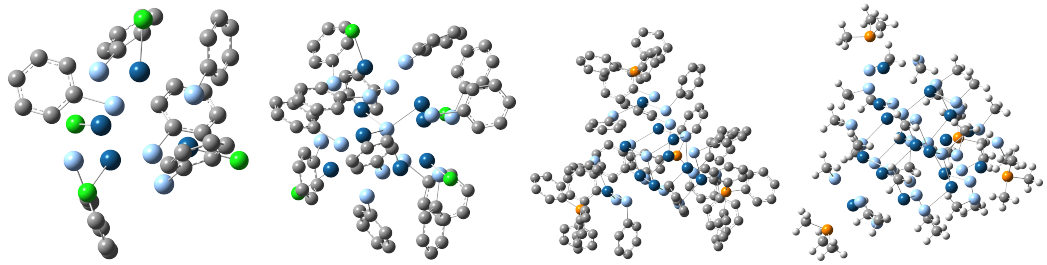

(a) (b) (c) (d)

Figure 1.1: Series of homologous CdSe clusters, from [21], optimized structures. In structure (d) all phenyl residues are replaced by methyl groups, according to the benchmark study and to ref [25]. Color code: selenium (Se) atoms in light blue, cadmium atoms (Cd) in blue, chlorine in green, phosphorus in orange, carbon in grey and hydrogen (not displayed for phenyl groups) in white.

by quantum confinement as the dimension of the system are squeezed to the nanometric scale. The range of optical absorption, red to IR in the bulk material, is therefore shifted to the UV-Vis range in QDs and clusters. The first allowed transition in the smallest CdSe crystal compound, the first among the clusters in the series we consider, is 4.2 eV (295 nm, 33875 cm^{-1}).

In this work, I will focus on the homologous series of clusters synthesised by U. Banin *et al* in [35] and further expanded in [21]. These clusters are:

- $[Cd_4(SePh)_6Cl_4]^{2-}$
- $[Cd_8Se(SePh)_{12}Cl_4]^{2-}$
- $Cd_{10}Se_4(SePh)_{12}(PPh_3)_4$
- $[Cd_{17}Se_4(SePh)_{24}(PPh_2Pr)_4]^{2+}$

here reported in fig. 1.1, and from now on addressed with the abbreviated notation **Cd4**, **Cd8**, **Cd10** and **Cd17**.

These clusters are characterized by a stable stoichiometry, they can be synthesized and isolated and their structure is known by single-crystal X-ray determination. The clusters belonging to this series share many features. The stoichiometry is uneven, approximately $Cd_{\sim 0.6}Se$ ratio for the inorganic elements, and, except for the smallest cluster, they present a central core unit: a single Se centre is the core of **Cd8**, an adamantane-like cage is the core of **Cd10**, although it marginally participates at the surface of the crystal, and a $CdSe_4$ tetrahedron is the core of

Cd17. All of the clusters belong to the same symmetry point group C_3, that can be further idealised as a tetragonal symmetry, i.e. a trigonal-based pyramid and it can be clearly seen by the presence of four apical ligands and their spatial arrangement. The apical ligands are different in these structures. The smallest clusters are stabilised by four halides, chlorine in this particular case, although it can be found with four bromides as well. The other two clusters, bigger and more regular in their internal structure, are coordinated by four triphenylphosphines (PPh_3) that, contrary to halides, bear no net charge. Notice that the total charges of these compounds are different: the first two clusters are di-anions carrying a -2 charge while **Cd10** is neutral and **Cd17** is doubly positively charged. The formal charge of the inorganic core is 2+ for all the clusters with the except for **Cd10**, that is neutral. This difference will be important later in Chapter 4 to rationalize the electron affinities of the clusters and the trend across the series.

We should mention that in the recent literature on the computational characterization of CdSe clusters, a large emphasis is given to "magic-size" clusters (MSCs) as testified by the increasing number of papers published within the last years.[42–47] "Magic-size" clusters have an even stoichiometry, i.e. Cd_XSe_X, with X such that the resulting structure is highly stable and would form preferentially over any other combination of atoms. However, while the cluster we consider are structurally well-defined, far less experimental data are available for the magic-size clusters and their actual geometries are still unclear.

Another important reason underpinning the choice of these systems as our chemical building blocks is their relatively small size, in term of number of atoms composing the core and the number of ligands, while the smallest magic size core is $Cd_{13}Se_{13}$.[47–51] In this regard, the $Cd_{\sim 0.6}Se$ homologous series gives us the opportunity to study electronic properties of real and well-characterised clusters of increasing size, which naturally presents an organic capping shell, by means of atomistic electronic structure calculation.

Nonetheless, I will also consider the smallest magic size cluster, namely $Cd_{13}Se_{13}$, for comparison because it allows us (i) testing our hypothesis in a representative of a different family of clusters, (ii) having a model for spherically shaped QDs and (iii) considering a bare CdSe core, meaning without capping ligands. In

particular, we will use $Cd_{13}Se_{13}$ as reference for the analysis of the properties of the dimers we build, because the electronic structures of $Cd_{13}Se_{13}$ dimers were previously studied in ref [25].

1.2 The Shell of Capping Ligands

As mentioned above, the presence of an organic shell is a key element in most of semiconductor nanocrystals, particularly for CQDs,[52–54] and the series under investigation is no exception. The ligands saturate the dangling bonds of the inorganic core, avoiding the formation of traps due to surface defects. As a shell, these ligands protect the clusters from coalescing towards the more thermodynamic favourable condition of bigger crystals.[55]

In the recent research on CQD, the active role of the ligand shell in determining the properties of these systems is widely recognized. From the point of view of electronic and optical properties, we can roughly recognize two wide classes of ligand: common protecting ligands - such as trioctylphosphine (TOP), trioctylphosphine oxide (TOPO), oleic acids, amines and alcohols -[52] do not have specific and strong effects.

Their main role is the stabilization of the core and the passivation of the unwanted trap states which increases the emission yield. The absorption profile, while shifted to higher energy for the opening of the gap, maintains the same feature as in the bare core. Nonetheless, exciton and electronic dynamics are influenced by the capping ligands: they mediate electron-phonon interactions, causing the dephasing of oscillating quantum coherences and the relaxation of the system by coupling to the phonon vibrations.[23, 56–58] Indeed, the stabilisation given by the organic shell is due to an effect of isolation from the environment. The interactions with the organic shell affect the inorganic core, and they resent of only small variation when the capping ligands, in turn, interact with the outer environment. One way is by the induced Debye-like relaxation. The ligand moieties act as non-interacting dipoles with the possibility of independent rotations and motion, dynamically assuring an effective dielectric response that shields from the environment dielectric constant and its possible variations.

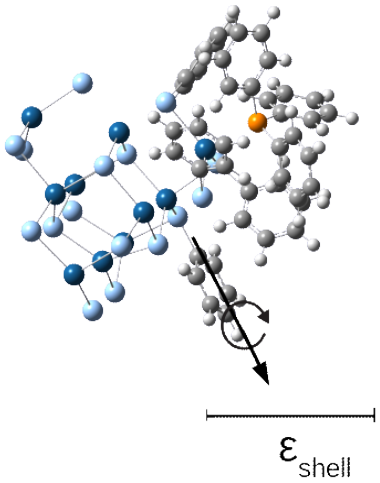

Figure 1.2: The **Cd10** cluster with only one face covered by phenyl groups, to emphasise the protective role of the organic shell. The possible rotation around the main axis is shown

The series under investigation presents all the clusters capped by phenyl groups, that can be also viewed as selenophenols when considering the Se centres as binding termination of the ligand and not part of the inorganic core.

The other family of commonly used capping molecules comprises a wide selection of thiol-based ligands. They are known for the stability of the bonding to the inorganic core and their simple use in the synthesis process. However, capping with thiolate ligands deeply affects the electronic structure of the system which reflects in a different optical behaviour. One of the main effects is the creation of surface traps which effectively quench the luminescence. Moreover, a red-shift of the absorption profile upon substitution of pristine ligands with thiol-based molecules is commonly observed suggesting these ligands influence the confinement of the excitation.

In the simple description by the approximated models of the particle-in-the-sphere and EMA, the sulfide centres increase the apparent radius of the QD, causing a red-shift because of the looser confinement of the exciton.[59–62]

From an atomistic point of view, the redshift of the absorption spectrum may arise from the delocalization of the excitonic wavefunction over the ligand shell. The extension of the wavefunction outside the semiconducting core is a key point for the design of ligands which are able to influence energy and charge transport in QD aggregates. “Traditional” ligand shells unavoidably isolate the

semiconducting core from the environment and also from adjacent nanostructures hampering an efficient "communication" among the different units. As we briefly explain in the next section, an important research effort has been devoted to the identification of ligands able to efficiently delocalised excitons and charges.

1.3 Exciton Delocalising Ligands

Starting from the evidence that thiol-based ligands strongly influence the electronic structure of the semiconducting core, important research questions arise: (i) is it possible to enhance the delocalisation of the excited states by specifically engineering ligand molecules? (ii) if this is so, does the delocalisation into the external organic shell enhance the coupling with other units of an aggregate or to other neighbouring systems?

Concerning the first point, few Sulphur-based organic molecules have been proposed as "exciton delocalising ligands".[60, 63–65] The first and most studied molecule of these class is the phenylendithiocarbamate (PDTC),[59, 63, 65–72] a bidentate anionic molecule which binds through its dithiocarbamate head to the surface metal centres of the crystals in a chelating mode. Several experimental papers report a consistent spectral red-shift upon binding of PDTC to CdSe QDs, however, the exact way this ligand acts on the electronic cloud to produce this effect is still under active investigation. Recent results show that this molecule might decompose during the process of exchange with pristine ligands during the synthesis[73] and also that other molecules binding the system with the same dithiocarbamate moiety have similar effects despite a lower mixing of interfacial orbitals modulated by different side chains.[74, 75] In a recent computational study on sub-nanometric clusters dimers connected with PDTC,[25], we indeed find that the specific backbone π-system of PDTC has a limited influence on the system compared to the bonding branch. However, other completely conjugated systems have been proved to influence delocalisation,[64, 76] especially in dimers.[25]

Besides being used as capping agents in single QD or clusters, these exciton delocalizing ligands can be used to covalently link different clusters when two bonding moieties are present on the same molecule. Using this procedure we will

build dimer of clusters and we refer to these ligands as linkers, bridge or bridging ligands. We will therefore investigate the answer to the research question (ii) above: does a linker which is able to delocalize the exciton enhance the coupling between two cores?

The intuitive idea is that molecule with good exciton delocalisation capability should act as an enhancer of the electronic coupling between units by favouring the overlap of the excitonic wavefunctions localized in each cluster. Such coupling would manifest as a red-shift of the optical absorption transitions due to the reduction of the quantum confinement (i.e. delocalized hole and electron states) or to the excitonic splitting of the localised optical transitions.

Throughout the discussion of the results in Chapter 4, we will see how the logic by which the exciton density is shared between cluster and ligand and among different units is less straightforward than what the simple intuition suggests. However, there are some general features that we expect to play a role in the enhancement of the exciton delocalisation and that we have used to choose the bridging ligand to be studied. Specifically, an efficient orbital hybridization at the surface influences the overall properties of the systems and is a good premise to exciton delocalization. Considering that we aim at enhancing the electronic communication between two separated units connected by the bridging ligand, a high delocalisation of the electronic density over the ligand seems to be beneficial and therefore we selected conjugated molecules. This characteristic generally entails another important one, the rigidity of the bridge: because of the presence of double bonds and rings, rotational degrees of freedom are constrained and therefore the perturbation effect on exciton states diminishes. Systems that are highly conjugated and planar, like those described above, generally have high polarizability, meaning that their electronic cloud promptly interacts with an external perturbation. Beyond these structural properties, it is interesting to choose molecules whose transition energy can be tuned so that the absorption due to the ligand can be designed with respect to the absorption profile of the cluster. Moreover, ligands should be either commercially available or producible by a well defined synthetic route. However, this does not have to limit the theoretical studies that aim to comprehend the inner mechanisms underlining

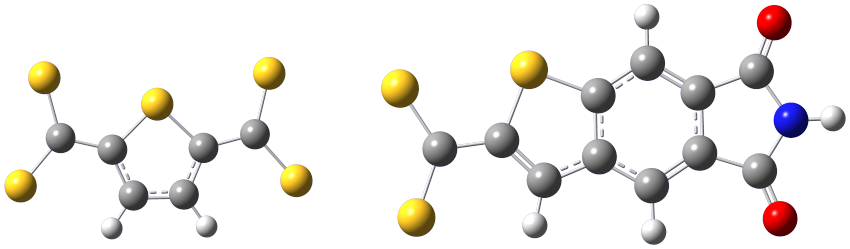

(a) (b)

Figure 1.3: Organic linkers investigated in this work. (a) 2,5-di-(dithiolmethyl)-thiophene in its di-anionic form (DTMT) and (b) 2-(dithiol-methyl)thieno-[4,5-f]-N-methyl-isoindole-5,7-dione (PPNS) in its anionic form. Color code: sulfur atoms in yellow, nitrogen atoms in blue, oxigen atoms in red, carbon in grey and hydrogen in white.

these processes. These studies often rely on drastic simplifications to emphasise the role of a particular feature of a system, whether it is the behaviour due to a single element or group, geometry or interaction, and then, after the elucidation, the obtained knowledge can be transferred to experimental fields.

Considering the previous studies on exciton delocalising ligand focused on simple aromatic rings functionalised with thiolic moieties,[25, 64, 76] we choose a similar molecule as principal bridging ligand, namely the 2,5-di-(dithiolmethyl)-thiophene molecule,[77, 78] from now on referred to as DTMT. DTMT is a thiophene ring functionalised by two dithiomethyl groups, binding similarly to the dithiocarbamate by chelating Cadmium centres of the inorganic clusters. Since the main effect attributed to the PDTC molecule is related to its binding head, with the design of this ligand we want to enhance the role of the backbone of the ligand introducing sulfur atoms in the whole bridging molecule rather than only as binding elements. Furthermore, the thiophene backbone is widely studied as it is the monomer of different semiconducting polymers,[79, 80] and could be an interesting combination for new nano-composite materials.[81]

Another bridging ligand studied in this work is the 2-(dithiol-methyl)thieno-[4,5-f]-N-methyl-isoindole-5,7-dione molecule. Unlike the previous one, this molecule has not been found in the main databases, although similar structures exist, with moieties attached in different positions.[82, 83] The idea beneath the choice of this linker comes from the use of organic push-pull systems for innovative and non-linear devices,[84–87] where the donor and acceptor units are linked together by a

conjugated bridge.

This is a simple model of an intrinsic 1D push-pull system: the dithiomethyl thiophene ring acts as the push towards the nitrogen terminal that acts as the pull and the fused aromatic ring is the core of the π-system connection. Hence, this molecule is named PPNS, staying for push-pull with nitrogen and sulfur extremities. This ligand was specifically designed to induce a precise direction into the reorganization of the electronic density upon optical excitation. Specifically, we will see how this ligand enhances the charge transfer (CT) character of the excited states of heterodimers, where two different clusters indeed become the donor and acceptor unity of a push-pull super-system. The same design could be used to enhance CT between a cluster and other systems, such as a conductive material.

Chapter 2

Excitonic Systems

Considering the intermediate nature of the systems under investigation in terms of size and composition, and bearing in mind the materials we want to understand through this modelling, we need to clarify the essential features of their excitation. Indeed, electronic excitation of nanosystems differs both from the solid-state definition of exciton and the simple molecular excitations, while sharing characteristics with both.

The problem can be tackled from the two different starting points. Here we choose to address first the solid-state description of the excitation of bulk inorganic semiconductor material and then the molecular excitation and aggregate models, to depict methodically the complex behaviour of our nanometre-sized systems, recalling when necessary features of the bulk description.

The simplest way to describe a single excitation in a bulk inorganic semiconductor material is as a transition between the valence band (VB) and the conduction band (CB). When a photon of sufficient energy $h\nu$, hence at least as the band-gap energy, is absorbed by the material, one electron changes its state from an occupied state in the VB to a virtual state in the CB. A positive charge is then left in the valence band, the *hole*, because of the presence of an empty state, and a negative charge, the actual *electron*, in present the conduction band. These two entities are interacting by the attractive Coulomb force between the two opposite charges. When the magnitude of the coupling is negligible the particles are "free carriers" and they play a major role in conventional photovoltaic devices.

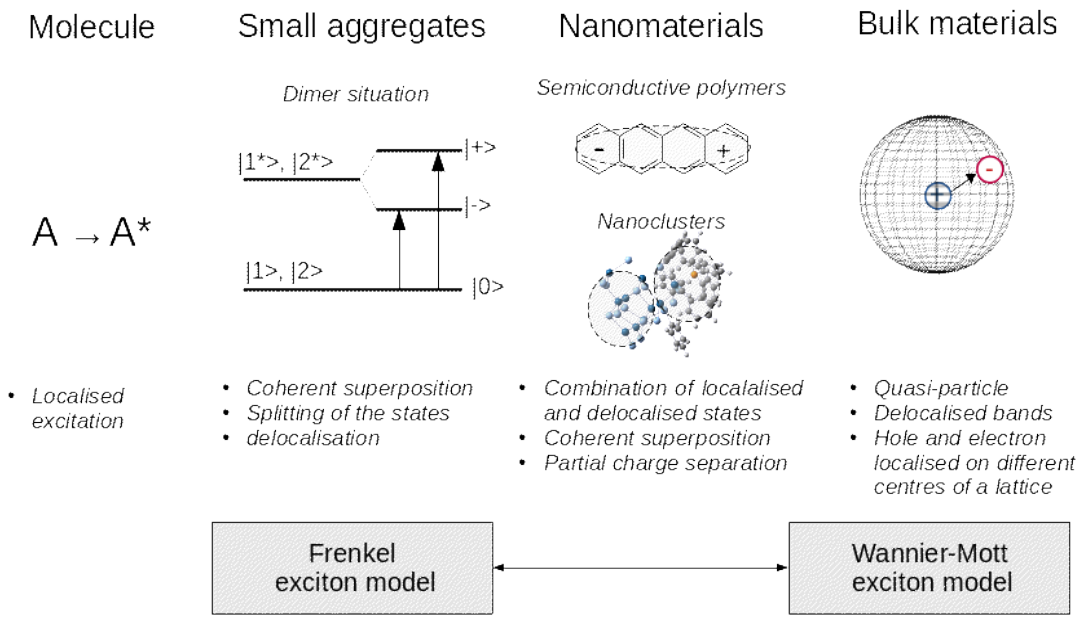

Figure 2.1: Schematic diagram of the different behaviour and approach to describe excitations in different systems. Proceeding from the molecular description we start with a localised basis, a simple excitation localised on a molecule, to the formation of combinations of localised state leading to a new basis set of delocalised states (Frenkel-excitons) to describe excited states. In the intermediate situation, characteristic of nanosized structures, it is more difficult to picture the excitation only on localised or delocalised basis sets: a combination of local excitations and charge-transfer transitions are common, without reaching a loose bounded quasi-particle situation. In bulk materials the description starts from delocalised bands, i.e. the excitation shared along all the infinite crystal, where the electron and hole may move freely and independently throughout the material, then a partial localisation through the Wannier-Mott exciton model, a quasi-particle given by the bounded hole-electron that can move along the material. When proceeding from this starting point, the intermediate situation is due to a localisation of the excitation due to quantum confinement effect. An example that differs from pure nanostructured systems is added to the intermediate situation for systems with they are often combined, to emphasize the effect of a low dielectric constant and the similar effect to the localisation of the wavefunction.

Conversely, when the coupling is strong enough the electron and the hole form a bound state called *exciton*. In an inorganic crystal, hole and electron are localised on different units of the lattice, and the exciton is called Wannier-Mott exciton: a neutral excitation 'quasi-particles' similar to a hydrogen atom, as an electron–hole pair spatially separated in the lattice.[88–90] The distance of the charges is the effective Bohr radius (a_{ex}) of the quasi-particle. The energy of the electron state is then lowered by this interaction and lies within the band-gap, the energy difference named binding energy (E_b).

This picture holds for inorganic systems with reduced dimensions until the size

becomes smaller than the Bohr radius, i.e. commonly for nano-sized structures, when a molecular-like nature might be retrieved.[91]

In the description of the excitation of ideal inorganic crystals and the subsequent discussion, we consider the crystal as a whole entity. The excitation is then completely delocalised on the crystal through the definition of the bands, considering the constituent atoms as the localised basis.

On the other hand, starting from the description of molecular excitation we move from transitions involving localised states to the delocalised systems, as we first describe a simple transition in an isolated molecule and then we consider the interaction of units upon aggregation. To depict a localised transition is prosaic. For example, in a simple organic aromatic molecule, we can use the MOs to visualise a transition that is localised on the molecule, usually as a HOMO-LUMO transition. When the molecule conjugation size increase, e.g. by the addition of sub-units, more orbitals are needed to describe the transition to eventually obtain again a band type model. The situation is more interesting, for our purpose, when two molecules interact. Provided the coupling given by the interaction of the electronic distributions of the two units is weak enough to preserve the individuality of each chromophore, the molecules form an excitonic dimer. The interaction of this dimer with a photon is no more described by transitions localized on a single unit, but by linear combination of them. In the case of a homodimer, the two excited states combine in two coherent superpositions with opposite phases ($|+\rangle$ and $|-\rangle$), symmetrically split in energy by $\Delta\varepsilon = \varepsilon_+ - \varepsilon_- = 2J$. The two different superpositions are called Frenkel excitons and their energy difference is called Davydov's splitting.[92, 93] Together with the splitting of the absorption band of the monomers into two different peaks of the dimer, because of the different phase relations, a redistribution of the transition dipole happens, which enhances the oscillator strength of one transition while lowering the other depending on the relative geometry of the arrangement of the monomers dipoles. This particular feature of these states reflects into a specific pattern in the simulated optical spectra, that helps us to identify these transitions. The excitation is coherently shared among the monomers, whereas the electron-hole pair is bounded to the same monomer in the localised basis. This influences the energy transport ca-

pacity of aggregates systems, enhancing the migration length of the excitation particle.[23, 57, 94–96]

This behaviour can be appreciated in pairs of nanoclusters and QDs as well, provided the coupling between the units to be strong enough to become competitive with the disruptive interactions - such as the intrinsic energetic disorder between neighbour units and the dynamical coupling with the environment -[97] and the same simple model as discussed by M. Kasha can be occasionally somehow retrieved.[25, 93]

Regardless, more often in these systems we fall in an intermediate situation, where it is more difficult to picture the excitation only on localised or delocalised basis sets a combination of local excitations, delocalised states and charge transfer transitions are common, without reaching the loose bounded quasi-particle situation typical of infinite crystal systems. Some other features of the delocalised bands behaviour persist, since the duality of nature of inorganic nano-clusters and their intermediate size, and multiple excitations can be eventually found, leading to intra-QD coherent states.[98]

Referring to the two units of such a dimer as A and B, a local exciton on the unit A can be written as $|h_A e_A\rangle$, meaning that both hole and electron wavefunction are described by states localised in A. Then the coherently shared exciton state $|+\rangle$ reads $|+\rangle = |h_A e_A\rangle + |h_B e_B\rangle$. In a similar fashion a complete charge transfer from A towards B state can be written as $|h_A e_B\rangle$, and many combination can be formed. The ideal limit situations for an homodimer are discussed in the next Chapter.

Chapter 3

Methodologies

To unravel the quantum-mechanical behaviour of the systems under investigation we use theoretical and computational tools based on the electron density distribution. These methods include the density functional theory, its time-dependent extension and a theoretical analysis that helps to understand how the electronic density changes upon optical excitation. The one-particle transition density matrix allows us to obtain numerical indexes describing the nature and the localization of the excitation. By means of its singular value decomposition (SVD), we also obtain the direct visualisation of the hole and electron distribution describing the excited states. In this Chapter, I briefly recall the theoretical basis of these methodologies.

3.1 Density Functional Theory

3.1.1 Introduction to *Ab Initio* Calculations of Molecular Electronic Structures

The quantum mechanical description of molecules ideally requires the solution of the Schrödinger equation for many electrons and nuclei whether in its static (eq. 3.1) or time dependent (eq. 3.2) formulation:

$$\hat{H}\Psi_n(\mathbf{r}) = E_n\Psi_n \tag{3.1}$$

$$i\hbar\frac{\partial}{\partial t}\Psi(\mathbf{r},t) = \hat{H}\Psi(\mathbf{r},t) \tag{3.2}$$

where Ψ is the wavefunction, Ψ_n any eigenvector with its eigenvalue E_n and $\hat{H}$ is the Hamiltonian operator of the system. In its general form the Hamiltonian reads:

$$\hat{H} = -\sum_{i}^{N} \frac{\hbar^2}{2m_e}\nabla_i^2 - \sum_{A}^{M} \frac{\hbar^2}{2m_A}\nabla_A^2 - \sum_{i}^{N}\sum_{A}^{M} \frac{e^2 Z_A}{\mathbf{r}_{iA}} + \sum_{i<j}^{N} \frac{e^2}{\mathbf{r}_{ij}} + \sum_{A<B}^{M} \frac{e^2 Z_A Z_B}{\mathbf{r}_{AB}} \quad (3.3)$$

the first two terms describes the kinetic energy of N electrons and M nuclei, the latter three for potential energy by Coulomb interactions between electrons and nuclei and among themselves (last two terms, repulsive).

Finding the exact solution of eq. (3.3) is an exceptionally difficult problem and several approximated methodologies has been developed: Hartee-Fock restricted and unrestricted models (RHF, UHF), configuration interaction (CI), many-body perturbation theories (MBPT, e.g. Møller-Plasset MPn) and coupled-cluster (CC) are examples of well known methodologies that can be used to handle calculation of quantum mechanical properties of small isolated molecules with high accuracy. Aforementioned methodologies suffer of an unfavourable scaling of required computational resources: HF scales as $O(N^4)$, and methods accounting for electron correlation scales with higher power of the number of electrons. Indeed, all these methods are based on the wave-function of the systems, meaning that the complete solution of eq. (3.1) requires the computation of integrals depending on $3n$ coordinates, with n the sum of electrons and nuclei particles.

In practice, these methods are hardly applicable to nanostructures and supramolecular systems. Density functional theory (DFT) is the most important and flexible method to deal with relatively bigger systems, with high accuracy and yielding the same information.

3.1.2 Foundation, Theory and Implementation of DFT

Instead of working with the wavefunction $\Psi(\boldsymbol{\tau})$, which depends on $3n$ coordinates by $\boldsymbol{\tau} \in \{\mathbf{r}^{\otimes n}\}$, DFT works with the electron density $\rho(\mathbf{r})$, a direct physical observable depending only on the three Cartesian's coordinates. Given a generic normalised wavefunction $\Psi(\boldsymbol{\tau})$, $\langle\Psi|\Psi\rangle = 1$, the electron density is obtained inte-

grating for $N-1$ coordinates and multiplying by N, where N is the total number of electrons:

$$\rho(\mathbf{r}) = N \int |\Psi(\mathbf{r}_1, \mathbf{r}_2, ..., \mathbf{r}_N)|^2 d\mathbf{r}_2 ... d\mathbf{r}_N \tag{3.4}$$

The density integrated over the entire space gives the total number of electrons N:

$$\int \rho(\mathbf{r}) d\mathbf{r} = N \tag{3.5}$$

and position and charges of nuclei of the system is recovered as well: local maxima in $\rho(\mathbf{r})$ correspond to positions and, looking back at the Hamiltonian in eq. (3.3), these points are cuspids due to the singularity arising from the division by zero. Then, the atomic number of a nucleus in $\mathbf{r}_A$ is proportional to the derivative of the spherically averaged density calculated in $\mathbf{r}_A$.

The pioneering effort to define a theory based of this observable were made by Thomas and Fermi in 1927,[99] the early days for quantum mechanics. Using fermion statistical mechanics they derived the first energetic term of the Hamiltonian, the kinetic energy of the non-interacting electron gas:

$$T[\rho(\mathbf{r})] = \frac{3}{10}(3\pi^2)^{2/3} \int \rho^{5/3}(\mathbf{r}) d\mathbf{r} \tag{3.6}$$

Whereas wavefunction-based methods uses operators, which maps two spaces of functions ($g(x) = \hat{O}f(x)$), here the T is defined as a functional: a prescription which maps a function to a number ($y = F[f(x)]$). Henceforth the name density functional theory.

The real kickoff for DFT formalism arrived in 1964, with the Hohenberg-Kohn first theorem.[100] First, let's recast the Hamiltonian, for the electron exclusively, in a even more general form:

$$\hat{H} = -\frac{1}{2} \sum_i^N \frac{\hbar^2}{2m_e} \nabla_i^2 - \frac{1}{2} \sum_{i \neq j}^N \frac{e^2}{\mathbf{r}_{ij}} + v_{ext} \tag{3.7}$$

where v_{ext} is a so-called external potential experienced by the electrons, gathering the Coulomb potential due to nuclei and other possible contributions (e.g. external fields), and defines completely the system under investigation. The

Hohenberg-Kohn existence theorem states that such external potential is determined by the the electron density $\rho(\mathbf{r})$. This leads to two strictly related consequences:

i) since $\rho(\mathbf{r})$ determines the number of electrons, it follows that $\rho(\mathbf{r})$ determines the ground state wavefunction

ii) there is a bijective correspondence between external potential v_{ext} and the ground state density $\rho(\mathbf{r})$

Since $\rho(\mathbf{r})$ is uniquely related to v_{ext}, which determines the Hamiltonian, the electron density $\rho(\mathbf{r})$ can be used as basic variable and the ground state energy of the electron system is a functional of the electron density, obtained by the following functional:

$$E_0[\rho(\mathbf{r})] = T[\rho(\mathbf{r})] + V_{ee}[\rho(\mathbf{r})] + \int \rho(\mathbf{r}) v_{ext} d\mathbf{r} \tag{3.8}$$

The second Hohenberg-Kohn theorem is the first indication of how to actually predict the electron density of a system. The density obeys a variational principle, which means that the functional attains a minimum when $\rho(\mathbf{r})$ is the true electron density of the system $\rho_0(\mathbf{r})$.

Kohn-Sham Self-Consistent Field Methodology

The implementation of Hohenberg-Kohn theories into a practical form came one year later with the Kohn-Sham (KS) equation.

First, a reference electron system of *non-interacting* electrons described by a single Slater determinant Φ_{KS} of orthonormal orbitals, having the same electron density $\rho(\mathbf{r})$ of the real system.

$$\Phi_{KS} = \frac{1}{\sqrt{N!}} det[\phi_1 \phi_2 \dots \phi_N] \tag{3.9}$$

Then, a form for the terms of of the energy functional is searched for the reference system (S). The kinetic energy is defined, within an orbital expression of the density, as:

$$T \approx T_S = \sum_i^N \langle \phi_i | -\frac{1}{2}\nabla_i^2 | \phi_i \rangle \tag{3.10}$$

$$T = \sum_i^N \langle \phi_i | -\frac{1}{2}\nabla_i^2 | \phi_i \rangle + (T - T_S) \tag{3.11}$$

where ϕ_i are Kohn-Sham orbitals. The kinetic energy of the real system T is exact just because it is given in an implicit way. In the same fashion the electron-electron interaction potential is written starting from the classical part of the interaction $J[\rho]$ of a charge distribution

$$J[\rho(\mathbf{r})] = \frac{1}{2}\int \frac{\rho(\mathbf{r}_1)\rho(\mathbf{r}_2)}{\mathbf{r}_{12}} d\mathbf{r}_1 d\mathbf{r}_2 \tag{3.12}$$

and then recovering the lost quantum mechanical contribution:

$$V_{ee}[\rho(\mathbf{r})] = \frac{1}{2}\int \frac{\rho(\mathbf{r}_1)\rho(\mathbf{r}_2)}{\mathbf{r}_{12}} d\mathbf{r}_1 d\mathbf{r}_2 + (V_{ee}[\rho(\mathbf{r})] - J[\rho(\mathbf{r})]) \tag{3.13}$$

The functional arising is then:

$$E[\rho(\mathbf{r})] = T_S + V_{ee}[\rho(\mathbf{r})] + \int v_{ext}\rho(\mathbf{r}) d\mathbf{r} + \Delta T + \Delta V \tag{3.14}$$

where the first two terms refer to the fictitious system, the third accounts for external contributions and the interaction with the nuclei and the latter two accounts for the differences between the real system and the reference. These two unknown terms are gathered together in the *exchange-correlation functional* E_{xc}.

The Kohn-Sham equation, similarly to Schrödinger equation and HF method, is then:

$$\left[-\frac{1}{2}\nabla^2 + v_{eff}(\mathbf{r})\right]\phi_i(\mathbf{r}) = \phi_i(\mathbf{r})\varepsilon_i \tag{3.15}$$

where the effective potential experienced by each particle due to the other N-1 electrons is

$$v_{eff} = \frac{\partial J[\rho]}{\partial \rho} + \frac{\partial E_{xc}[\rho]}{\partial \rho} + v_{ext} \tag{3.16}$$

This leads to a set of N one-particle KS equations which has to be calculated in an iterative self-consistent field procedure, due to the dependence of the effective potential to the KS orbitals and *vice versa*. The overall simplified procedure is then summarised in the following. In a optimisation problem the cycle is slightly more complex since the initial guesses are both the orbitals basis set and the initial geometry, which is modified to self-consistency as well.

KS-SFC Procedure

1. build a trial wavefunction as Slater determinat, eq. (3.9)
2. build the electron density
3. compute v_{eff}, eq. (3.16)
4. solve N KS equations, eq. (3.15)
5. build new density
6. recompute v_{eff} with the new density
7. repeat to self-consistency

Even though DFT might looks just a recasting of HF and others there is a key difference: the derivation hitherto does not contain approximation, it is exact. Two caveats must be pointed out to the overview so far: even if the derivation is exact, one term is unknown and thus approximations for E_{xc} must be adopted. Second, the spin issue as been ignored up to this point, but can easily handled in DFT by the addition of individual functionals for the α and β densities.

To conclude this brief overview of ground state DFT a short glance to the approach to correlation and exchange energy used in the functional employed in this work is in order. Given the following expression for the exchange-correlation functional using a so-called 'energy density' ε_{xc}, thus the problem is once again just moved to another unknown entity, another functional of the electron density.

$$E_{xc}[\rho(\mathbf{r})] = \int \rho(\mathbf{r})\varepsilon_{xc}[\rho(\mathbf{r})]d\mathbf{r} \tag{3.17}$$

Thus, approximations are now to be made on ε_{xc}. The simplest approach is called local density approximation (LDA), and it consider that the value of ε_{xc} in a point can be evaluated based on the electron density in such point, its *local* value. To carry out the calculation, it is actually split into the two components, correlation and exchange ($\varepsilon_{x/c}$). Such methods consider the density to be spatially uniform, leading to important limitation.

One of the most popular way to improve DFT is the generalised gradient approximation (GGA). These methods are widely used in chemistry because their reliability for molecular systems, where the density is far from uniform. Correlation and exchange functionals are dependent on the extent of changing of the density toward the local point, thus to its derivative. A general construction for these functionals is the following, as proposed by A.D. Becke in 1988 (B88):[101]

$$\varepsilon_{x/c}^{GGA}[\rho(\mathbf{r})] = \varepsilon_{x/c}^{LDA}[\rho(\mathbf{r})] + \Delta\varepsilon_{x/c}\left[\frac{|\nabla\rho(\mathbf{r})|}{\rho(\mathbf{r})^{4/3}}\right] \tag{3.18}$$

Depending on the truncation performed in the series of the derivatives different methods arise, as examples meta-GGA, nonseparable gradient approximation (NGA) and hybrid-GGA functionals. The latter are probably the most known, because of the efficient and popular B3LYP functional. This functional, eq. (3.19), combines LSDA exhange and correlation, B88 and HF exchange (in order a local and a non-local functionals and one arising from the application of HF methodology to KS orbitals) and Lee, Parr and Young (LYP) correlation, in which there is no correction but correlation energy is computed *in toto*.

$$E_{xc}^{B3LYP} = (1-a)E_x^{LDSA} + aE_x^{HF} + b\Delta E_x^{B88} + (1-c)E_c^{LDSA} + cE_c^{LYP} \tag{3.19}$$

Functionals belonging to this family allow to have long-range correction Indeed, one subgroup is of *range-separated functionals* (RSF). Instead of using a fixed Hartree-Fock exchange energy fraction in these methods the E_x^{HF} contribution is smoothly varied as a soft function $\omega_{RSF}(\mathbf{r}_{12})$ of the distance in the Coulomb interaction kernel $\frac{1}{\mathbf{r}}$:

$$\frac{1}{\mathbf{r}_{12}} = \frac{1-[\alpha+\beta(1-\omega_{RDF}(\mathbf{r}_{12})]}{\mathbf{r}_{12}} + \frac{\alpha+\beta(1-\omega_{RDF}(\mathbf{r}_{12})}{\mathbf{r}_{12}} \tag{3.20}$$

where the first term accounts for short-range interaction and the second for long-range. Methods with ($\alpha = 0, \beta \neq 0$) are denoted by LC before the name of the hybrid functional used, when both are non null ($\alpha \neq 0, \beta \neq 0$) its preceded by CAM.

As an anticipation, the functional used in this work after comparisons with a benchmark is a long-range corrected hybrid functional, CAM-B3LYP.

3.2 Time-Dependent Density Functional Theory

As it has been described above, DFT is essentially a ground-state theory. However, it can be extended to be used to model specific aspects of excited states too, and this extension is called time-dependent density functional theory (TD-DFT). This definition comes because the addition of a time-dependent scalar term to the Hamiltonian in eq. (3.2), to describe the interaction of the system with an optical field:

$$\hat{H}(\mathbf{r},t) = \hat{H}_0(\mathbf{r}) + \hat{V}(\mathbf{r},t) \tag{3.21}$$

where $\hat{V}(\mathbf{r},t) \propto \mathbf{E}(\mathbf{r},t)$, a time-dependent linear electric field written as:

$$\mathbf{E}(\mathbf{r},t) = E_0 \exp[i(\mathbf{k}\cdot\mathbf{r} - \omega t)] + c.c. \tag{3.22}$$

TD-DFT finds its formal foundation in the Runge-Gross (RG) theorem.[102] The time evolution of the system, governed by the Schrödinger equation, propagates the initial state (usually the ground state) over the interval $[t - t_0]$. The RG theorem proves that the information about this dynamics are encoded in the time-dependent density, hence allowing to use it instead of the wavefunction.

Using an approach similar to static DFT, within different functional approximations, it is possible to obtain any desired observable of a time-dependent many-particle system. Calculating the energy E_j of the j-th excited state is one of the goal of TD-DFT. This is achieved by the time dependent energy expec-

tation value, eq. (3.23), and the expansion of the wavefunction over the excited state eigenfunctions, eq. (3.24):

$$E(t) = \langle \Psi(t) | \hat{H}(t) | \Psi(t) \rangle \tag{3.23}$$

$$|\Psi(t)\rangle = \sum_j c_j(t) e^{-iE_j t} |\phi_j\rangle \tag{3.24}$$

which lead to

$$E(t) = \sum_j |c_j(t)|^2 E_j \tag{3.25}$$

From this last expression the excited state energy can be obtained, and from the squared coefficients the transition rates and so the oscillator strengths, essential to reconstruct any optical absorption spectra.

3.3 A Metric To Describe Exciton Topology

3.3.1 Charge Transfer Character and Partecipation Ratio

The topology of the excited states can be difficult to understand, especially when they involve multiple transitions. In CdSe clusters, even the lower energy excited states correspond to a combination of many singly-excited configurations. Therefore, the analysis of the hole and electron distribution requires a post-processing of the configurations obtained as a results of TD-DFT calculations. The approach we illustrate in the following is based on dividing the whole system in fragments and studying how they are involved in the exciton. This approach allows us to understand key aspects of the excited states: for example, the extent of delocalization and possible charge transfer character.

To accomplish this aim we want to recover information in the simplest form possible, and to do so we use descriptors. Namely, we introduce the participation ratio (PR), which quantifies the number of fragments involved in the excited state hence the degree of delocalisation over the whole system, and the charge transfer index (CT) which accounts for the charge transfer character of an excited state.

These descriptors come from the work done by F. Plasser [103, 104] initially

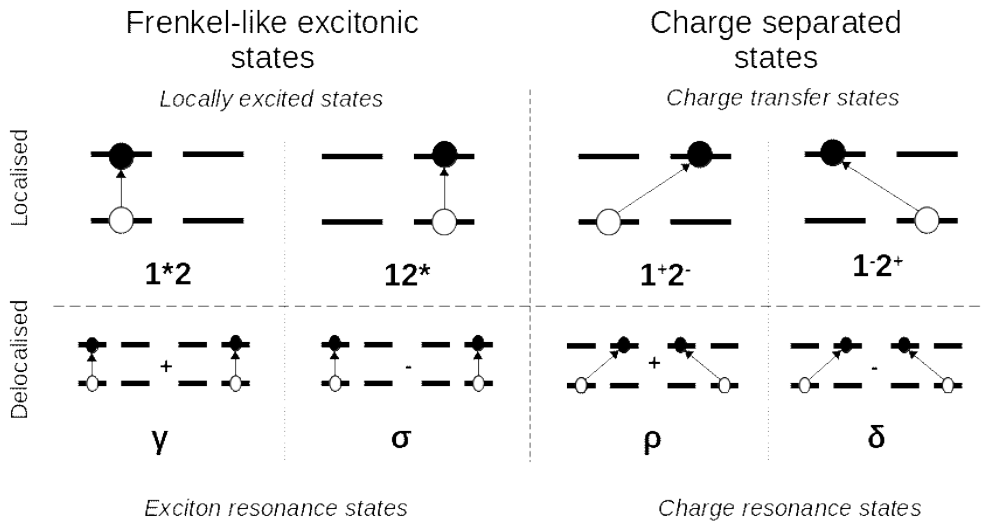

Figure 3.1: Frenkel-like excitonic states and charge-separated states in the localised basis set and delocalised basis set, adapted from ref. [103] maintaining the same notation.

intended to understand energy transfer and excitation delocalisation in multi-chromophoric systems and organic crystals. The definition of the fragments is specific for the system and the property we wish to investigate. In our case we will adopt several definitions of fragments: two different portions of the same cluster, as for example to study the participation of the inorganic cluster and the organic linker, or different units in a dimer configuration to study the extent of exciton delocalisation.

In order to introduce the indexes describing excitons, let us consider a dimer of interacting units 1 and 2, each one with two energy levels only. This four levels, considered as MOs, form an orthonormal basis set $\{i_1; f_1; i_2; f_2\}$ where MOs are named i (initial) and f (final) of the n-th monomer. Using this basis set it is possible to construct four possible singly-excited localised states:

$$|1^*2\rangle = 2^{-\frac{1}{2}} E_{f_1 i_1} |0\rangle \tag{3.26}$$

$$|12^*\rangle = 2^{-\frac{1}{2}} E_{f_2 i_2} |0\rangle \tag{3.27}$$

$$|1^+2^-\rangle = 2^{-\frac{1}{2}} E_{f_2 i_1} |0\rangle \tag{3.28}$$

$$|1^-2^+\rangle = 2^{-\frac{1}{2}} E_{f_1 i_2} |0\rangle \tag{3.29}$$

where E_{rs} is the spin-averaged excitation operator in the second quantisation formalism $E_{rs} = \sum \hat{a}^{\dagger}_{r\chi}\hat{a}_{s\chi}$ and $|0\rangle$ the reference ground state - not the vacuum state.[105, 106] If the two units are equal, that is an homodimer, and there is coupling between them the eigenstates are delocalised. This new states form another (delocalized) basis for the Hilbert space of the dimer $\{i^+; i^-; f^+; f^-\}$ and can be defined in the localized MOs basis set as $i^{\pm} = 2^{-\frac{1}{2}}(i_1 \pm i_2)$ and $f^{\pm} = 2^{-\frac{1}{2}}(f_1 \pm f_2)$. The four excited states, eqs. (26-29), can be expressed in the two basis as a couple of transitions involving localized or delocalized states as:

$$\begin{aligned} |\sigma\rangle &= 2^{-\frac{1}{2}}(|1^*2\rangle - |12^*\rangle) \\ &= \frac{1}{2}(E_{f_1i_1} - E_{f_2i_2})|0\rangle \\ &= \frac{1}{2}(E_{f^+i^-} + E_{f^-i^+})|0\rangle \end{aligned} \qquad (3.30)$$

$$\begin{aligned} |\delta\rangle &= 2^{-\frac{1}{2}}(|1^-2^+\rangle + |1^+2^-\rangle) \\ &= \frac{1}{2}(E_{f_1i_2} + E_{f_2i_1})|0\rangle \\ &= \frac{1}{2}(E_{f^-i^-} - E_{f^+i^+})|0\rangle \end{aligned} \qquad (3.32)$$

$$\begin{aligned} |\gamma\rangle &= 2^{-\frac{1}{2}}(|1^*2\rangle + |12^*\rangle) \\ &= \frac{1}{2}(E_{f_1i_1} + E_{f_2i_2})|0\rangle \\ &= \frac{1}{2}(E_{f^+i^+} + E_{f^-i^-})|0\rangle \end{aligned} \qquad (3.31)$$

$$\begin{aligned} |\rho\rangle &= 2^{-\frac{1}{2}}(|1^-2^+\rangle - |1^+2^-\rangle) \\ &= \frac{1}{2}(E_{f_1i_2} - E_{f_2i_1})|0\rangle \\ &= \frac{1}{2}(E_{f^+i^-} - E_{f^-i^+})|0\rangle \end{aligned} \qquad (3.33)$$

where the states $|\sigma\rangle$, $|\gamma\rangle$ are Frenkel-like excitonic states (combination of excitation within one fragment only)[93] and $|\delta\rangle$, $|\rho\rangle$ are charge transfer resonance states (combination of excitation across the two fragments).[107] The nomenclature used has chosen to match with the literature, ref. [103] and the original proposing paper [108]. For a schematic visual representation of these states see fig. 3.1.

For a generic excited state α let's define an element of the one-electron transition density matrix (1TDM, $\mathbf{D}_{0\alpha}$) as:

$$[\mathbf{D}_{0\alpha}]_{rs} = \langle 0|E_{rs}|\alpha\rangle \qquad (3.34)$$

where r runs over the occupied orbitals and s over the virtual orbitals. The matrix has to be considered to be a block matrix. Working in the localised excited state basis set (LES), the blocks on the diagonal refer to individual fragments

excitations, whereas off-diagonal ones relate to charge transfer states.

As an example given α to be $|1^*2\rangle$, the one-particle transition density matrix reads as follows:

$$\mathbf{D}_{0|1^*2\rangle} = \left(\begin{array}{cc|cc} 0 & \sqrt{2} & 0 & 0 \\ 0 & 0 & 0 & 0 \\ \hline 0 & 0 & 0 & 0 \\ 0 & 0 & 0 & 0 \end{array}\right) \tag{3.35}$$

the relation to eq. (3.26) is evident. Another matrix can be obtained from the 1TDM, the *charge transfer number matrix*, which is defined by charge transfer number as its elements:[109]

$$[\mathbf{\Omega}^{\alpha}]_{AB} = \frac{1}{2} \sum_{\substack{a \in A \\ b \in B}} ([\mathbf{D}_{0\alpha}^{[LES]}]_{ab})^2 \tag{3.36}$$

thus the matrix associated to the $|1^*2\rangle$ state is simply:

$$\mathbf{\Omega}^{|1^*2\rangle} = \begin{pmatrix} 1 & 0 \\ 0 & 0 \end{pmatrix} \tag{3.37}$$

While the 1TDM is a square matrix expressed in the Hilbert space of the MOs orthonormal basis set, and hence it is difficult to understand at a glance, the charge transfer number matrix is expressed in the space of the fragments. It is then a simple matrix with dimension 2×2.

From this matrix it is possible to define the first index of interest, that is the charge transfer character (CT) of the excited state. In the example of the state α the CT reads:

$$CT = \frac{1}{C} \sum_{\substack{A \\ B \neq A}} [\mathbf{\Omega}^{\alpha}]_{AB} \tag{3.38}$$

that is the total weight of the configurations with the initial and the final orbitals into different fragments, given by the sum over the off-diagonal elements of $\mathbf{\Omega}^{\alpha}$, where C is a normalisation coefficient, that for a orthonormal basis set is simply equal to 1 in the CIS frame, and close to be unitary for all the transitions that can be described by one-electron transitions.[103, 110] Hence, CT index is able to

discriminate the nature of delocalised excited states: Frenkel-like excited states are a combination of local excitons thus the off-diagonal elements are null (CT=0), whereas the resonance of pure charge transfer states leads to a null diagonal and non zero off-diagonal elements (CT=1).

From the charge transfer number matrix, information about the extent of the delocalisation over different fragments can be recovered, too. To do so, the participation ratio is defined first by defining the participation of the fragments in the delocalisation of the holes and the electrons individually:

$$PR_I = \frac{C^2}{\sum_A (\sum_B [\mathbf{\Omega}^\alpha]_{AB})^2} \tag{3.39a}$$

$$PR_F = \frac{C^2}{\sum_B (\sum_A [\mathbf{\Omega}^\alpha]_{AB})^2} \tag{3.39b}$$

describing the sum of the weight of excitation of every single fragment A towards any possible other fragment B (eq. 3.39a) for the delocalisation of the hole and the sum over every fragment B to be the final of an excitation of any fragment A (eq. 3.39b).

Then, the participation ratio (PR) is defined as the average of these two quantities:

$$PR = \frac{PR_I + PR_F}{2} \tag{3.40}$$

In a similar fashion the average position of the excitation (POS), referred to in the fragments space, is defined as the average of the initial position POS_I and the final position of the excitation POS_F, assigning the numerical value to the fragments ensemble (A=1, B=2):

$$POS = \frac{\sum_A A(\sum_B [\mathbf{\Omega}^\alpha]_{AB}) + \sum_B B(\sum_A [\mathbf{\Omega}^\alpha]_{AB})}{2C} \tag{3.41}$$

To clarify various situations that might be encountered while dealing with systems whose behaviour is far from being ideal, and to summarise the concepts illustrated so far, it is important to exemplify and visualise the use of these descriptors first in idealised situations, as the four presented in fig. 3.1 and further schematised in fig. 3.2.

In the simplest case, a local excitation that takes place in one of the two

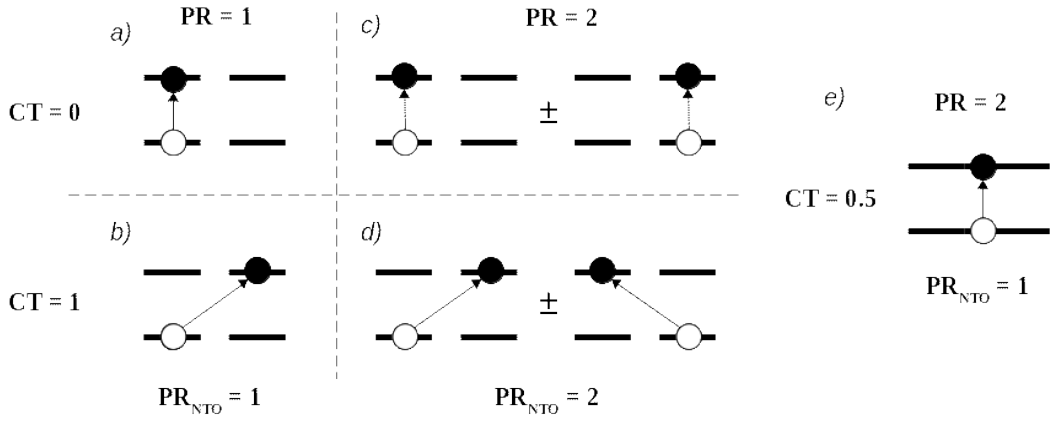

Figure 3.2: Schematic representation of singly excited states of an ideal homodimer and their participation ratio (PR) and charge transfer character (CT) values. Top left (a) one of the two local transitions, electron and hole on the same site, with CT=0 and PR=1. In bottom left scheme (b) a charge transfer state, hole and electron in different sites, characterised by CT=1 and PR=1. The corresponding delocalised combinations are in the right bottom and top corners (c,d) and are characterised by the same CT value as the localised base but PR=2. (e) an excitation between a delocalised hole and a delocalised electron, thus a mixture of schemes (c,d), is characterised by CT=0.5 and PR=2.

fragments, the participation ratio is PR=1 as only one unit is involved and the charge transfer character is zero (CT=0). Moving along to the second type of transition in the localised basis, a pure charge transfer transition from monomer 1 to monomer 2, the CT character is now CT=1 as the hole is completely localised on the first fragment, the electron on the second, and there is a net charge moving from one unit to the other.

The participation ratio value instead is less straightforward to rationalise, because it is still PR=1, even if the transition occurs among both the units. The reason can be found in the definition of PR in eqs. (3.39) and (3.40): both PR_I and PR_F are equal to one because the hole and the electron are completely localised in either one of the fragment. Then, their mean is one again. This helps to clarify the meaning of PR as a descriptor of the extent of the delocalisation in the system intended as the extent of the basis set function needed to describe the transition.

As a matter of fact, the transitions arising from a linear combination of solely locally excited states or solely charge transfer states have the same participation ratio, PR=2. The CT index still allows discriminating whether the state is a combination of local excitations or the resonance of two opposite charge transfer

transitions. Again more attention has to be paid to this latter case, because even if CT=1 the obtained state show an overall null net transfer of charge.

Further different states can be obtained from various combinations of local excitation and charge transfer states or their combination: in the example scheme in fig. 3.2(e) the exact combination of an excitonic resonance state (c) and a charge resonance state (d) is characterised by CT=0.5, as intuitively net charge transfer states contribute for half of the configurations, but PR=2, as the two fragments equally contribute to the state.

In real systems we move far from the ideal situation, especially in complex and heterogeneous systems as those considered in this work, and usually excited states are a combination of several configurations. Moreover, let's explicitly note that these indexes depends on how the whole system is fragmented.

For example, when dealing with dimers linked together by a bridging ligand, one of the possible fragmentation is to consider each core as a fragment with the bridging ligand equally shared between the two units. Therefore the one should pay attention to the meaning of the descriptors in this specific case.

As an example, we will see later in Chapter 4, that the first dark transitions of several clusters are attributed to the ligand by the visual analysis of the involved states, while the PR is observed to vary between 1.25 and 1.5 [e.g. the first two transitions of dimer **8D** have PR=1.3]. If the transitions would have been involving the bridging ligand alone and the involved MOs perfectly symmetric to the axes dividing the fragments the participation ratio should have been PR=2. Three major factors might have influenced these values: (i) the transition is not pure intra-ligand and there is already participation of the clusters, (ii) even if the transition is purely of the ligand, the MOs involved are asymmetric, (iii) the transition is a mixture of a single local excitation and a single charge transfer state, or possibly a combination of all these factors.

Thus, these descriptors of the excitations have to be used in combination with other tools, such as NTOs, the average position of hole and electron among the fragments and their distance to achieve a comprehensive understanding of the excited state topology.

3.3.2 Natural Transition Orbitals

The definition of an excitation of a single excited state between delocalised orbitals leads to a mixture of locally excited and CT contribution:

$$\begin{aligned} |\alpha\rangle &= 2^{-\frac{1}{2}} E_{f^+i^-}|0\rangle = 2^{-\frac{3}{2}}(E_{f_1 i_1} - E_{f_1 i_2} + E_{f_2 i_1} - E_{f_2 i_2})|0\rangle \\ &= \left(\frac{|1^*2\rangle - |12^*\rangle}{2\sqrt{2}} + \frac{|1^+2^-\rangle - |1^-2^+\rangle}{2\sqrt{2}}\right) \\ &= \frac{1}{2}\left(|\sigma\rangle - |\rho\rangle\right) \end{aligned} \tag{3.42}$$

In the results of excited state calculations of generic systems can be complicate to establish the nature of the hole and the electron as the excitation is a combination of many different transitions with no dominant configuration.

A compact visualization of the hole and the electron distributions can be obtained with the definition of natural transition orbitals (NTO)[111]. NTOs are found by applying a Singular Value Decomposition to the transition matrix.[112] This way, a compact representation for $\mathbf{D}_{0\alpha}$ is found, a diagonal form given by:

$$\mathbf{D}_{0\alpha}^{[NTO]} = \mathbf{U}\text{diag}(\sqrt{\lambda_1}, \cdots, \sqrt{\lambda_n})\mathbf{V}^{\mathbf{T}} \tag{3.43}$$

where λ_i is the weight of the i-nth transition. $\mathbf{U}$ and $\mathbf{V}$ are the unitary transformations applied to the occupied orbitals and the virtual orbitals, and therefore they denote respectively holes and electrons positions.

Hence, what obtained is an optimised basis set to describe each transition, whose basis functions are the best combination of the original KS orbitals. To recall once more the ideal cases depicted in fig. 3.2, the Frenkel-like transition (c) is described by the combination of two local excitations and is then described by two couples of NTOs, whose coefficients are equal, $\lambda_1 = \lambda_2 = 0.5$. The transition between delocalised states (e), formally written in eq. (3.42), is described by four states in the localised excited state basis set, but it can be described by a single couple of NTOs: one for the delocalised hole, optimised combination for the initial state, and one for the delocalised electron, optimised for the final state.

3.3.3 Entropy and PR_{NTO}

The great power of NTOs is the visual representation of the excitation process, in terms of orbitals depiction in real space. The main issue within this approach is that transitions must be analysed one by one, possibly resulting in a huge quantity of orbitals that must be computed and plotted. Even if this is essential to clearly understand the nature of the transitions, we can collect some of the information into a single value descriptor. This allows us to overcome, partially, the need for visualising each transition and focus on the few transitions that capture our interest. So we define a participation ratio based on the number of NTOs:

$$PR_{NTO} = \frac{(\sum_i \lambda_i)^2}{\sum_i \lambda_i^2} \tag{3.44}$$

This expression, based on the *collectivity number* introduced by Luzanov,[113, 114] helps to formalize the last concept introduced in the previous section as it, in the ideal scenario, measure the number of states transitions needed to describe the excited state.

In the case of equal amplitudes of the participating NTOs, e.g. in the ideal case (c) in fig. 3.2, the PR_{NTO} is exactly the number of entangled states:[115]

$$Z_{h|e} = PR_{NTO} \qquad iff \quad \lambda_i = \lambda_j \ \ \forall\lambda \tag{3.45}$$

It is then possible to relate this index to the entanglement entropy of the electron-hole subsystem as $S_{h|e} = \log_2 PR_{NTO}$. However, in more real cases the number of states $\mathrm{Z}_{h|e}$ and PR_{NTO} are different enough to avoid to use this as a reliable value in itself and we better study its trend and values that emerge as particular in the distribution, especially combined with the other indexes.

Chapter 4

Topology Of The Excited States

In this Chapter the main results of the investigation on the topology of the excited states of the systems introduced in Chapter 1 are presented and discussed. Specifically, after the benchmark of the methodology for CdSe clusters, I present the electronic structures of (i) the isolated clusters and exciton delocalising ligands, (ii) the substitution of one ligand with the bridging ligands to form modified clusters which are considered as the monomers, (iii) the formation and investigation of the homodimers and then (iv) of an engineered hetero-dimer. I will discuss both ground state properties such as charge distribution, density of the states and molecular orbitals and excitation and optical properties such as absorption spectra, indexes describing the excited state topology and natural transitions orbitals.

4.1 Benchmark of the Methodology

First of all, we investigate the **Cd4Ph** to validate and benchmark the method for what concern the choice of the functional used for the TD-DFT calculation and the choice of the basis set. We start from the same method adopted in our recent work in ref. [25], which included a study of the **Cd10** monomer.

The validity of the substitution of phenyl groups (Ph) of the ligand shell with methyls (Me) to reduce the computational cost is then evaluated studying the simulated optical spectra of the **Cd10** monomer with the two different cappings, reported in ref. [25], and then further investigated by the comparison of properties

within **Cd4** and **Cd8** monomers with different ligand shells.

The geometry of **Cd4Ph** was optimised at B3LYP[116] level of theory without symmetry constrains, to relax the structure in the vacuum situation, from the X-ray data in [21]. To deal with relatively heavy atoms such as Cd and Se two different basis set have been used at first, namely the LANL2DZ basis set[43, 117] with the corresponding effective core potential (ECP)[118] for Cd and for Se, while the 6-31G(d) basis set was employed for ligand atoms such as C, H, N, P, O, S and Cl.[119–121]

Dispersion forces were considered within the Grimme's function original dumping D3(0) version,[122] zero-dumping, and in the Becke and Johnson damping correction D3(BJ).[123–125]

To check the validity of the optimised geometry the IR and Raman vibrations were computed, to ensure that no imaginary (negative valued) frequencies are shown in the calculation. Such imaginary components, when present, indicate that the geometry does not correspond to a minimum of the potential energy surface (PES): one negative component locates a saddle point, more the one locate the geometry on a generic point over the PES.

The optical spectrum of the optimised geometry of the **Cd4Ph** system was investigated by calculating 100 singlet transitions using five different functionals summarised in the following.[126, 127] The profiles of the absorption spectra were obtained by a Gaussian broadening function with a line width (σ) of 85 meV, consistent with the experimental characterisations of this and similar systems,[128] and another Gaussian broadening of 200 meV that better simulate the experimental absorption profile, although loses the capacity to give a detailed description. The broadening used for the investigation in then $\sigma = 85$ meV.

The Becke three-parameter Lee-Yang-Parr functional (B3LYP) is a global-hybrid GGA, tested because for its simplicity is already used for the geometry optimisation, and because it has been used successfully for ZnS clusters.[129–131] CAM-B3LYP is the range-separated implemented functional of B3LYP designed to perform better in the description of CT states.[132, 133] In M06-HF functional full HF exchange is considered, hence self-exchange interactions at long range are not present. It is usually better than B3LYP on electronic GS but most impor-

tantly has good performance reported for TD-DFT, and CT states as well.[134] MN15,[135, 136] a global-hybrid meta-NGA, is in the same family of M06-HF, called Minnesota functionals (Myz), developed by Truhlar's group. It has been designed to have broad accuracy for various parameters and specifically for new energy-related material design. For this functional the Grimme's D3 dispersion function in the according to Becke and Johnson (BJ-damping) was used, since the D3(BJ) parameter for MN15 can be found in Table SI.2.1 of SI of Grimme's GMTKN55 database paper [125] while D3(0) is not implemented. The BJ-dumping is more practical for weakly bonded complexes, but even if this is not the case it is better to have a less dumped dispersion function rather than none at all. This shouldn't be so relevant given that all the optimisations are computed at the same level using GD3 function but it has been done for the sake of precision. To conclude, the latest functional from Head-Gordon and coworkers, a long-range corrected hybrid functional, ωB97XD have been used.[137] It includes already an empirical dispersion function, in the D2 version of Grimme's form (dumped atom-atom dispersion).

The analysis done highlights two different functionals for different reasons. The absolute transition energies, neglecting relative intensity ratio, are well described by Truhlar's group newest functional MN15 (δ=0.16 eV). Since we want to investigate the interactions between excited states of clusters linked and thus eventually separated in space by organic ligands, the second functional we choose is CAM-B3LYP. As previously mentioned, CAM-B3LYP is a long-range corrected functional, and so it is expected to describe better such interactions between the cores and states with charge transfer character.[132, 138] Among the long-range corrected functionals we have tested, CAM-B3LYP gives the best description of the relative intensities of the bands. Absolute transition energies are overestimated (δ=0.71 eV) but, beside the shift toward higher energy, it conserves almost the same shape of MN15, in particular the first band, along with good computational effort feasibility. This second benchmark study confirms and supports the results already obtained for **Cd10Ph**.

Therefore, with the exception of a parallel check with MN15 performed for all the clusters and for the following benchmarks of basis sets and methyl substitu-

tion, CAM-B3LYP is used in the following for all TD-DFT calculations and all the results presented.

With the selected MN15 and CAM-B3LYP functionals, we tested different basis set, with 6-31G(d)/LANL2DZ as a starting point. The most cost-effective and performing basis resulted in the mixed basis set 6-31G(d)/LANL2DZ(d,p)/ LANL2DZ.

Since, to make the calculations feasible, Cadmium and Selenium atoms need to be described by a pseudopotential ECP due to their number of electrons, to use great time-consuming complete multiple-basis for lighter elements lacks of meaning. Another split-valence Pople-type basis is therefore used, considering the unrestricted description of one more valence orbital and another diffusion function added, 6-311G(d,p).[139] This change of basis for the sole ligands atoms greatly intensifies the computational cost and poorly improves the results, shifting the first peak of $\delta' = 0.045$eV, one order of magnitude less than the shift from the experimental data.

A comparative study of basis for similar CdSe systems done by S. Kilina *et al.*[117] gave the hint for the modification of LANL2DZ basis, with the addition of different polarisation function. Unlikely to what done in ref. [117], the modified LANL2DZ basis is used for solely Cd and Se atoms instead of the whole system's elements. Progressively, the additional functions are initially added as one-member polarisation set.

The first basis set so modified is LANL2DZ(*), using the d type polarisation function for Se present in ref. [140] and a simply p type from ref. [141] for Cd. Differences in the computed spectra are small but consistent, without a substantial growth of computational effort. Thus other modified basis are tested with different polarisation functions. Using the new Basis Set Exchange software[142] different basis sets have been compared to choose another polarization function for Cd.

The second modification of LANL2DZ is by addition of the same d type polarisation function for Se as used before and an f type orbital for Cd, obtained from the newest jorge-DZP-DKH basis, an all-electron double zeta valence quality plus polarization basis set, optimised for relativistic effect comprehensive

calculation.[143] This modified basis is therefore addressed as LANL2DZ(df). A further modification is given by the addition of the above-mentioned f function for Cd and the use of the tested LANL2DZ(dp), which uses one p and one d polarisation functions for Se,[140, 142] and it is here referred as LANL2DZ(pdf).

The effect of the polarization function on Cd centres is compared to a modification for the solely Se atom for the tested LANL2DZ(dp). The most interesting effect is given by *(d,p)* on Se centres, as a shift of the absolute transition energies towards the experimental values, while the addition of a solely d function slightly increases the shift, and none appreciable modifications arise improving the basis on Cd centres. Therefore the LANL2DZ(d,p) basis set is used for Se centres, LANL2DZ for Cd centres and 6-31G(d) for all the other atoms.

4.1.1 Substitution with Methyl Groups

In computational studies of hybrid nano-clusters, it is a rather common practice to substitute the side chains of the ligand shell with methyls to save resources. This practice is as common as potentially misleading as the chemical nature of the ligand shell is known to play a key role in the photophysical properties of semiconducting clusters and quantum dots. Therefore, we explicitly investigated the effect of the substitution of the phenyl ligand shell with methyls in the **Cd4** and **Cd10** clusters. For **Cd4** the spectra show to be quite different, but the first band still shows similar features and profile, even if red-shifted. That is because the frontiers states, both occupied and virtual, are states localized mainly in the inorganic core. For **Cd10** the first band is slightly narrowed and blue-shifted, fig. 4.1. Nevertheless, by the analysis of the natural transition orbitals of the excited states of the first band, we can conclude that the nature of the optical transitions remains substantially the same: the electron is mainly localised over Cd centres and p orbitals of Se mainly contribute to the hole in both the clusters, fig. A.40. Notice that this composition of the hole and electron states is consistent with the EMA model of the valence and conduction band in bigger CdSe QDs. The main effect of the phenyl rings is to sightly delocalize the hole density without changing the nature of the transitions.

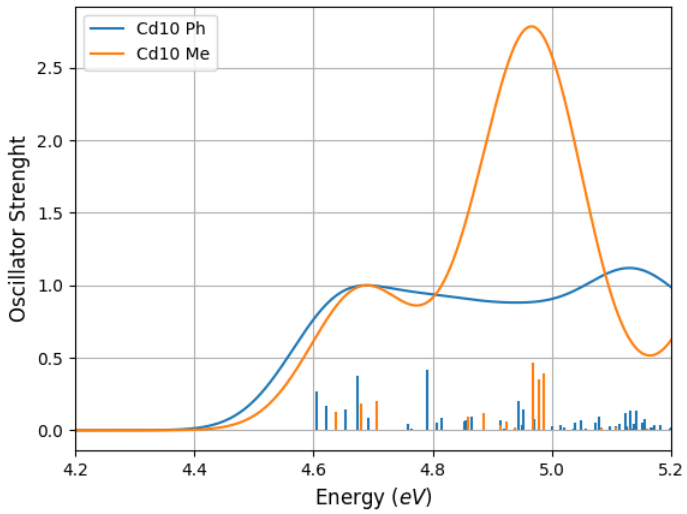

Figure 4.1: Normalized spectra of $Cd_{10}Se_4(SePh)_{12}(PPh_3)_4$ in blue line and $Cd_{10}Se_4(SeMe)_{12}(PMe_3)_4$ in orange, obtained using CAM-B3LYP/*, *: LANL2DZ/6-31G(d), calculated for ref. [25].

4.1.2 Implicit Solvent

To study the extent the outer environment influences the system by means of electrostatic effects we test the response of the smallest cluster Cd4 in implicit solvents with different dielectric constants. Three values of the dielectric constant have been studied: ε_1=5.5, ε_2=46.7 and ε_3=78.4, to explore cases where the cluster is embedded in a matrix characterised by a low, medium and high dielectric constant. The first value is chosen according to ref. [144] and it mimics a non-polar organic medium, the latter is the water dielectric constant, as an example of a possible solvent, while ε_2 is an intermediate value to observe the trend. The effects due to this environments were studied for the pristine clusters and the methyl-substituted ones, to indirectly investigate the effect of the organic ligands shell, since it acts as a protective shell and as a first solvent-like environment for the inorganic core. Because of this consideration, the effect of the solvent has been studied to the slightly bigger cluster **Cd8** as well, to investigate whether or not systems with a different dimension of the core are influenced differently.

The effect of the different solvents is in the order of few tens of meV of shift of the first band, that remains almost unchanged and a modification of transitions intensities of the higher energy region of the absorption spectra, fig. 4.2.

We can therefore conclude that the effect of a change in the dielectric medium

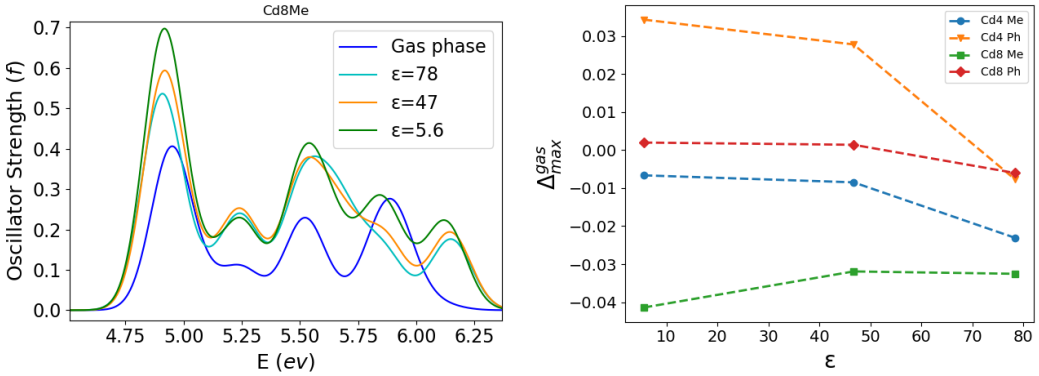

(a) (b)

Figure 4.2: (a) Spectra of **Cd8Me** in different environments and in gas phase. In (b) the shifts respect to the gas phase monomer spectrum are plotted against dielectric constant values for **Cd4Ph**, **Cd4Me**, **Cd8Ph** and **Cd8Me**.

outside the ligand shell has a minor contribution to the optical properties of the clusters. For this reason all the calculation hereafter refer to the gas phase.

4.2 Monomers

Here we lay the starting point for the journey through the following sections, where step by step the main ingredients are added and the systems are built.

The main characteristics of each monomer are here described and they will serve as a reference for the subsequent analysis of the effect of the particular ligands that act both as exciton delocalising agents in the modified monomers and also as bridging ligands, or linkers, in the dimeric systems.

The correctness of the geometry optimisation of all clusters was verified by the computation of all vibrations and the results are consistent with experimental data and previous theoretical calculations.[21, 145, 146] The structures and dimensions of the clusters are commented in the following.

Cd4 has an adamantane-like structure, which is recognisable in as a cell of the zinc-blende lattice of the bulk. The diameter of the inner bare inorganic core is 0.65 nm and the diameter of the whole cluster comprehensive of the methyl ligand shell is 0.92 nm, whereas it is about one nanometer if substituted by phenyl groups. In the **Cd8** cluster, a combination of both zinc-blende and wurtzite structures can be identified, with a central Se atom bonded to four different

Cd centres. The diameter of the inorganic core is 0.86 nm and the methyl-capped cluster has a diameter of 1.12 nm. The **Cd10** cluster shows again a mixture of zinc-blende and wurtzite structures, the latter as the inner core, while adamantane cages can be appreciated among inner and external atoms. The diameter of the inorganic core is 1.0 nm and the methyl-capped cluster has a diameter of 1.57 nm. Increasing further the dimensions, **Cd17** clearly shows a regular cubic zinc-blende phase in a central position, while the surface is relaxed. The diameters of the inorganic core and the whole cluster are respectively 1.32 nm and 1.78 nm.

The ionisation potential (IP) and electron affinities (EA) of these clusters were obtained in two different fashions, vertical and adiabatic, by mean of two further optimisation calculations, respectively removing and adding one electron to the total net charge. The vertical value is the energy required to remove, or the amount of energy released when one electron is added to the system instantaneously, i.e. at the geometry of the nuclei frozen, and it is obtained by a single-point energy calculation at the geometry of the cluster in its original charge state. Conversely, the adiabatic value is obtained by the difference of the total energy of the optimised systems, that is after the relaxation of the geometry to the new electronic distribution. All the values of the homologous are reported in eV units in table 4.1.

By comparison of the results and considering the initial net charge of the structures, it is evident an increasing trend for the IP, whereas it is more peculiar for the EA. In particular, the values of **Cd10** and **Cd17** are notable. The former has no net charge in the initial situation, and yet it is less prone to accept an electron than the smaller and doubly negatively charge clusters. **Cd17**, which has a positive net charge (2+) in the initial state, is the most prompt to accept one electron. Even so, the values compared to the other small cluster **Cd4** and **Cd8** are still comparable. The expected features of these values are not seen in the modified monomers and in the dimers later reported, bearing the first hint that a simple effect of CT is not the explanation of the behaviour of these systems.

The density of states (DOS) of the overall systems (TDOS), the projected densities of states (PDOS) for core and ligand shell, the energy gap and the

	IP (eV)		EA (eV)		ΔE_{gap} (eV)
	vertical	adiabatic	vertical	adiabatic	
Cd4	1,72	1,31	-3,43	-2,86	4,788
Cd8	2,07	1,82	-2,06	-1,88	7,021
Cd10	5,88	5,59	-0,25	0,66	6.638
Cd17	9,90	9,66	-4,27	-4,41	6.602

Table 4.1: Vertical and adiabatic ionisation potential (IP) and electron affinities (EA) calculated for all the methyl-substituted monomers at at B3LYP theory level.

	μ_2 (bridging)	μ_4 (tetrahedral)
Cd	-	0,95
Se	-0,35	-1,1
C	-	-0,85

Table 4.2: Average charge of the elements in the pristine clusters, calculated by NPA and expressed in unit of electron charge ($e = 1.60217662 \cdot 10^{-19}$ C).

charge distribution were obtained by the results of higher theory computations, i.e. after the SCF procedure done with the CAM-B3LYP function that precedes the TD-DFT calculation. The density of states describes the number of states, occupied or available to be occupied by one electron, present in an infinitesimal energy range. The DOS can be expressed as a weighted sum of PDOS, which reflect the he number of one-electron levels with weight on one particular orbital or, more useful, on a particular ensemble of orbitals. The PDOS shows that for all these methyl-substituted clusters both occupied and virtual frontier orbitals are mainly localised on the inorganic core.

The charge distributions show no surprise. The average charge of each element, analysed both with Mulliken and NPA (Natural Population Analysis) methodologies,[147, 148] is the same for the same bonding situation. Cd is always tetrahedral and whether bonding Se, Cl or P its charge fluctuates little and it is closed to +1. The Se atoms are mainly divided into two classes: those on the surface which are bound to the methyl group and form a bridge between two Cd atoms have slightly negative charge (-0,3e) while the Se in the inner cage of **Cd10** or **Cd17** or the tetrahedral core of **Cd8** carries a negative charge close to -1e. The charges reported in table 4.2 are calculated by NPA and expressed in unit of electron charge ($e = 1.60217662 \cdot 10^{-19}$ C).

4.3 Bridging Ligands: Chelated Monomers

The successive step now is to address the effect of the linker. Two special ligands were used, namely DTMT and PPNS, chosen because of their potential as exciton delocalizing ligands. First, let us consider their properties as isolated molecules in vacuum. Then, we will focus on the interaction of a single cluster with these special ligands to assess quantitatively their exciton delocalising properties.

The effect of the ligands on different cores, or better the different effect of the ligand due to interaction with different dimensions and charge, have been thoroughly investigated for the DTMT ligand. A comparison of the effect of the different organic molecules is then reported. Notice that in the next Section we will discuss the same special ligands used ad bridge in dimers of clusters. For sake of simplicity, the abbreviated notion for modified monomers and dimers, reported at p. iii, is used: the clusters chelated by a bridging ligand are noted as the number of Cd atoms of the core and D or P, namely for DTMT and PPNS, the respective dimers with the prefix **d.** (e.g. Cd8-DTMT is referred to as **8D** and Cd8-DTMT-Cd8 as **d.8D**).

Moreover, to facilitate the discussion in terms of NTOs we always refer to the transitions with higher coefficients without reporting their numerical value unless it is relevant in the discussion.

4.3.1 Isolated Special Ligands

After geometry optimisation, the optical spectra of the ligands have been investigated for the neutral form and the anionic form, by TD-DFT calculation with CAM-B3LYP functional, for a total of 10 singlet excited states.

The main features of the spectra do not change between the different forms, but the anionic spectra of both the molecules are red-shifted compared to neutral and they show one dark state at lower energies, 0.77 eV for DTMT and 0.49 eV for PPNS, these effects are due to the “free” electron. The spectra are reported in fig. 4.3.

Because they are relevant to establish the coupling with the CdSe clusters, we emphasise three features of these ligands: i) both ligands present a strong

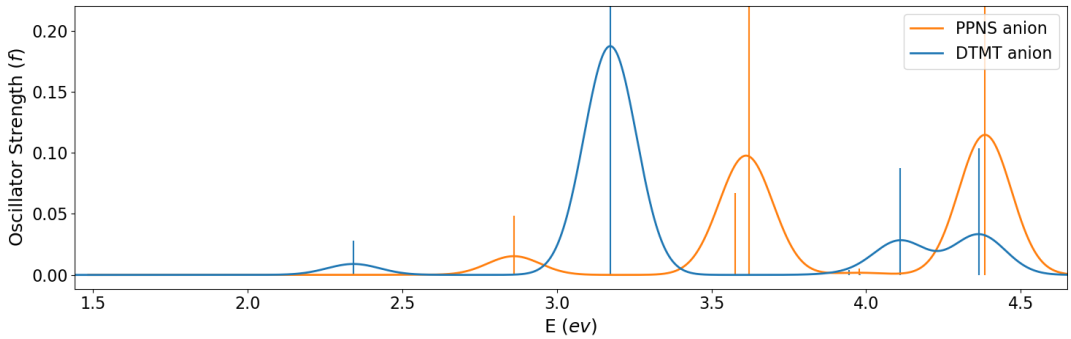

Figure 4.3: Absorption spectra of the isolated ligands, obtained with the same Gaussian broadening of the inorganic clusters ($\sigma = 85$ meV). The range 1.5 to 2 eV is shown to underline the presence of dark states.

transition around 4.4 eV, typical of benzene-like aromatic systems. These transitions are close in energy to the first absorption bands of the clusters and therefore we expect to find modifications of the complexes spectra in this region in case of hybridization of the ligand and the cluster electronic states. ii) Even if with different intensities, both ligands present several dark and bright states in the range between 2-4 eV. We will focus our attention to this energy range, because a wealth of states will appear here as a consequence of the interaction between these ligands and the CdSe clusters entailing delocalisation effects induced by the ligands. iii) Lastly, two dark states are present at low energies (1.5-2 eV), localised among the thiophene ring and the –C–S_2^- moiety, which is the bidentate chelating group binding to the cluster surface.

4.3.2 DTMT on Different Cores

To investigate the effect of the ligands on different clusters we first consider the ability of DTMT to displace electronic density, i.e. its electron-withdrawing or electron-donating action when it binds to a CdSe cluster.

The trend of the difference of charges of the clusters when the apex group, Cl^- or (PPh_3), is replaced by the aromatic ligand was calculated using NPA and it is reported in fig. 4.4.

For **4D** and **8D**, which already bear a ligand with formal net charge -1 in the pristine cluster, the effect on the total charge of the clusters is almost negligible. The distribution of the charge among the atoms of the core, on the other hand, varies, the Cd centre chelated by the ligand is slightly more negative than the ones

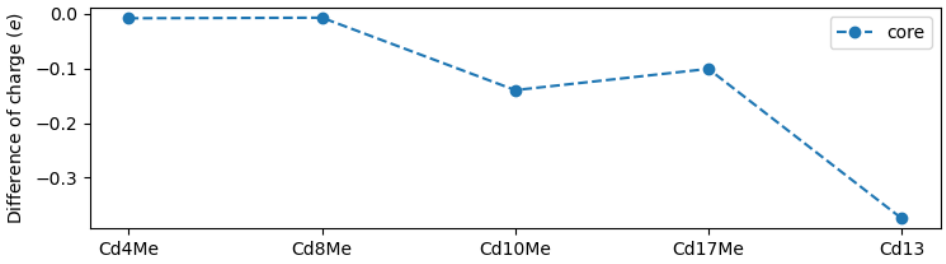

Figure 4.4: Plot of the difference of the global charge of all the clusters bonded to DTMT respect to the charges of the same clusters, obtained by summing all the atomic charges except for the ligand, whether DTMT, Cl^- or (PPh_3).

bonded with the halogen atoms. For **10D** and **17D** the variation is appreciable, with an electron density donation from the ligand to the cluster. However, the distribution of the charges among the individual atoms shows that the chelated Cd atom is depleted of charge upon binding ($\Delta e = 0.05-0.10e$) requiring a deeper explanation of this interaction. The effect of the binding on the neutral and bare cage **Cd13** is also reported, showing a substantial donation of electron density from the ligand to the core. This increased redistribution of electron density shows once more the importance of considering clusters capped by a protective ligand shell in the modelling of this kind of systems.

Now, we investigate the electronic properties of the excited states and their nature by the analysis of the absorption profile, the characteristic of each single transition, studied with the descriptors and NTO decomposition illustrated in Chapter 3, and the DOS analysis.

Figures 4.7 and 4.11 show the absorption profile of the clusters ligated with DTMT (in blue) together with the spectra of the isolated cluster (orange) and isolated ligand (green). In the smaller cluster **4D** we notice a strong change in the absorption profile, fig. 4.7, which is difficult to trace back to the original spectra of the isolate constituents This is due to its small size which is indeed comparable to the size of the linker. Nonetheless, the absorption spectrum already shows a typical feature which characterizes all the spectra of the complexes, except for **17D**, which is an intense transition at 3.2 eV. This transition can be assigned to an almost pure DTMT transition in the complexes **8D**, **10D** and **13D**. However, in the smallest monomer, we see from the relative NTO ($\lambda_1 = 0.97$) that this excited state is already strongly hybridised with the cluster showing a

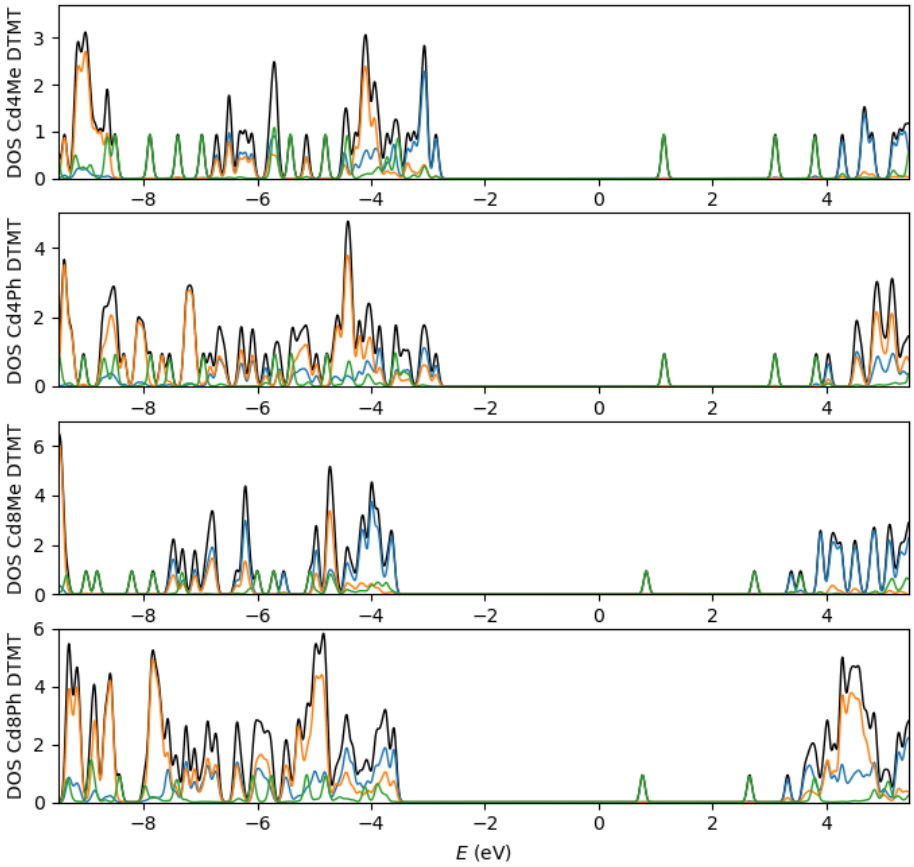

Figure 4.5: Projected density of states (PDOS) showing the contribution of CdSe cores (blue), capping ligands (blue) and chelating ligand DTMT (green). The total density of states (TDOS) are in solid black lines. The partition is based on the Mulliken scheme,[147] and the density of states has been obtained by convolution of Gaussian curves centered on the states with FWHM = 0.1 eV. In the first two panels monomers **4D** and **8D** in the latter two, respectively with methyl (Me) and phenyl (Ph) as capping ligand groups.

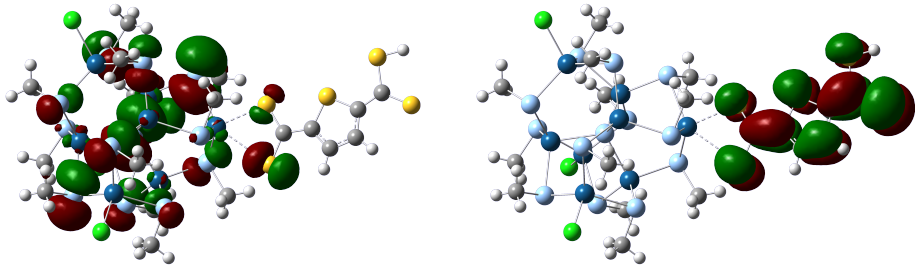

(a) HOMO (b) LUMO

Figure 4.6: Occupied (HOMO) and virtual (LUMO) frontier orbitals of monomer **8D**. Surfaces of the orbitals are shown with an isovalue=0.2.

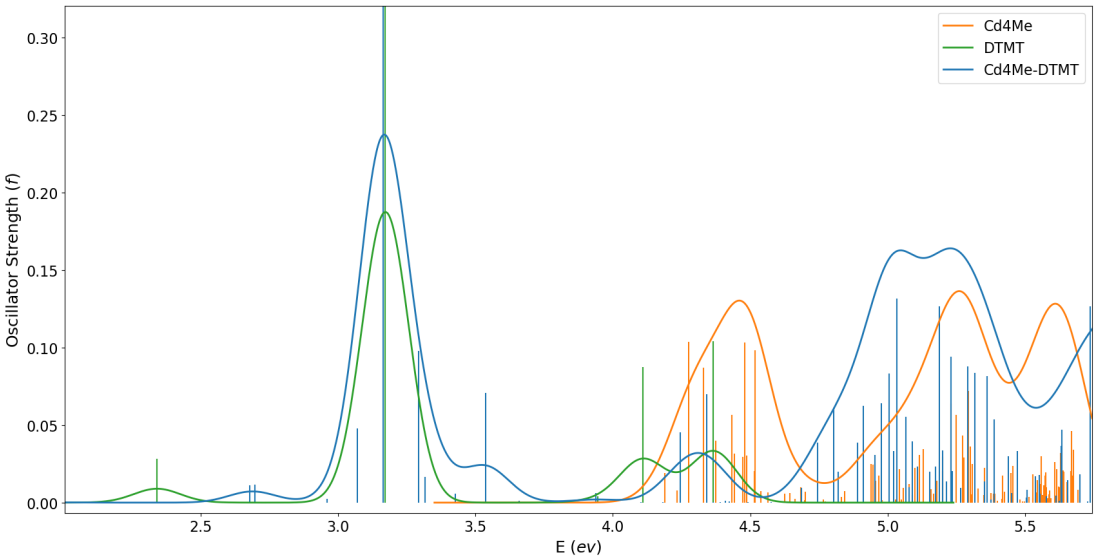

Figure 4.7: Simulated optical spectrum of **4D** monomer in blue, the isolated cluster and ligand units respectively in orange and green lines.

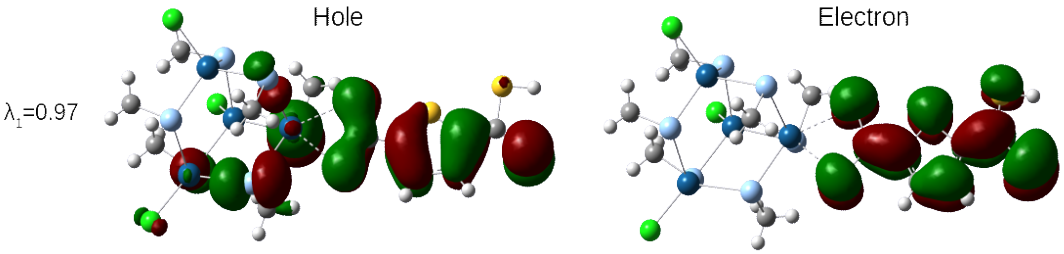

Figure 4.8: Natural transition orbitals of transition 7, the most intense transition of the first peak, of monomer **4D**. Computed transitions are plotted as vertical lines, the lineshapes of the spectra are obtained by convolution of Gaussian curves centered at each transition ($\sigma = 85$ meV).

clear charge transfer character, from a hybrid hole state delocalised on the cluster to an electron state completely localised in the ligand, see fig. 4.8. Indeed, the nature of almost all the excited states of 4D is foremost hybrid-states with CT character, especially above 4.5 eV, the range where the inorganic core participate the most.

These aspects will be discussed more extensively throughout the comparison with the other monomers and to its dimer. Let us now consider the PDOS of the complexes. The 4D and 8D clusters have been studied with both the original phenyl capping shell and a methyl capping shell, to further test the validity of the substitution of phenyl groups with methyl groups, also in the context of the interaction of the cluster with a different aromatic ligand. The DOS and PDOS

for the four monomers are reported in fig. 4.5, showing that the simplification of the model systems by methylation of the capping shell does not modify the main features of the density of states. On the other hand, it is clear that the phenyl capping shell participates to the frontier orbital composition more than methyls confirming a contribution of the phenyl capping to the size of the exciton.

For monomers **4D**, **8D**, **10D** and **13D** the occupied frontier orbitals are mainly localized in the inorganic core, while ligand trap states are present inside the cluster energy gap, progressively closer to the virtual core states as the dimension of the cluster increases. A different DOS characterizes the bigger cluster **17D**, as it will be pointed several times in the following. First, we explicitly observe that the whole DOS is shifted of about 2 eV to lower energies, frontier virtual orbitals laying at negative energies. This is simply due to the effect of the overall positive charge of the system, whereas all the others are negatively charged. What is important are the relative positions and compositions of the molecular orbitals. In this diagram, we note an inversion of the nature of the frontier orbitals, concurrent with the disappearance of ligand trap states at high energies within the gap, fig. 4.9. The occupied frontier orbital lies separated from what we can refer to as the "valence band", with a hybrid character, the HOMO localised among the external apical adamantane-like cage and the ligand, with a major contribution of the chelating sulfur atoms, fig. 4.6a. The virtual frontier orbital, in fig. 4.10b, is conversely localised on the cage only, and the immediately successive virtual states are again with a contribution of the ligand, LUMO+1 completely localised on the whole ligand and LUMO+2 with two poles, one on the DTMT and on the opposite side of the inorganic cage, fig. A.33. As we will see below, the composition of the frontier orbitals is connected to the nature of the lower energy exciton states.

The optical spectra are now addressed, first considering the spectral profile in comparison with those of the isolated components and then the distribution of the descriptors, i.e. participation ratio and CT, plotted as vertical lines in the following figures, obtained by defining the system fragments as the cluster unit and the DMTM ligand. To recall the use of these descriptors, the limit situations are (i) PR=1 and CT=0 localised transitions, (ii) PR=1 and CT=1

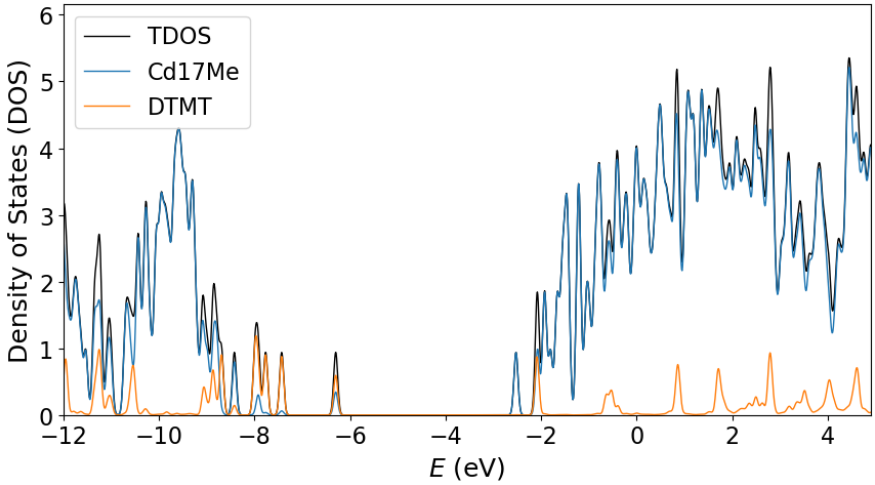

Figure 4.9: Projected density of states (PDOS) of **17D** showing the contribution of the cluster (blue) and chelating ligand DTMT (orange). The partition is based on the Mulliken scheme,[147] and the density of states has been obtained by convolution of Gaussian curves centered on the states with FWHM = 0.1 eV.

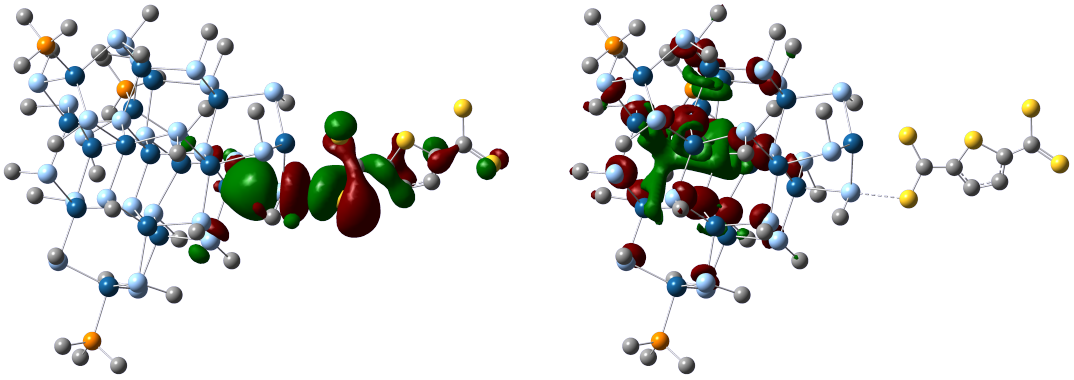

(a) HOMO (b) LUMO

Figure 4.10: Occupied (HOMO) and virtual (LUMO) frontier orbitals of monomer **17D**. Surfaces of the orbitals are shown with an isovalue=0.2.

a complete charge transfer, (iii) PR=2 and CT=0 a Frenkel-like excitonic state and (iv) PR=2, CT=1 a resonance of charge transfer states. All the intermediate situations describe exciton with partial delocalisation and CT character.

The NTO decomposition is used to visualise directly the states of interest that we selected out from the spectra comparison and the analysis of the descriptors.

Monomer **8D** optical spectrum, fig. 4.11a, shows more clearly three zones that were already present less neatly in **4D**. At energies lower than 3.4 eV transitions due to only DTMT are present, the slightly rising of PR values of the third and fourth transitions is due to a minor contribution of the bonded Cd atom. The first two lower energy dark transitions of the ligand are present in this spectral region. The characteristic DTMT transition at 3.22 eV is blue-shifted of 51 meV compared to the isolated molecule, probably due to the effect of proximity to the negatively charged cluster.

In the range 3.5 to 5 eV, tens of new states arise. This is a portion of the spectrum where, considering the isolated fragments spectra, there are no transitions of the pristine cluster whereas there are various excited states of the ligand, both dark and bright, as previously mentioned. The nature of these states can be easily assumed to have a strong charge transfer character, because of the low oscillator strengths. As a matter of fact, we can appreciate in fig. 4.12a an almost ideal limiting situation, as the values of the descriptors are almost CT=1 and PR ~ 1, hence describing complete charge transfer states. From the NTO analysis, these excitations can be confirmed as pure cluster to ligand charge transfer transitions, the hole localised on the inorganic core and the electron on DTMT. In this range, only two transitions, 15th and 16th at 3.92 eV, are between delocalised hole states to a ligand localised states. They are distinguishable because the overlap between hole and electron states over the ligand leads to a discrete oscillator strength. Of the two high energy bright transition of the ligand, the last one is still visible in the chelated monomer spectrum, namely transition 24 at 4.31 eV (PR=1.125, CT=0.097) which stands as an isolated peak in this spectral region.

At energy higher than 5 eV, which is where the pristine cluster spectrum lays, a blue-shift of the band of around 80meV is observed compared to the isolated cluster. This is smaller than the shift observed for **4D**, that is of almost 0.5 eV,

and its magnitude is comparable with the results of previous studies,[19, 25, 149, 150] although it is an unexpected behaviour since by delocalisation of the excitation we would expect a lowering of the energy of the exciton. Indeed, even if a general increase of the PR index values can be appreciated, observing the CT values and analysing the NTOs of various transitions this band can be described as a collection of hybrid state and transitions characterised by a major involvement of the cluster but still a relevant charge transfer character from the cluster to the ligand.

The optical behaviour of **10D** is quite similar to what we discussed above for 8D. The shift to the blue of the characteristic DTMT band, 56 meV, and of the high energy band is still present, although a different gaussian broadening has to be used (σ = 60 meV) to separate two different contributions to the band and obtain two relative maxima. In this condition, the blue-shift at high energy is considered to be approximately 70 meV, consistent with the shift of the smaller chelated cluster. Since the shift of the ligand transition is still present, we attribute the cause to a polarization effect due to the presence of the clusters themselves rather than to the effect of the solely overall charge of the clusters. As for **8D**, the most important feature to remember as a key point is the subdivision of the spectrum into three zones: $(2 - 3.25$ eV) the first portion, mainly due to DTMT transitions, $(3.3 - 4.5$ eV) the central zone, characterised by the presence of almost pure charge transfer transitions with the electron density moving in direction of the ligand and (> 4.5 eV) the last portion of the spectrum, mainly characterised by an increase of the delocalisation among the two fragments but still maintaining charge transfer features. In this particular spectrum more CT transitions are present in the high energy region (figs. 4.13 and A.26).

The complex **17D** is characterised by a markedly different behaviour. In this case the spectrum of the cluster-ligand complex is rather different by the superposition of the spectra of the isolated fragments and several new transitions arise, showing allowed transitions in the lower energy range between 1.5 to 3.5 eV.

By studying the distribution of the topology descriptors, fig. 4.12b, it is not possible to clearly distinguish different zones featuring a particular character.

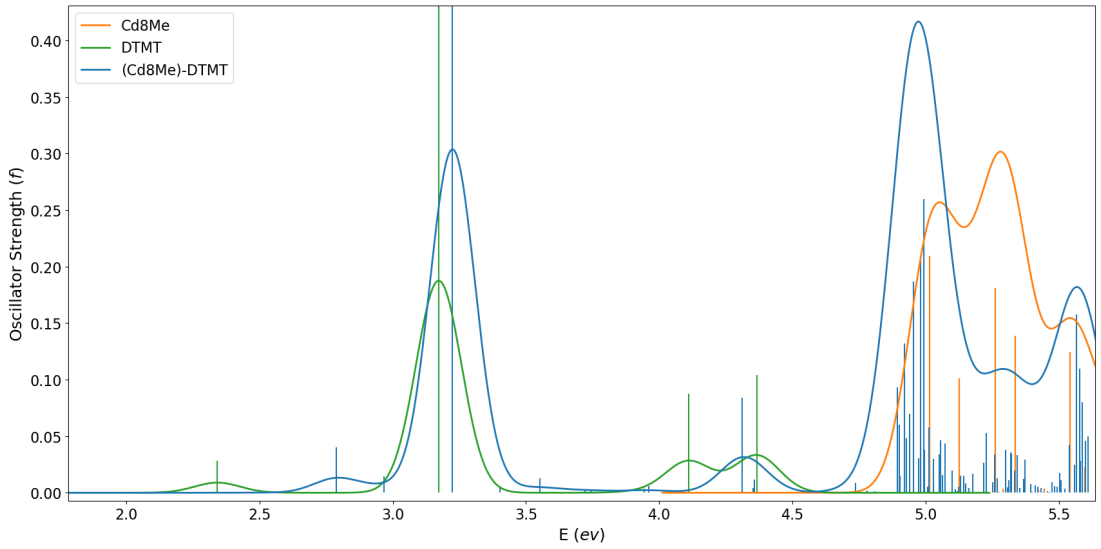

(a)

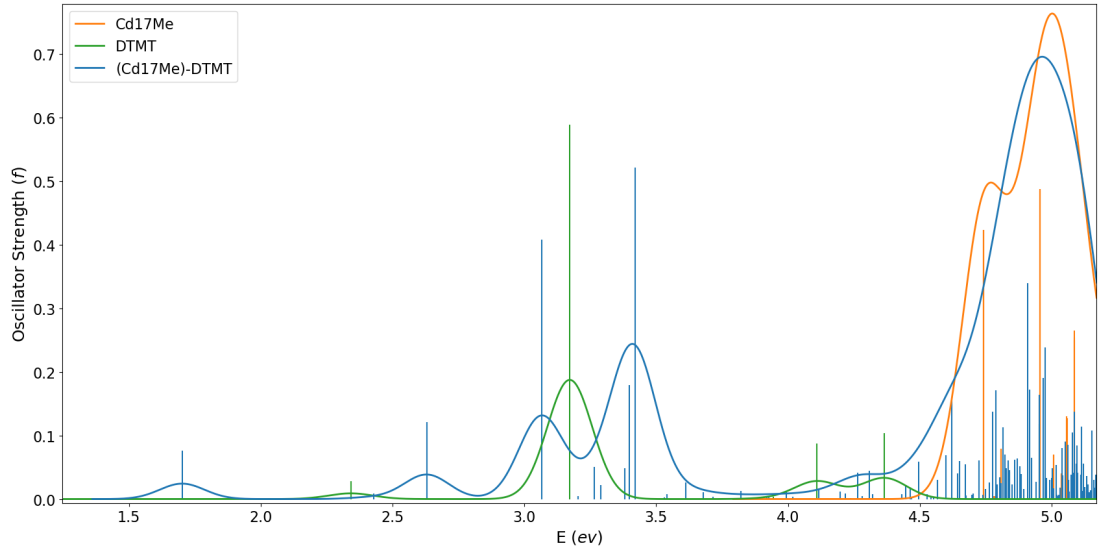

(b)

Figure 4.11: Comparison of simulated optical absorption spectra for monomers (a) **8D** and (b) **17D** and their isolated fragments. Chelated monomers in blue, isolated pristine cluster and ligand anion form respectively in orange and green. Computed transitions are plotted as vertical lines, the lineshapes of the spectra are obtained by convolution of Gaussian curves centered at each transition ($\sigma = 85$ meV).

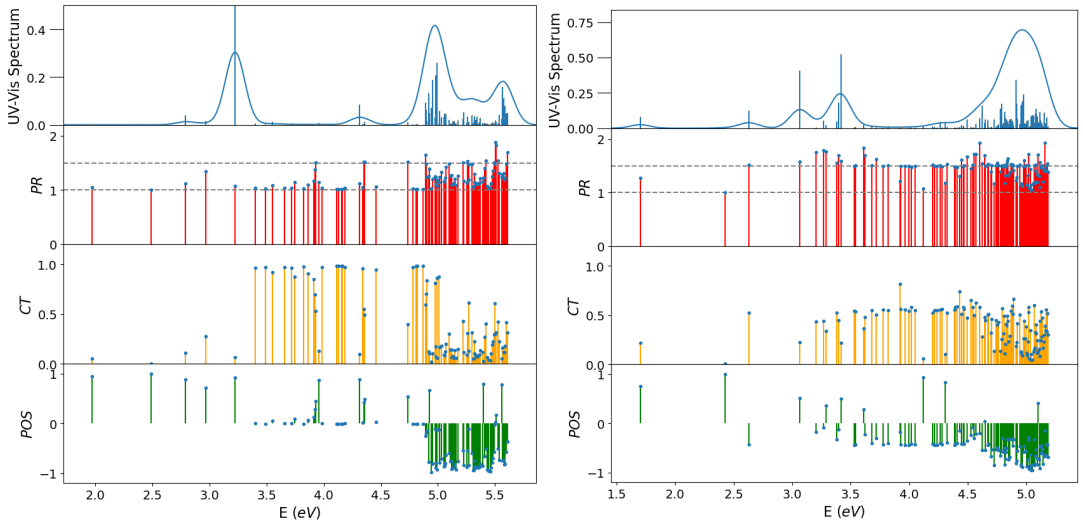

(a) (b)

Figure 4.12: Plot of participation ratio (PR), charge transfer character (CT) and average excitation position (POS) descriptors values together with the simulated absorption spectra of monomers (a) **8D** and (b) **17D**. Position values are shifted as $(POS - 1.5)/2$ to have a clearer visualisation of the position, negative values for fragment 1 and positive for fragment 2.

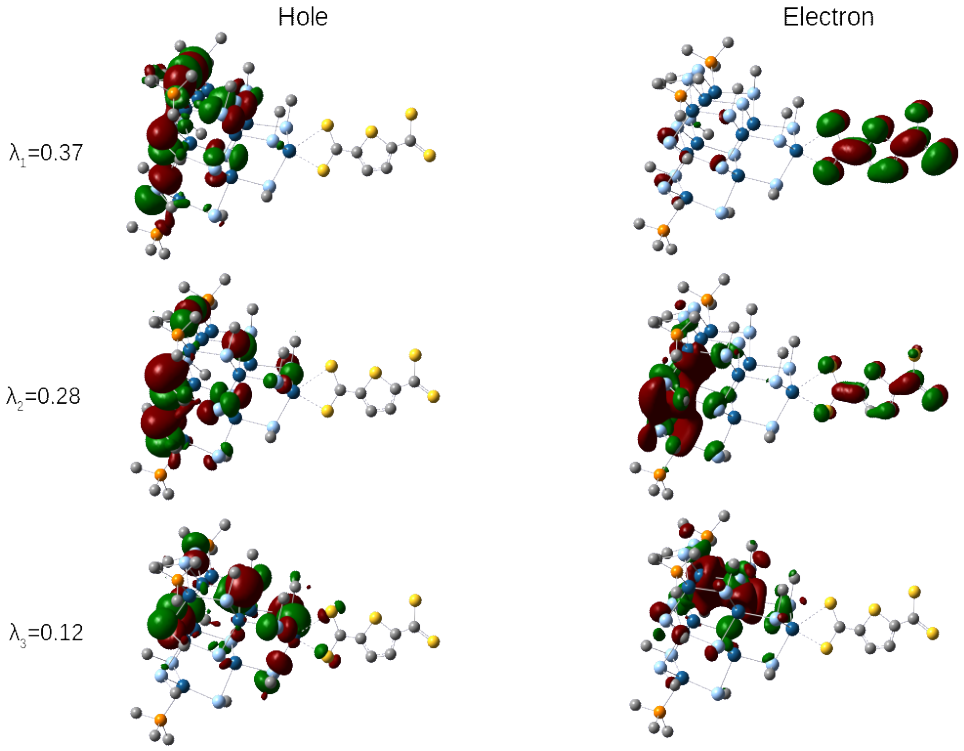

Figure 4.13: Natural Transition orbitals (NTOs) of transition 44 of monomer **10D**. The singular value (λ_i) of every couple is reported on the left, each row representing a couple of hole and electron orbitals.

The CT values oscillate around 0.4, underlining a stable displacement of the electron density upon excitation, and the PR around 1.5 indicates a situation of intermediate mixing between the cluster and the ligand. Sometimes, only the hole or the electron state is delocalised or, especially when PR > 1.5, both hole and electron are delocalised but not equally among the two fragments. Differently from **8D** and **10D**, an overall strong hybrid character of the excited states is clearly visible throughout the whole optical spectrum.

A further evidence of diffuse delocalisation comes from the position (POS) index: the POS is 1 for the cluster fragment, and 2 for the ligand. These values are shifted to -1 for the cluster and 1 for the ligand in all the plots of the indexes, to help having an immediate the visualisation from the graphs. The average value is $\overline{POS} = -0.43$, thus mostly weighted to the cluster, but still generally delocalised.

POS index helps to point to the almost untouched transition of the ligand too, that are still present although the two transitions at 4.11 and 4.37 eV, strongly allowed for the isolated molecule, loose oscillator strength.

The NTO analysis shows one more key difference. The direction of the electron density flow in the charge transfer among the configurations is now from DTMT to **Cd17**. This is a completely different behaviour from the other monomers and therefore to distinguish it we refer to it as inverse charge transfer ICT. This can be appreciated for almost all the excited states, starting from the third transition, the first panel in fig. 4.14, a clear ICT from a small delocalised state to a state localized on inorganic core. Almost fully described by a single couple of NTOs, confronted with the frontier MO in fig. 4.10 they resemble a HOMO-LUMO transition, although they are not the same states.

At higher energy, above 4 eV, the transitions show a higher multiconfigurational degree and PR_{NTO} and can not be described by a single pair of hole and electron orbitals, rather by combinations of multiple NTOs, typically two to four configurations, e.g. transition 40 in the third panel of fig. 4.14.

Lastly, **13D** monomer was studied to investigate the effect of DTMT when bound to a bare inorganic core. Albeit the gap is more than 1 eV smaller, the characteristic of the nature of the transitions is quite similar. The intermediate

region is not present, the ligand-localized and cluster-localized region get closer in energy. The region of the absorption spectrum dominated by the cluster with a contribution of the ligand spans a wider energy range ($3.5 - 5.5$ eV) compared to the other monomers. As a consequence, the charge transfer transitions are more spread throughout the spectrum, with a CT index that varies similarly to how it varies in the other cluster-related bands, entailing an increased transfer of electron density in the direction of the ligand. The CT states appear from the second absorption band, the NTOs of the first and main three transitions of this band are depicted in fig. A.41, the optical spectrum and diagrams of the descriptors are shown in fig. A.4 and fig. A.18.

The analysis of this monomer highlights that the smaller energy gap of the semiconductor cluster is not the key factor to explain the different behaviour of **17D** compared to the other clusters of the homologous series. The main conclusion of this section is that the DMTM shows remarkable capability of exchanging charge with the CdSe clusters. The exciton delocalising properties of the ligand are evident in all the monomers, despite the nature of the CdSe clusters involved (homologous series or MSC **13D**).

4.3.3 Effect of a Different Special Ligand: The Case Of PPNS

The effects of another ligand, the PPNS, on the electronic structure of the clusers are now explored. As we learned by the study of the DMTM ligand that Cd4, Cd8 and Cd10 have a similar behaviour. In this section we will concentrate on two clusters, that is **Cd8** and **Cd17** interacting with the PPNS linker, we will refer to these species as **8P** and **17P**. The PPNS molecule can bind the apical Cd atom in two different ways, with the nitrogen of the pyrrole moiety or through the bidentate $-CS_2^-$ group. Both possible modes will be exploited for building dimers, while in the monomers we use only the binding by the dithiolcarbammate moiety as it is the same type of coordination of the DMTM linker.

The effect of PPNS on the charges distribution, calculated by natural population analysis, is less than what expected, considering the intrinsic push-pull nature of this ligand. Similarly to **8D**, the charge difference between the pris-

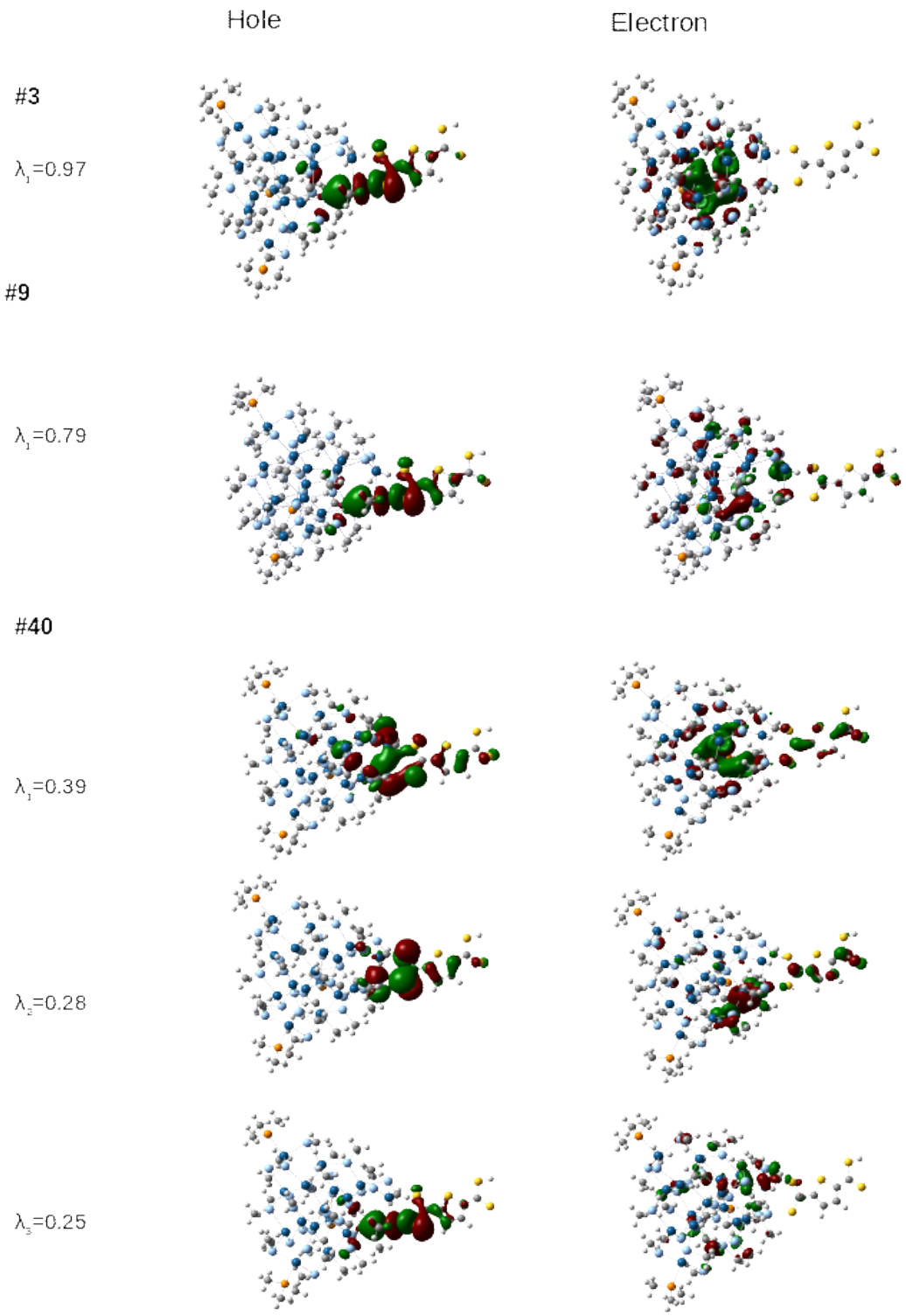

Figure 4.14: Natural Transition orbitals (NTOs) of illustrative transitions, namely 3rd, 9th and 40th transitions, of monomer **17D**. The singular value (λ_i) of every couple is reported on the left, each row representing a couple of hole and electron orbitals. Transition 3 and 9 are well represented by a single couple of NTOs while at higher energies, transition 40th, combinations of NTOs couples are needed.

tine cluster and **8P** is almost negligible, while it seems more efficient as electron density donor when comparing **17P** to 17D monomer (the core is -0.09 *e* more negative than **17D**). This was unexpected because the electron density is supposed to "flow" in the direction S-to-N in the ligand rather than the opposite. In any case the magnitude of the effect is small and it can be ascribed to the increased electronic conjugation in the PPNS molecule, *the electron density a bit looser.*

The composition of the projected densities of states for cluster and ligand is similar to the density distributions previously studied for the DTMT. In **8P** the frontier occupied orbital is localised on the Se centres of the inorganic core, with a little contribution of the ligand through the binding sulfur atoms, while the frontier virtual orbital is fully localised on the PPNS molecule. It is the first of three ligand trap states present within the band-gap of the cluster. Likewise, the DOS of **17P** is similar to the DOS of **17D**, with the disappearance of trap states within the gap. However, more differences are present in the comparison of the PDOS of these two species: the frontier occupied state is no more completely detached from the cluster valence band, but there is a visible narrow band of ligand states close to the cluster states, although it is still internal to the band-gap. The first unoccupied frontier state is a state localised on the inorganic core but the subsequent state is an almost pure ligand state, both slightly separated from the subsequent band of virtual states.

From the investigation of the simulated absorption profile of these two monomers, figs. 4.15 and 4.16, the first observation is that the main peak, associated with the inorganic cluster because of its spectral range, is now red-shifted. Respectively, the shifts are calculated to be -71 meV for monomer **8P** and -44 meV for monomer **17P**. As pointed out for the previous series, the nature of the absorption band is different between pristine clusters and ligand-cluster systems, therefore we do not observe the same transitions shifted to lower energies but rather different ones, that have to be investigated and described considering the associated electronic properties.

Even if the optical spectrum of **8P** shows more allowed transitions along all the energy range, it can still be rationalised by the subdivision into three

zones, using the distribution of the values of the descriptors (fig. 4.17a). The first one, up to 3.75 eV, is related to transitions of the sole ligand, with little contribution of the chelated Cd. The central portion, in the range 3.8 to 4.8 eV, transitions are mostly cluster-to-ligand charge transfer and hybrid state to ligand transitions. The oscillator strength of the localised charge transfer states, and its enhancement for the partially hybrid transitions, is given by *intra* PPNS transition configurations. The high energy region of the spectrum, above 4.9 eV, is related to a mixture of cluster transitions and hybrid cluster-ligand state, where the contribution of the ligand is enhanced compared to the DMTM.

The push-pull character of the ligand induces more charge transfer states, and also there is the presence of more hybrid states. This is clearly visible from the CT and PR descriptors, the average of both increased respect to monomer **8D**. A deeper understanding of the way the ligand affects the electron density can be achieved by the study of the hole and electron distribution through the inspection of the associated NTOs. In particular, it is interesting to see how the hybrid character of the states increase along the spectrum and how the visualisation of more transitions in the spectral range helps to highlight the push-pull sling behaviour of the system, a sort of drain of electron density by PPNS. Selected NTOs for the three regions of the spectrum are displayed in fig. 4.18. Transition 5 is the first pure charge transfer transition, identified by PR=1.064 and CT=0.939, the position of the excitation (POS=1.499) describes an exciton equally shared between cluster and ligand. The 19^{th} excited state is visible as the third absorption peak, the second strongly allowed absorption, at 4.46 eV. Expected to be a transition of the sole ligand by the comparison of the spectra, potentially with a marginal contribution of the portion of the inorganic cage bonded by the sulfur centres, it shows a strong hybrid contribution by a configuration where the hole is delocalised among the entirety of the fragments, the singular value of this NTO is $\lambda_2 = 0.40$, even if the principal NTO is localised on the ligand with weight $\lambda_1 = 0.60$. At higher energies (> 4.9 eV), the delocalisation effects are even more present, and more NTOs are needed to describe the transitions. For example, transition 34 has PR=1.873 and CT=0.307 and it needs three NTOs: the first one ($\lambda_1 = 0.47$) is a transition between delocalised states with an observable displacement of the

electron density towards the ligand, the second ($\lambda_2 = 0.22$) is a transition between a delocalised hole to a ligand-localised electron and the third contribution with an appreciable coefficient ($\lambda_3 = 0.09$) describes a cluster-to-ligand charge transfer state.

The optical spectrum of **17P** resembles more the sum of the spectra of its two components, fig. 4.16 compared to the spectra of 8P and 17D. This is reflected by the numerical descriptors fig. 4.17b which confirm a more limited mixing between the cluster and the PPNS ligand states in the 17P. For example, we notice the disappearance of the states with high CT which characterizes the central region of the spectra of the other species and a general lowering of the value of CT values (average $\overline{CT} = 0.141$). The values of the participation ratio index are slightly lower than **8P** monomer and markedly lower than the 17D which is the same cluster interacting with the DTMT ligand.

This limited mixing comes somehow unexpected because (i) among all the considered clusters, the **Cd17** showed a high tendency toward hybridization of states with the DTMT ligand and (ii) by analyzing the **Cd8** cluster, we saw that the PPNS ligand is more effective in delocalizing the charge compared to the DTMT.

To understand the reason underlying the limited hybridization in the **17P** cluster, the visualisation of the NTOs of the transitions is enlightening. It helps to understand why the optical spectrum is different from our expectation based on the behaviour of the other ligand and the other cluster. First, we can still divide the spectrum of 17P into the three regions we found characteristic of all these systems. The first region, up to 4.2 eV, before the second visible band, is related to transitions of the sole PPNS and is not further interesting. In the first portion of the second band, two transitions with the ICT feature can be appreciated, similar to the characteristic transitions of **17D**. Among cluster related transitions, in the central part of the second band and at higher energy, we find a peculiar combination of configurations which recurs for many transitions. Two main NTOs pairs participate, with comparable weights, to a resonance of charge transfer states, similar to the situation displayed in the ideal dimer in figs. 3.1 and 3.2, and a clear example is shown in fig. 4.19. As we see, all the

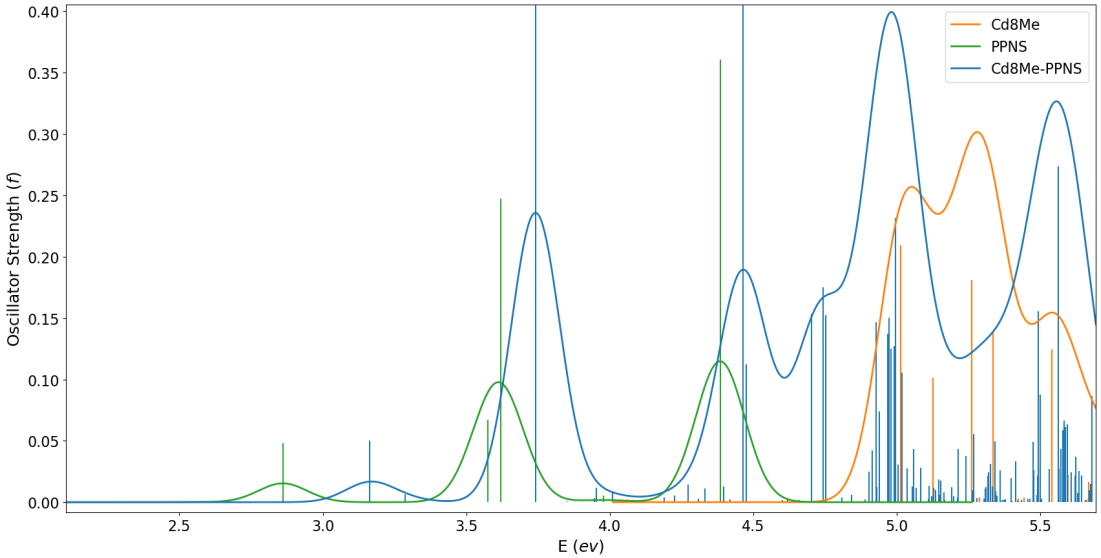

Figure 4.15: Comparison of simulated optical absorption spectra of monomer **8P** (blues) and its isolated fragments, pristine cluster (orange) and ligand anion form (green). Computed transitions are plotted as vertical lines, the line-shapes of the spectra are obtained by convolution of Gaussian curves centered at each transition ($\sigma = 85$ meV).

states involved are not purely localised either on the inorganic core or the special ligand, rather they are partially delocalised states, accounting for the increasing of PR index that deviates from 1 and the significant lowering of CT, as the transition is far from being a pure CT state. Still, the competition of charge transfers in opposite directions picture can be recollected in many transitions such as transition 26 displayed in fig. 4.19, and in particular when studying all the NTOs of the band and considering them as an intuition for the behaviour of the band considered as a whole.

We consider this particular behaviour to be due to the effect of the push-pull ligand, by which effect the two opposite charge transfer processes become competitive.

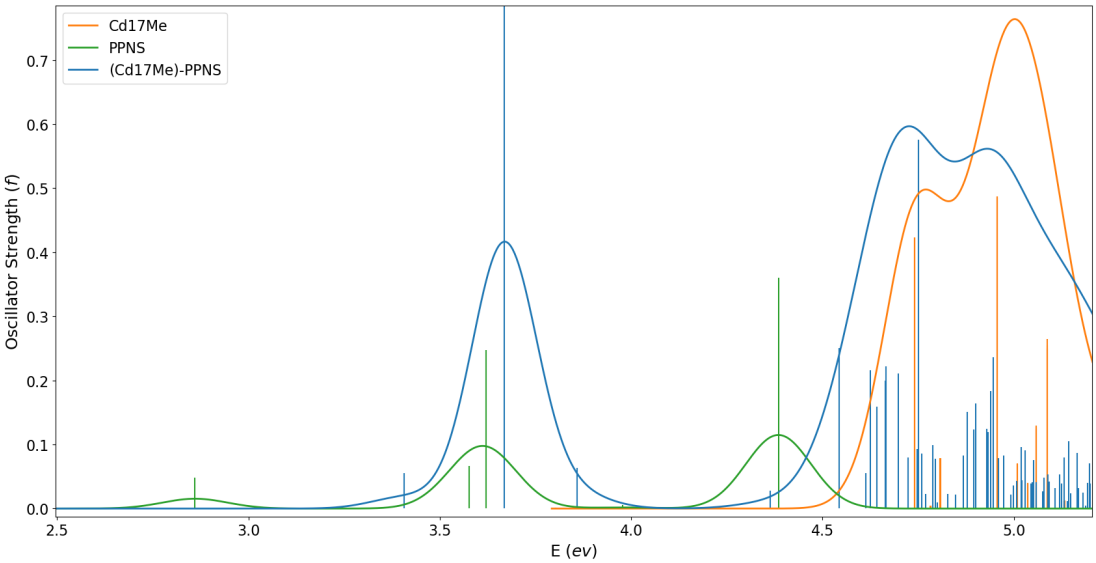

Figure 4.16: Comparison of simulated optical absorption spectra of monomer **17P** (blues) and its isolated fragments, pristine cluster (orange) and ligand anion form (green). Computed transitions are plotted as vertical lines, the line-shapes of the spectra are obtained by convolution of Gaussian curves centered at each transition ($\sigma = 85$ meV).

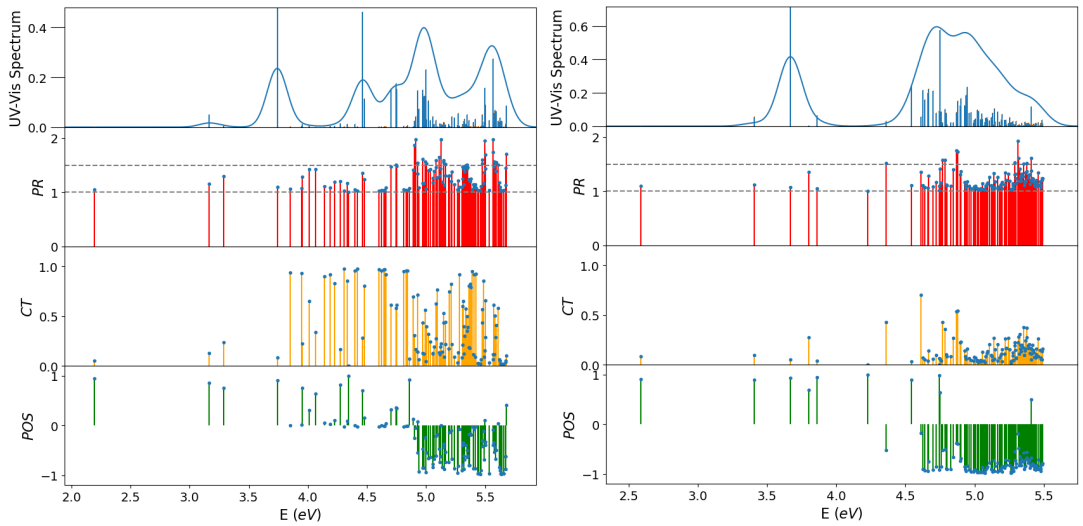

(a) (b)

Figure 4.17: Plot of participation ratio (PR), charge transfer character (CT) and average excitation position (POS) descriptors values together with the simulated absorption spectra of monomers (a) **8P** and (b) **17P**. Fragments are assigned to the cluster unit one and to the PPNS ligand the other.

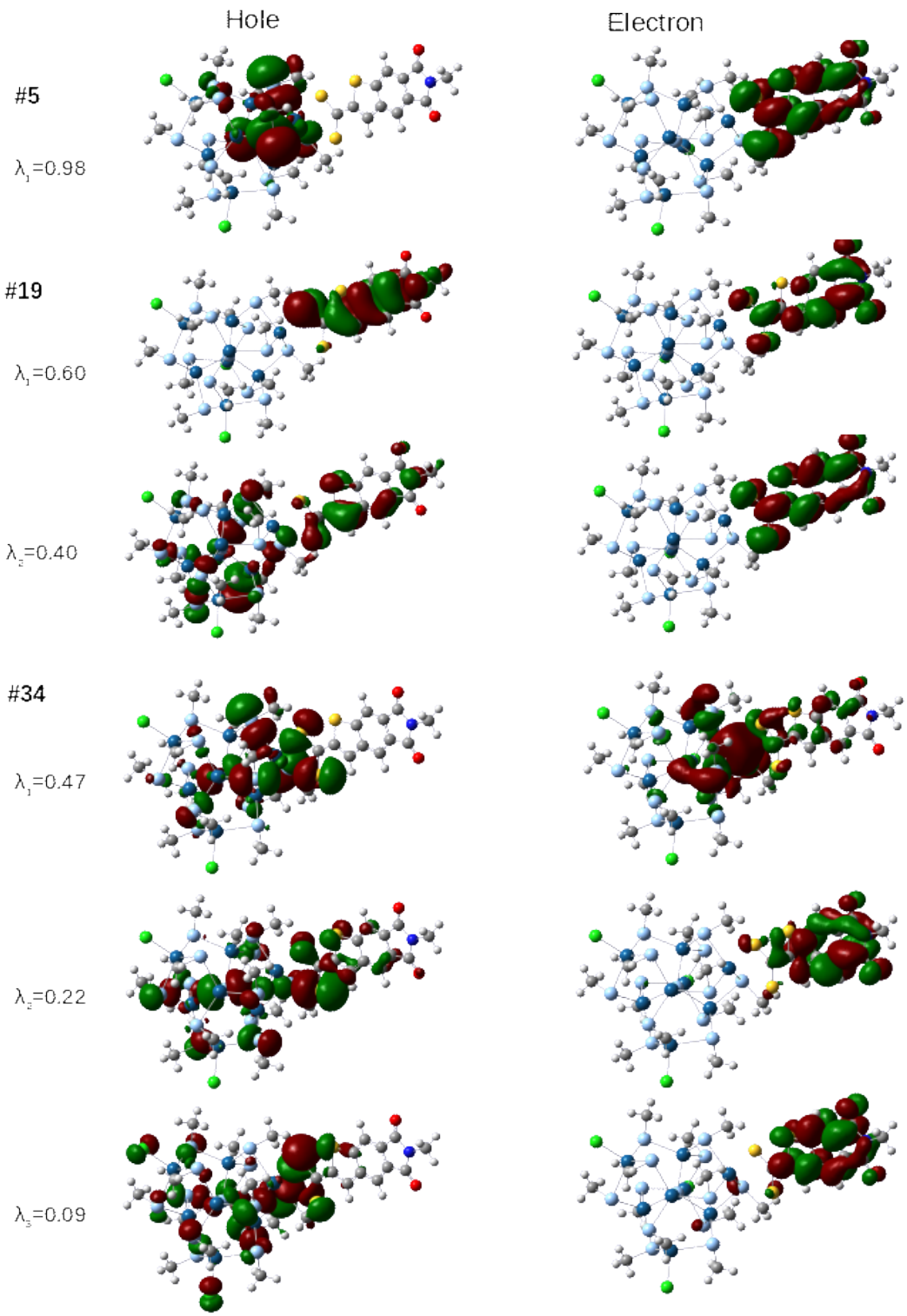

Figure 4.18: Natural Transition orbitals (NTOs) of transitions 5, 19 and 34 of monomer **8P**. The singular value (λ_i) of every couple is reported on the left, each row representing a couple of hole and electron orbitals. The draining effect on the electron density is clearly visible, as well as the trend in the increasing of delocalisation of the states, together with the necessity of more NTO pairs to describe higher energies transitions.

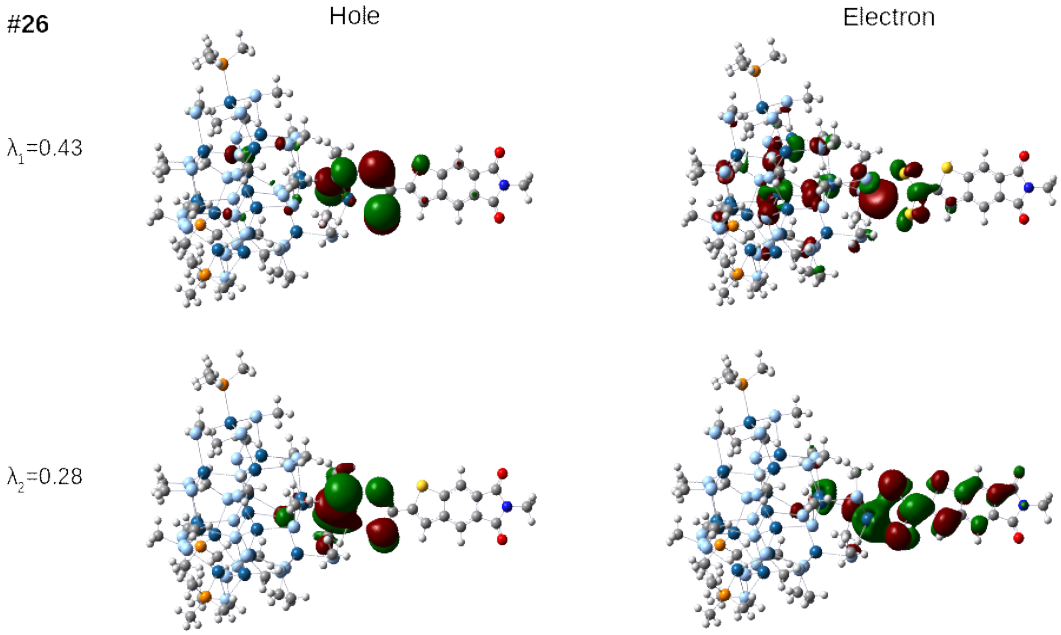

Figure 4.19: Natural Transition orbitals (NTOs) of the 26th transition of monomer **17P**, as an example of a charge resonance hybrid state. In the first pair of hole and electron orbitals representations

4.4 Dimers of Clusters

In this Section, we discuss the electronic structure and the topology of the excitations upon aggregation of our clusters in dimers mediated by a covalent bridging ligand. Throughout this investigation all the homodimers linked by a single DTMT molecule are studied, fig. 4.20, while with PPNS as spacer only one homodimer is studied as a test to isolate the intrinsic effect of the ligand on two equal units. Then an engineered heterodimer is built to obtain the maximum enhancement of directional charge transfer, an electron transfer process (ET) that relies only on the photo-excitation in its early step,[151] that might shows coherent ET signaturs.

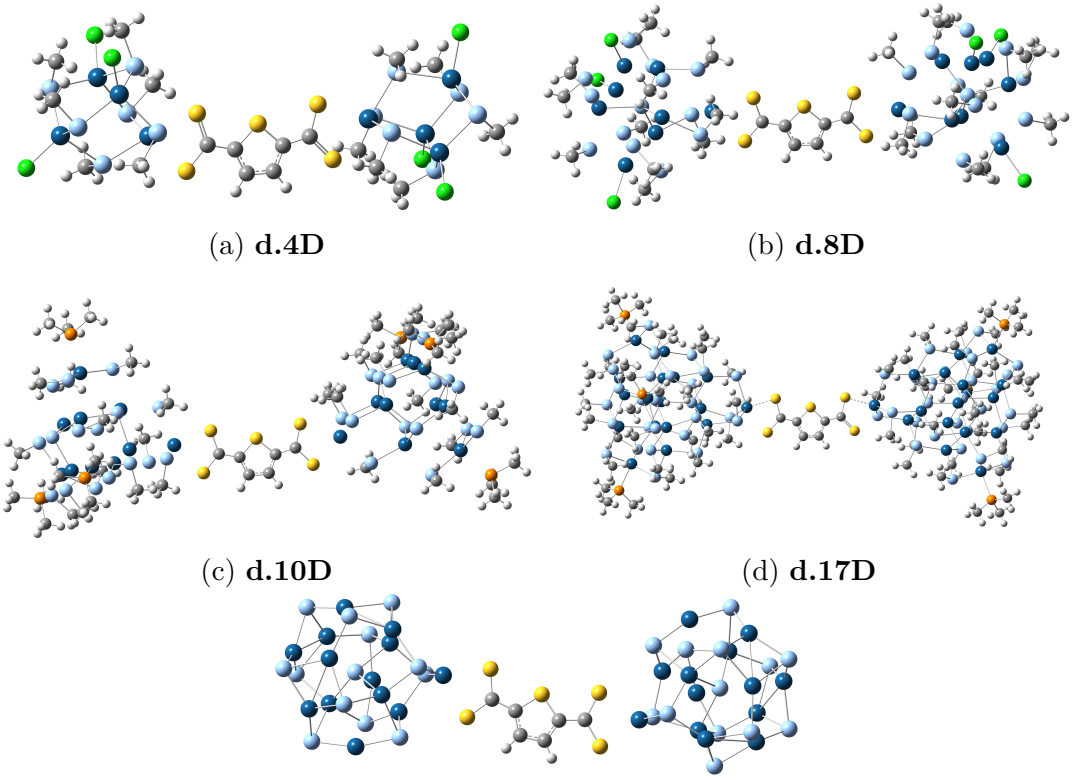

(a) **d.4D** (b) **d.8D**

(c) **d.10D** (d) **d.17D**

(e) **d.13D**

Figure 4.20: Optimised geometries of the homodimers computed at B3LYP theory level with the mixed basis set LANL2DZ/LANL2DZ(dp)/6-31G(d).

4.4.1 Homodimers

From the optimisation calculations only minor differences in terms of geometry are present between dimers and their monomers. All the dimers are in a minimum

of PES corresponding to a staggered conformation, considered with respect to the apical ligands of the two tetrahedra and looking along the axis of the bridge. The bond length between the chelating sulfur atoms and the chelated cadmium are substantially unchanged, 2.75 Å for dimers **d.4D**, **d.8D** and **d.10D**, and 2.70 Å for dimers **d.17D** and **d.13D**. The aggregation induce a more symmetric binding of the chelating moiety of the ligand whereas in the monomers the bond lengths of the two sulfurs are one slightly shorter than the other (2.7 Å and 3.5 Å). The distances between the inorganic clusters in the dimers are comparable, namely, 1.15 nm for **d.4D**, 1.18 nm for **d.8D**, 1.16 nm for **d.10D**, 1.13 nm for **d.17D** and **d.13D**, calculated as the distance between the chelated cadmium atoms.

The DOS of all the dimers built with clusters of the homologous series presents similar features, flattening the diversity present between the monomers. The occupied frontier orbitals show in all cases a remarkable participation of the bridge in a similar fashion to what observed in the **17D** monomer. The analysis of the HOMO of these systems shows two degenerate states, hybrid between the cluster and the bridge with symmetric participation of one unit and the other. The DOS and MOs of **d.8D** are shown in fig. 4.21 as an example. Likewise, the LUMO orbital is localized on the bridging ligand also for the dimer of **Cd17** clusters, with the only difference that it is not isolated as a trap state within the gap but it is close to two degenerate states of the inorganic cores.

The first point we addressed is the possible delocalisation of the excitonic states over the two cluster units. In our previous study on dimer of **Cd13** cluster we indeed found an extended delocalisation of the excitons of the first band. To see if this the case also for the homodimer of the homologous series we consider the two inorganic cores as the two fragments and the ligand equally shared between them. This subdivision helps to identify those states that are resonances of Frenkel excitons, which are characterized by the indexes PR=2 and CT=0. Such coupled states would give two transitions whose energy difference denotes the coupling strength between the two clusters and with a redistribution of intensity, in complete analogy with the simple model of a dimer of two level systems described by Kasha.[93] As an alternative, resonance of charge transfer states are identified by the indexes PR=2 and CT=1, as depicted in Chapter 2 and section 3.3.

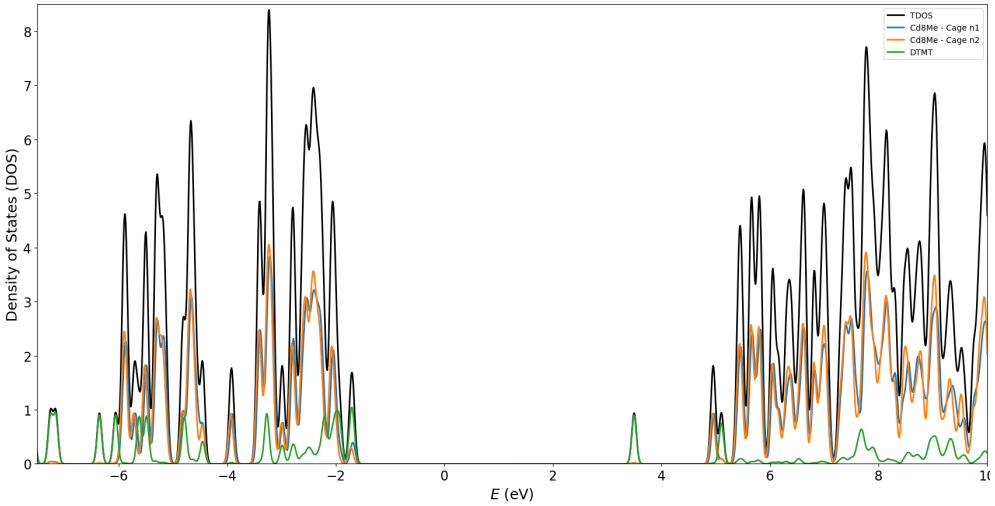

(a)

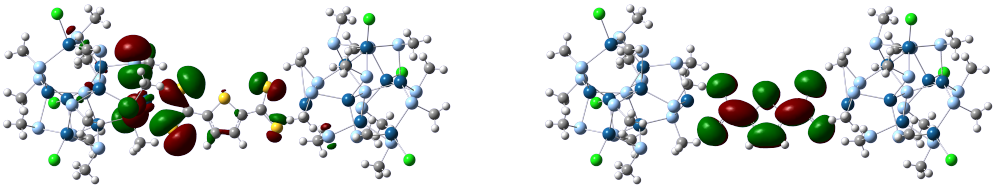

(b) (c)

Figure 4.21: (a) Computed DOS of the **d.8D** homodimer (solid black line), projected density of states of the two cluster units (blue and orange lines) and of the bridging ligand (green) are shown. (b) HOMO of **d.8D**, specular to the almost degenerate HOMO-1. (c) LUMO of **d.8D**, a trap state localised on the ligand.

Despite the clear capacity of the ligand to delocalise the excitation in the monomers, in particular for monomer **17D**, no such delocalised states are observed in the first cluster-related absorption band for none of the dimers belonging to the homologous series (with the exception of a single transition in **d.8D**). What is observed instead, from the NTOs analysis, is a general localisation of the excitation back to the cluster units. Even if cluster/ligand hybrid states are still present, they are mostly of charge transfers character, from one cluster to the ligand or concerted from both the clusters to the ligand. Hybrid delocalised state and combinations of configurations involving both the cluster units are indeed present only at higher energies, in the tail of the first cluster-related band, and the transitions at even higher energy are local transitions localised on the clusters only.

Since the analysis above shows a possible localisation effect, we divided the system according to a second partition scheme to get further insights. In this

	Monomer		**Dimer Part. 2**		**Dimer Part. 1**	
	PR	CT	PR	CT	PR	CT
d.4D	1.373	0.393	1.381	0.315	1.245	0.197
d.8D	0.393	0.387	0.315	0.288	0.197	0.155
d.10D	1.199	0.277	1.222	0.187	1.230	0.103
d.17D	1.450	0.385	1.286	0.195	1.328	0.101

Table 4.3: Mean values of PR and CT indexes for the monomers and for the two different partitions of the dimers. Partition 2 is presented first because allows the direct comparison to the monomer, as it consist in both the core in one fragment and the ligand in the other. In partition 1 the cores are the fragment and the ligand is equally split.

partition one fragment contains both the clusters, while the other includes only the bridging ligand. We can therefore compare the delocalisation among clusters and bridging ligand in monomer and dimer. The clusters in the dimer are almost identical, with small differences in geometry due to a different relaxation of the structures. Considering then both the inorganic cores as a single fragment, we observe the behaviour of one cluster interacting with its organic ligand when they are part of an aggregate.

It also allows us to have numerical values to quantify the localization effect we notice by the visual analysis of the NTOs, by computing the mean values of the PR and CT values for all the monomer and dimer transitions. We recall that PR>1 when either hole or electron are delocalised on the two fragment and CT>0 when hole and electron are localized on different fragment. Therefore the mean $\overline{PR}$ describes the average delocalisation of electron and hole states. However, taking into account that in the monomers the bridge is involved mainly in charge transfer states, the mean $\overline{CT}$ is the most significant parameter to compare in monomers and dimers. The average values of both the indexes are displayed in table 4.3. From the comparison of the $\overline{CT}$ of the monomers and the dimers in the second partitioning scheme, it is evident an increasing localisation of the exciton in the inorganic core going from from **d.4D** to **d.17D**. In particular for this last dimer the difference is significant and it can be appreciated from the simulated optical spectrum, fig. 4.22. The optical features of the monomer **17D** disappear in the dimer, which resembles more the sum of DTMT and pristine cluster isolated spectra, with little interactions.

Notice that this second partition scheme does not highlight exciton delocal-

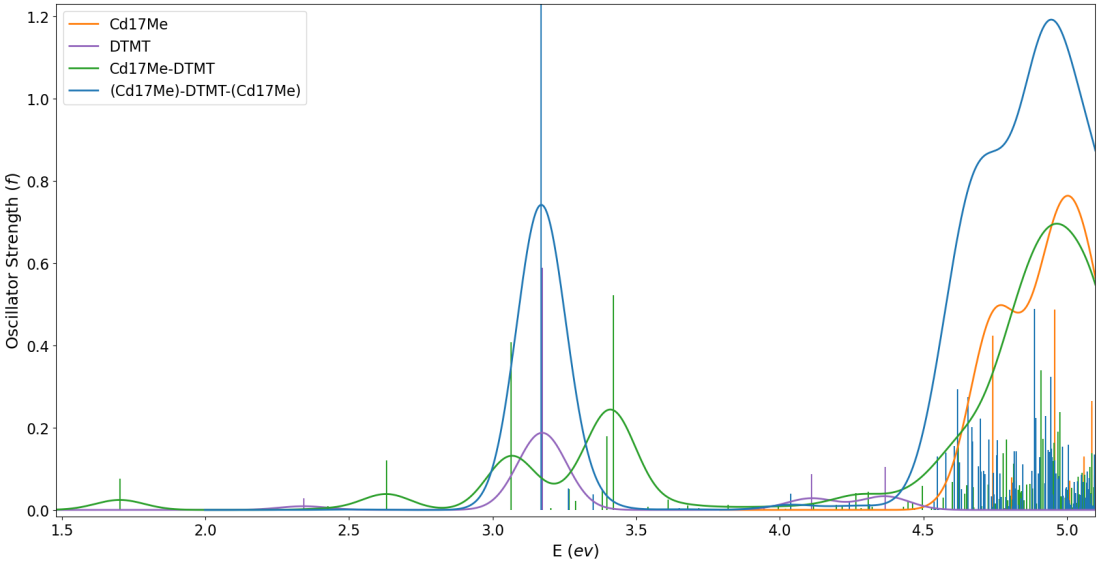

Figure 4.22: Simulated optical spectrum of **d.17D** dimer in blue, its monomer spectrum in green, the isolated cluster and ligand units respectively in orange and purple line.

isation between the two clusters, as e.g. Frenkel resonance states, therefore the two partitions give complementary information on the exciton topology.

By the analysis of the indexes associated to the other partition and the visualisation of the NTOs of the states with high PR values, we found also in this dimer delocalised states that strongly resemble Frenkel excitons in the dimer model of Kasha. However, these delocalised states are present only at high energies, differently from the dimers studied in ref. [25] where the electronic coupling between the two cores mixes the states of the first band. Second, the coefficients of these NTOs are small, the overall contribution of the actual Frenkel combination accounting for about only half of the transition, if not less (e.g. transition 68 of **d.8D** with coefficients $\lambda_1 = \lambda_2 = 0.14$ and transition 50 of **d.17D** with $\lambda_1 = 0.25$ and $\lambda_2 = 0.16$). If we calculate the electronic coupling between the two clusters by measuring the energy difference of two coupled excitons we can conclude that such a coupling is very small, in the order of few meV.

As in the dimer of the magic number clusters **Cd13** formed by the PDTC bridge, we did observe coupling of the lower energy excitonsref. [25],, we decided to analyse what happens linking the same clusters with the DTMT bridge in the dimer**d.13D**. This dimer is formed by two cages of **Cd13**, which we recall are uncapped inorganic cores with spherical symmetry and even stoichiometry.

The first absorption band related to the clusters is not shifted respect to the monomer case but the nature of the transitions changes considerably. A clear localisation of the excitation to the inorganic cores is indeed visible, just as in the previous dimers, the participation of the ligand visible only as a two cluster to ligand charge transfers almost dark transitions at 3.62 eV and then in the second band, above 4.2 eV. Focusing only on the first cluster absorption band (which is the second band in the spectrum of figs. 4.23 and A.11), the first two transitions have mixed charge transfer character from the cores towards the ligand. The subsequent absorption lines are present in pairs of close lying transitions: the first and the last pairs, namely transitions 8-9 and 12-13, are transitions localised on only one of the inorganic core, the pairing due to the imperfect degeneracy of the cores energy levels arising from slightly different geometries. The transitions 10 and 11 are, instead, a pair of Frenkel excitons, a coherent superposition of localised transitions, combined with opposite phase. The NTOs relative to this two transitions are displayed in fig. 4.24. From the singular values of the NTOs decomposition we observe that this are not pure Frenkel states, but other minor contributions are present. Overall, the behaviour of this dimer is consistent with what observed in other weakly coupled dimers, as for the dimers linked by a PDTC molecule, but with a much lower tendency to delocalize the exciton over the two units. The electronic coupling J between the two units can be calculated as half of the energy separation between the coupled local excitons transitions, as discussed in Chapter 2. The splitting between the coupled transitions is 2.6 meV, leading to a very weak coupling of 1.3 meV.

The last consideration to the analysis of this dimer is that, due to the re-localisation of the excitation back to the inorganic cluster units, it is possible to evaluate and comment the other contribution which may contribute to the spectral shift of the dimer compared to the bare cluster. From the bare cage **Cd13** to the dimer **d.13D** a significant shift of 229 meV to the blue is observed, fig. 4.23. Since the ligand is poorly coupled, and the clusters have a weak Coulomb coupling that accounts for only 1 meV, this is attributed to the polarization effect of the negative charge of the ligand.

To summarize, when the ligand interacts strongly in the dimer we expect a

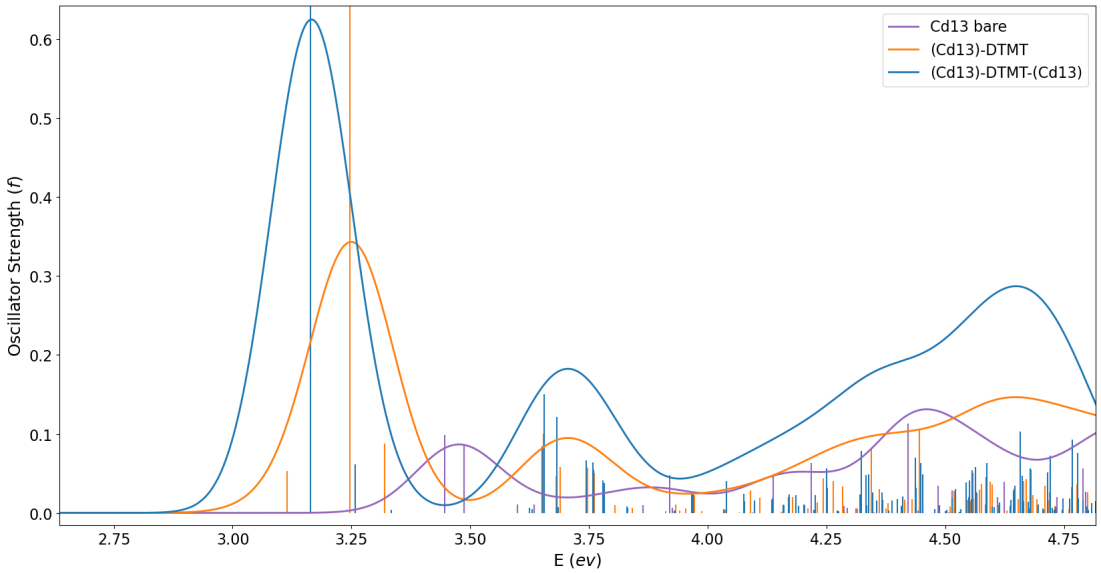

Figure 4.23: Comparison of simulated optical absorption spectra of dimer **d.13D** (blue), its monomer **13D** (orange) and the bare cage **Cd13** (purple).

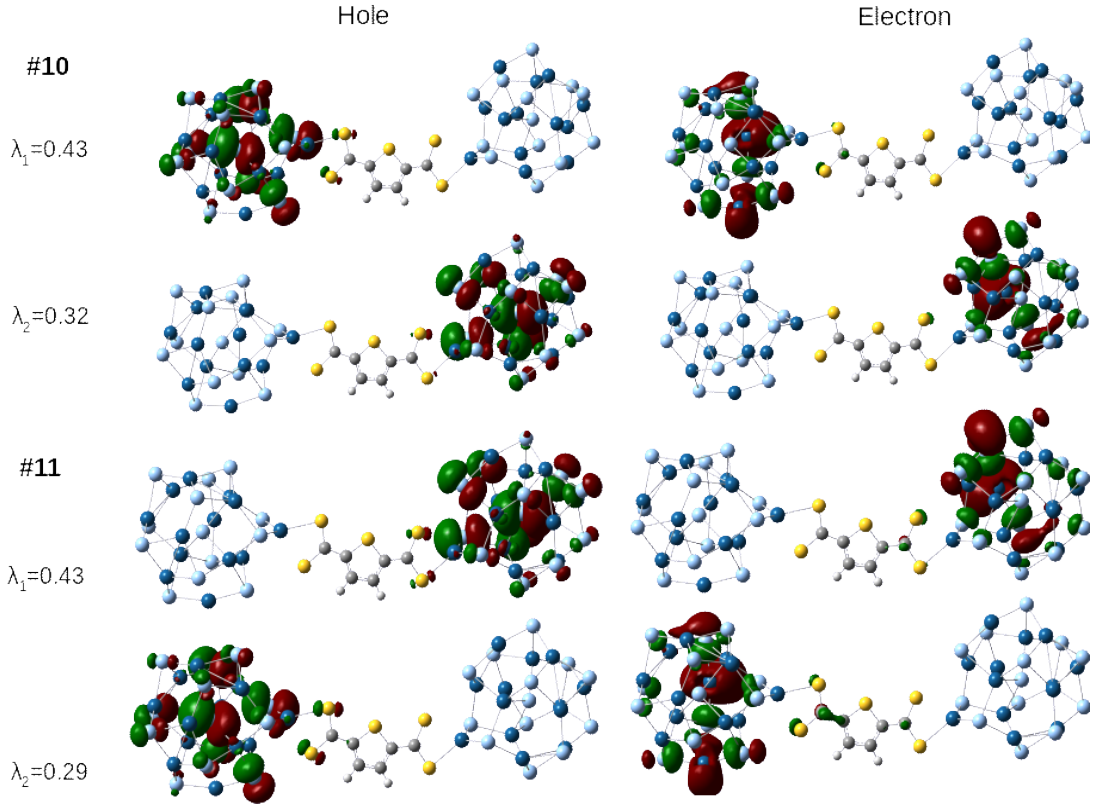

Figure 4.24: NTOs of transitions 10 and 11 of dimer **d.13D**, representing the pair of Frenkel excitons combinations.

stronger coupling between the clusters units, mediated by the ligand itself.

When the ligand poorly interacts, Frenkel states are still possible to observe but with small splitting, with no or negligible contribution of the bridge, as for dimers with PDTC.

In the case of the capped dimers of the homologous series, linked by a DTMT molecule, and in a different way but with similar effect in the case of the **d.13D** dimer, we observe that the presence of the second inorganic unit reduces the delocalisation between cage and ligand, resulting in a poor coupling between the units.

In other words, we observe a localization of the excitons back to the inorganic cores upon aggregation. Moreover, the tendency of the DTMT to establish charge transfer states with the clusters rather than delocalised hole and electron states diminishes the delocalisation of the exciton over the dimer.

4.4.2 Engineered Push-Pull Heterodimer

Because of the encouraging behaviour observed in the monomers with PPNS, **8P** and **17P**, we have built a model for an engineered heterodimer to test the enhanced capacity to transfer an electron from one unit to another mediated by the ligand.

As reference we also consider the corresponding homodimers linked by PPNS to observe the intrinsic effect of this different bridge. It is formed by two **Cd8** units bonded by the dithiolate end and by the nitrogen atom at the other end of the bridge.

The DOS of this homodimer, **d.8P**, shows that the frontier occupied orbital is a hybrid state of the clusters bonded by the dithiolate end and the ligand, while for the monomer it is localised mostly on the inorganic cage with little contribution of the sole binding sulfur atoms, visible from the HOMO. The first virtual state is again, similarly to the monomer, a trap state associated with the ligand, within the gap of the clusters states. Then three states are present, almost degenerate, separated in energy by 35 and 40 meV, associated in order to orbitals localised on the **Cd8** cluster bonded by the dithiolate, on the cluster bonded by the nitrogen and on the PPNS bridge, figs. 4.25 and A.39.

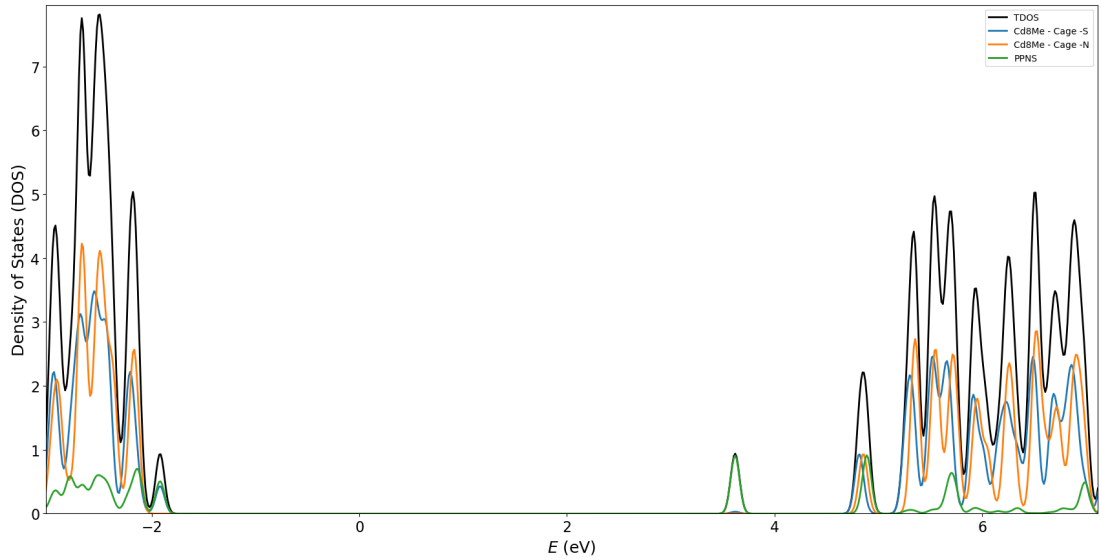

Figure 4.25: Total density of the states (black line) and projected density of the states for the dimer **d.8P**. PDOS of the ligand in green, the cluster chelated by the dithiolate extremity in blue and the cluster bonded by the nitrogen in orange. Note the mixed contribution of the solely S-chelated cluster with the ligand to the occupied frontier orbital.

We analyse the descriptors of the excitations character in both the partitioning schemes discussed above, figs. 4.26a and 4.26b, and the NTOs describing each transition. We note that, as for the dimers with DTMT, the mean $\overline{PR}$ and $\overline{CT}$ values are decreased after the formation of a dimer, but at the same time both the descriptors have higher values for the partition where the two clusters form a unique fragment, showing that the contribution of the ligand is not negligible.

Indeed, we observe that the aptitude of the ligand to accept electron density from the clusters is still present. Some transitions show a charge transfer with the participation of both the clusters to the hole state and the electron localised on the ligand, and other even a charge transfer from the cluster bonded by the nitrogen (ideally the pull portion of the dimer) to the PPNS ligand. This does not surprise, and it shows clearly that the ligand alone is not enough to convey an electron transfer between clusters.

Nevertheless, signatures of the influence of the push-pull ligand are visible from the observation of states that, whether hybrid or with a contribution of particular NTOs pairs, show a particular propensity of the ligand to accept and move electron density from the S-bonded cluster to its nitrogen end, mainly present in the spectral regions in the ranges 4 to 4.5 eV and from 5 to 5.3 eV.

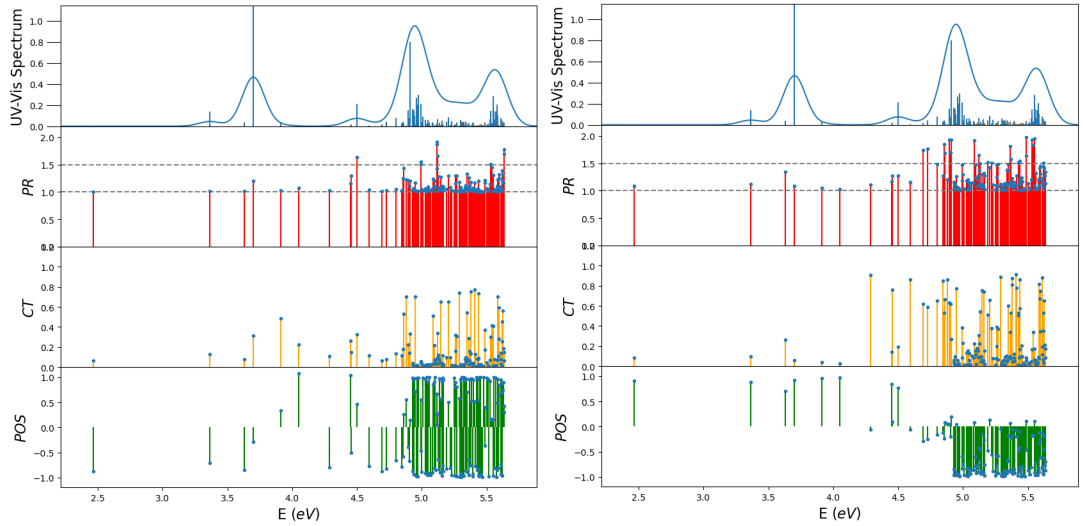

(a) (b)

Figure 4.26: Optical and descriptors spectra for the **d.8P** dimer, with two different partitioning schemes. In (a) the system is split along the horizontal axis of the central benzene ring, resulting into two fragments each carrying one cluster and half of the bridging ligand. In (b) the fragments are assigned one to the two clusters and the other to the ligand, to better visualise the hybridisation and charge displacement towards the organic molecule.

This tendency is reflected in the NTOs of several transitions.

The actual push-pull heterodimer **d.H** is built by replacing the cluster at the N-extremity of the PPNS with the acceptor cluster **Cd17**. The simulated optical spectrum shows unique characteristic compared with all the other spectra we have studied up to now. The first transition is at 0.68 eV, and it is the first of a set of 36 complete charge transfer dark transitions, then the first optically allowed transitions form a band at 2.56 eV, by the Gaussian broadening of the single 37^{th} transition, and a band with a maximum at 3.17 eV,

Due to the presence of charge-transfer transitions at very low energies for this dimer, a CIS (configuration interaction singles) calculation has been done, and the spectrum compared to the one computed with the TD-DFT method, fig. 4.27. This because it is known that DFT methods tend to underestimate the energy of CT transitions, which are better described by taking into account the full exchange interaction as in post Hartree-Fock methods. The analysis of the obtained spectrum and of the comparison shows that the CT transitions are well described by the CAM-B3LYP functionals, and laterally that the de-excitation configurations considered in the TD-DFT have little influence to the

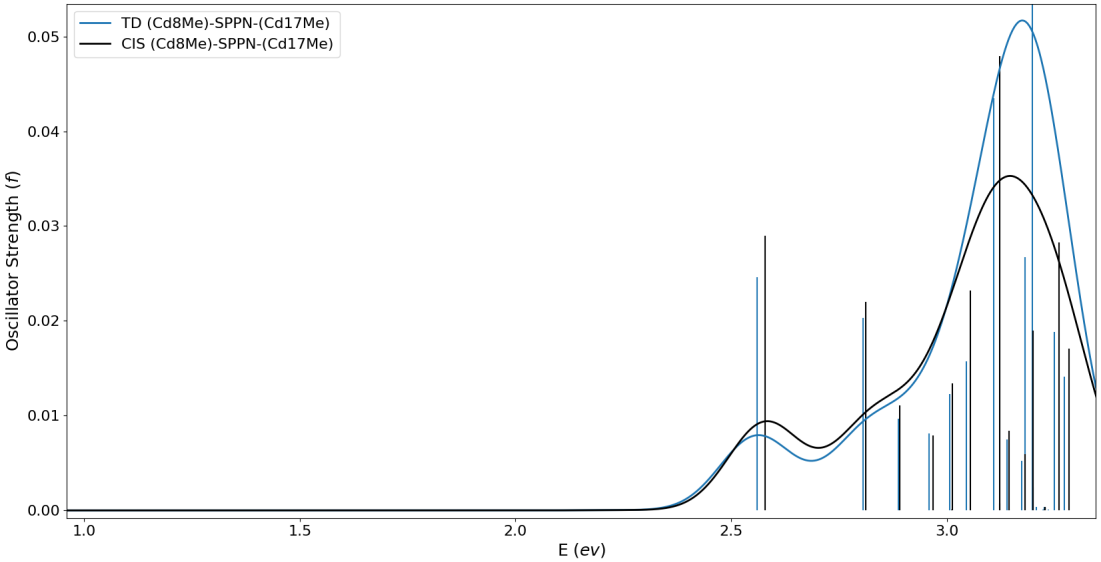

Figure 4.27: Simulated optical transitions of the **d.H** dimer using TD-DFT methods at CAM-B3LYP theory level (blue line) and using the CIS approach (black line).

overall behaviour of the transitions.

Confirmed the validity of the CT transitions, we now analyse the NTOs of the various excitations, given that the indexes are almost constantly PR=1 and CT=2 and hence we expect pure charge transfer states.

The visual analysis of the transitions shows unambiguously that an effective and complete charge transfer happens in all the dark states, described by a single NTOs pair with weight almost unitary ($\lambda > 0.98$). The hole is localised on the **Cd8** monomer and the electron on the **Cd17** unit, an example in the first panel of fig. 4.28.

The concern is now to understand the role of the bridging ligand as funnelling of the excitation flow. Little evidence supporting this idea is present, nevertheless there are indeed states that do support it. In the second and in the last panel of figure fig. 4.28, two of the states that show the participation of the ligand are displayed. One of the problems is that the number of computed transitions is not sufficient to give a complete picture of the charge flow. Indeed, NTOs shows that the higher energy optically active transitions have still the character of the cluster **Cd17**, that is the acceptor, and none localised on the **Cd8** core which absorbs at higher energy. These considerations point to the necessity to compute more excited states, to appreciate the band related to the monomer **Cd8**, because of the arising of so many low energy transitions.

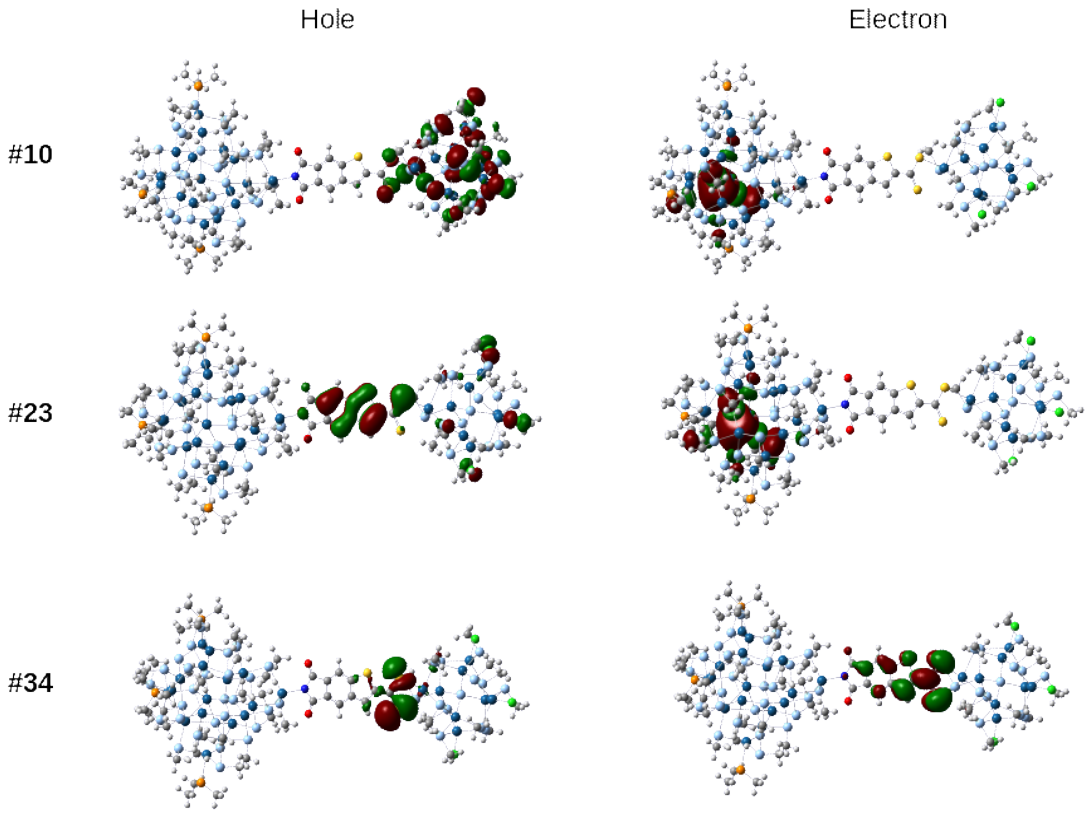

Figure 4.28: NTOs pairs for selected example transitions 10, 23 and 34. In the first panel a charge transfer transition, from **Cd8** to **Cd17**. In the second panel an hybrid charge transfer showing a major contribution of the ligand, maintaining the displacement from **Cd8** to **Cd17**. In the third panel a transition with oscillator strength shows the push-pull nature of the ligand. The singular values are not shown as they are approximated as unitary.

Chapter 5

Ultra-fast Electronic Populations Dynamics

In this last Chapter we want to give the basic theoretical background of the formalism to describe the time evolution of a quantum system, to then simulate the dynamics of the populations of the electronic states of our systems when interacting with a lasers pulse. First, the numerical implementation is tested with a simple excitonic dimer model, then the scheme is applied to the dynamics of the excitation of dimer **d.8D** and the charge density difference between the ground state and the final superposition of excited states is evaluated.

5.1 Theory

The time evolution of an isolated quantum system can be obtained by the solution of the time dependent Schrödinger equation (TDSE):

$$i\hbar\frac{\partial}{\partial t}|\Psi(\mathbf{r},t)\rangle = \hat{H}(\mathbf{r},t)|\Psi(\mathbf{r},t)\rangle \tag{5.1}$$

where $|\Psi(\mathbf{r},t)\rangle$ is the wavefunction describing the system at time t and $\hat{H}(\mathbf{r},t)$ is the possibly time-dependent total Hamiltonian. eq. (5.2). For a molecular system interacting with an optical field, the total Hamiltonian is the sum of a constant term H_0 that describes the isolated system and a time dependent perturbation term that describes the interaction of the electronic distribution of the system with an external electromagnetic field $\mathbf{E}$(**r**,t).

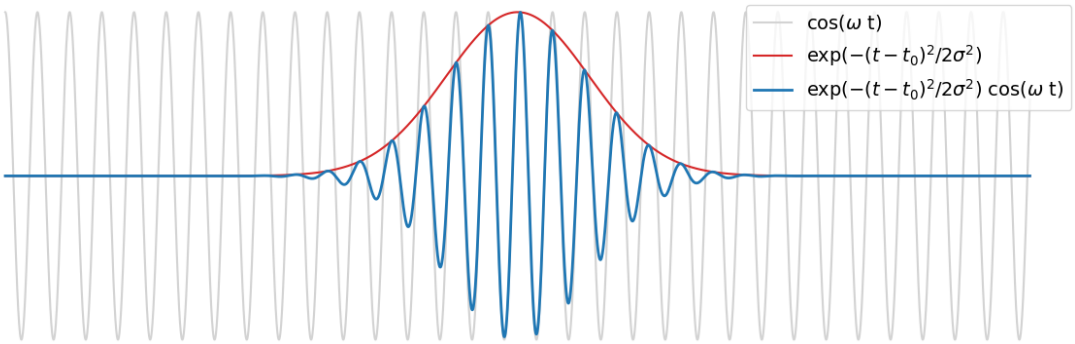

Figure 5.1: Simulated laser pulse with its two components plotted, cosine oscillating function is light grey and the Gaussian function in red. The pulse (blue line) is the convolution of these two functions.

In the dipolar approximation this Hamiltonian reads:

$$\hat{H} = \hat{H}_0(\mathbf{r}, t) + \underline{\boldsymbol{\mu}}\mathbf{E}(t) \tag{5.2}$$

In this particular case, we model an ultra-fast laser pulse as the external electromagnetic field $\mathbf{E}$(t). Hence, the pulse is a simple model with a single monochromatic carrying frequency ω, described by a cosine oscillating function with relative phase ϕ, and a Gaussian envelope of width given by σ and maximum of intensity E_0. The envelop phase is set to zero in the following simulations. The constraining of the cosine function into the Gaussian shape has the effect of losing the perfect monochromaticity of the pulse, resulting in an envelope of effective frequencies experienced by the quantum system.

$$\mathbf{E}(t) = E_0 \exp\left[-\frac{(t-t_0)^2}{2\sigma^2}\right] \cos\left(\omega t + \phi\right) \tag{5.3}$$

Assuming our system to be initially in its ground state, the wavefunction after the interaction with the pulse can be expressed as a coherent superposition of field-free electronic excited states $|\psi_j(\mathbf{r})\rangle$ with amplitude $c_j(t)$:

$$|\Psi(\mathbf{r}, t)\rangle = \sum_j c_j(t)|\psi_j(\mathbf{r})\rangle \tag{5.4}$$

We recall the generic one-particle density expression in eq. (3.4), and by expressing the total wavefunction Ψ and its complex conjugate as the linear combination of the orthonormal basis set ($|\Psi\rangle = \sum_j c_j|\psi_j\rangle$ and $\langle\Psi| = \sum_j c_j^*\langle\psi_j|$) we

can express the density matrix as:

$$\boldsymbol{\rho}(\mathbf{r},t) = \sum_{ij} c_i(t)c_j^*(t)|\psi_i(\mathbf{r})\rangle\langle\psi_j(\mathbf{r})| \tag{5.5}$$

Distinguishing the diagonal and the off-diagonal terms, the time evolution of the one-electron density operator (OEDM) can be expressed in the basis of field-free states as:

$$\rho(\mathbf{r},t) = \sum_j |c_j(t)|^2\rho_{jj}(\mathbf{r}) + \sum_{k\neq j} c_j^*(t)c_k(t)\rho_{jk}(\mathbf{r}) \tag{5.6}$$

where a generic element is the coefficient of the elementary operator $\rho_{ij} = |\psi_i\rangle\langle\psi_j|$. After the interaction of the system with the laser pulse, the squared moduli of the coefficients $c_i(t)$ of the states are stationary, as the dynamics resulting from the evolution of the TDSE are unitary. Indeed, dissipative phenomena are not considered in this simple model, and more complex formalism would be needed to introduce relaxation, dephasing and decoherence processes.[152–155]

The expression in eq. (5.6) is written as a sum of two terms. The first one is the stationary part for each state $|\psi_i\rangle$, containing the ground state $|\psi_0(\mathbf{r})\rangle = \Psi(\mathbf{r},0)$, and by its coefficients describes the *populations* of each state. These are the diagonal element of the density matrix. The off-diagonal elements are present in the second term of the sum, which is a non-stationary term. These are the *coherences* built by the pulse, that after the pulse ($t > t_f$) oscillate in time with frequency given by the the transition frequencies between two states $\exp[-i(E_j - E_k)t/\hbar]$ and ρ_{jk} is the transition density matrix between the states $|\psi_j\rangle$ and $|\psi_k\rangle$.

$$\rho(\mathbf{r},t) = \sum_j |c_j(t_f)|^2\rho_{jj}(\mathbf{r}) + \sum_{k\neq j} c_j^*(t_f)c_k(t_f)\exp\left[-i\frac{(E_k - E_j)t}{\hbar}\right]\rho_{jk}(\mathbf{r}) \tag{5.7}$$

We consider only the diagonal terms, as they describe the stationary preserved transfer of electronic density. Hence we describe the total excited state Ψ_{ES} expressed on the field-free stationary states. This allows us to use a vector $\varphi(t)$ of the coefficients $c_i(t)$, with initial condition $\varphi(0) = (1,0,\ldots,0)$, and propagate

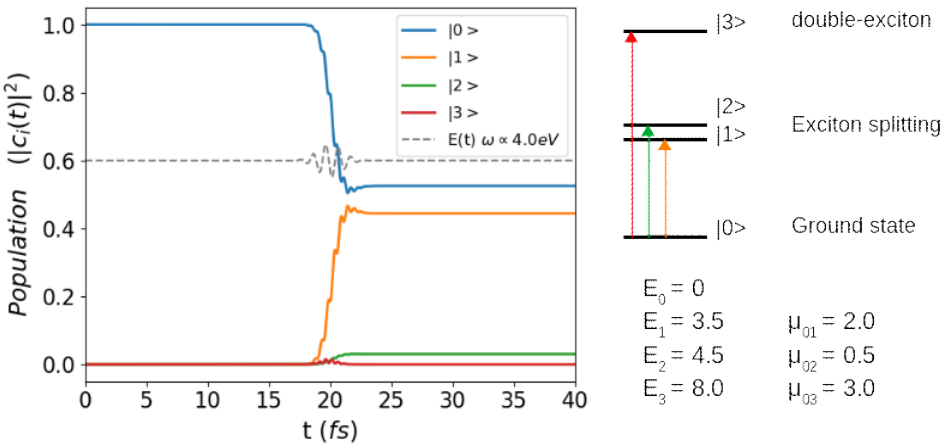

Figure 5.2: Dynamics of the excitation of an ideal excitonic model system driven by a laser pulse centered at 20 fs and with $\sigma = 2.8$ fs. The model system energy states is described on the left, with its transitions dipoles expressed in arbitrary units.

it by the interaction with the laser pulse present in the Hamiltonian of the TDSE, computing a physical meaningful value as the populations $|c_i(t)|^2$ of the states.

The numerical implementation of the solution of the TDSE eq. (5.1) is based on the Runge-Kutta 4^{th} order algorithm.[156]

An ideal excitonic dimer model is considered first, to test the numerical implementation and to show a simple propagation where the evolution of each state can be evaluated, fig. 5.2. We consider two coupled two-level systems, which strongly interact to lead to new states splitted by $2J = 1$ eV, the allowed transitions to the lowest excited state. The high energy excited state corresponding to the excitation of both of the monomer, which is the lowest double-exciton state, is also considered.

Figure 5.2 shows the evolution of the state populations in this simple system upon irradiation with a laser pulse. The resonant field pumps population from the ground state to the first excited state, the second excited state interact poorly with the laser pulse due to the low associated transition dipole, as expected. The higher energy state shows a null population at the end of the pulse even if it slightly oscillates during the application of the pulse. The interaction is not sufficient to move population from the ground to the doubly excited state as the field is completely off-resonance with this transition, as carrying frequency of the pulse is centered at half energy of the transition energy required to reach this state.

5.2 Results

The numerical solusion of the TDSE discussed above is here used to simulate the photo-excitation of the monomer **8D** and its dimer **d.8D**.

The time-independent Hamiltonian H_0 is obtained for each system from the TD-DFT calculation result, on the basis of the excited state. Hence, it is a simple square diagonal matrix whose diagonal elements are the transition energy for each of the N excited states. The ground state is added as a first null element, with relative empty column and row, leading to a square matrix of dimension $(N+1)$.

$$H_0 = \sum_{i}^{N+1} E_i |\psi_i\rangle\langle\psi_i| \tag{5.8}$$

where $|\psi_i\rangle$ are the field-free excited states with i=0 being the ground state. The energies of the states are scaled respect to the GS energy, so as to obtain E_i the transition energies to the i-th state and $E_0 = 0$.

The transition dipoles are obtained by the TD-DFT as well, and the relative matrix $\boldsymbol{\mu}$ is built as a symmetric square matrix, the first row containing the transition dipoles μ_{0i}, the first element μ_{00} set to zero. Another matrix $\tilde{\boldsymbol{\mu}}$ is built to include the dipole coupling between the various excited states. These transient dipoles μ_{ij} are an approximated form, obtained by the manipulation of the MOs dipoles considering the configurations, and relative coefficients, that constitute the excited states. The resulting matrix is then a symmetric square dense matrix with null diagonal elements, that couples the excited states among them.

The first dynamic implemented is for the monomer **8D**. The laser pulse is tailored to excite the second absorption band, that is related to the cluster, using a carrying frequency of energy 5 eV, the width of the Gaussian envelope given by $\sigma = 2.8$ fs. The maximum intensity is set to 0.0015 au (atomic units, used for the implementation to avoid numerical errors) corresponding to $2.63 \cdot 10^{11}$ W/cm^2, in order to significantly populate the excited states. The choice of these values for the pulse have been chosen referring to similar simulation and realistic ultra-fast laser pulses.[23, 157, 158]

In fig. 5.3 the dynamics (a) and (b) are simulated with the same pulse but with the different dipoles matrix $\boldsymbol{\mu}$ and $\tilde{\boldsymbol{\mu}}$. The population of the ground state is consid-

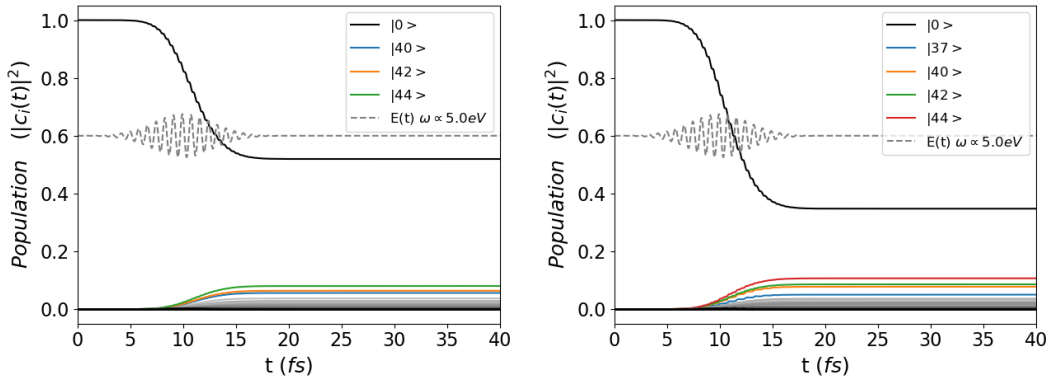

(a) (b)

Figure 5.3: Simulated dynamics for monomer **8D**, with the following parameters: $E_0 = 0.0015$ au, $t_0 = 10$ fs, $\sigma = 2.8$ fs and $\omega \propto 5$ eV. (a) the Hamiltonian considers only transition dipoles from GS to ES using the $\boldsymbol{\mu}$ matrix, while in (b) the transient dipoles are considered by using $\tilde{\boldsymbol{\mu}}$. States populated more than 0.05 are displayed in the legend and the relative curves are colored, while the other states are displayed in grey.

erably diminished by the inter coupling between the excited states ($|c_0(t)|^2 = 0.52$, $|\tilde{c}_0(t)|^2 = 0.35$). State $|37\rangle$ gains oscillator strength by its strong coupling with states $|34\rangle$ and $|36\rangle$ and then its population becomes higher. State $|44\rangle$ too is sensibly more populated, in particular by its coupling with state $|41\rangle$ and $|42\rangle$. In general all the excited states slightly increase their final populations when transitions among excited states are switched on.

The same parameters for the simulations have bee used for the dimer **d.8D**. The excitation profile shows that the packing of the excited states due to the clusters to the first band influences the draining of population of the GS to the various excited states. The final population of the GS at the end of the pulse is eventually very small, $|c_0(t)|^2 = 0.244$, $|\tilde{c}_0(t)|^2 = 0.068$, the GS being almost depopulated when considering transient dipoles coupling.

5.3 Evaluation of Charge Displacement

From the computed profile of excitation, a sum of different excited states is obtained, with population coefficients $|c_i(t)|^2$ which remain stationary after the application of the pulse. We want to evaluate the total charge density difference between the ground state and the system after the interaction with the pulse, that is how the photo-excitation moves the electronic charge within our molecu-

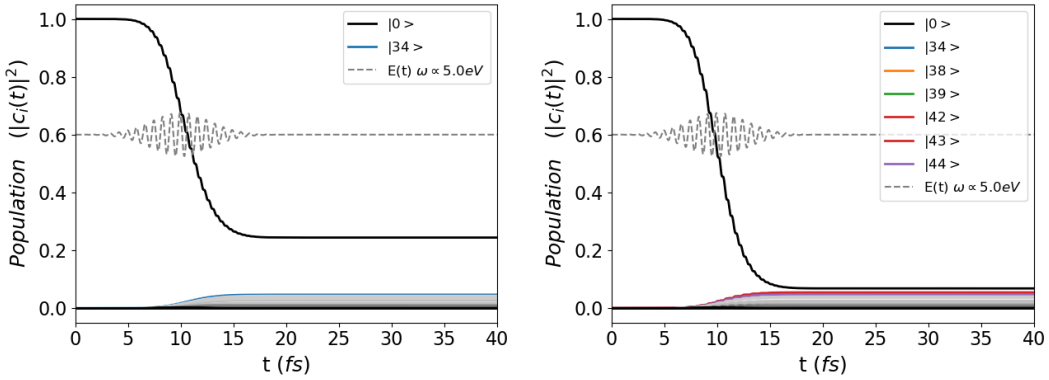

Figure 5.4: Simulated dynamics for dimer **d.8D**, with the following parameters: $E_0 = 0.0015$ au, $t_0 = 10$ fs, $\sigma = 2.8$ fs and $\omega \propto 5$ eV. (a) the Hamiltonian considers only transition dipoles from GS to ES using the $\boldsymbol{\mu}$ matrix, while in (b) the transient dipoles are considered by using $\tilde{\boldsymbol{\mu}}$. States populated more than 0.045 are displayed in the legend and the relative curves are colored, while the other states are displayed in grey.

lar system. To do so we have to evaluate this difference at first for the i-th excited state, so that we can evaluate the static transfer of charge corresponding to the first term in equation (6). We can define the charge density difference (CDD) for each excited state i as :

$$\Delta\rho_i(\mathbf{r}) = \rho_i(\mathbf{r}) - \rho_0(\mathbf{r}) \simeq \rho^{el}(\mathbf{r}) - \rho^{h}(\mathbf{r}) \tag{5.9}$$

where the densities of *electron* and *hole* in the real space are:

$$\rho^{h} = \sum_{i,j\to a} w_i^a w_j^a \varphi_i \varphi_j - \sum_{i,j\leftarrow a} w_i'^a w_j'^a \varphi_i \varphi_j \tag{5.10a}$$

$$\rho^{el} = \sum_{i\to a,b} w_i^a w_i^b \varphi_a \varphi_b - \sum_{i\leftarrow a,b} w_i'^a w_i'^b \varphi_a \varphi_b \tag{5.10b}$$

where w are weight coefficients for the excitations (w) and de-excitations (w') configurations and MOs are denoted by φ. This a first approximation of the effective density difference between an excited state and the ground state, since the excited state density is directly built with the MOs used to describe the GS and excitation coefficients. This density is then referred to as "unrelaxed", as it is not optimised by an interative SCF calculation. However, the qualitative description, and therefore the behaviour of the systems, is maintained.[159] Aknowledged that it is an approximation, it can be used as simplification that enables the calcu-

lation to be computationally feasible for the systems under investigations, that contains thousands of electrons.

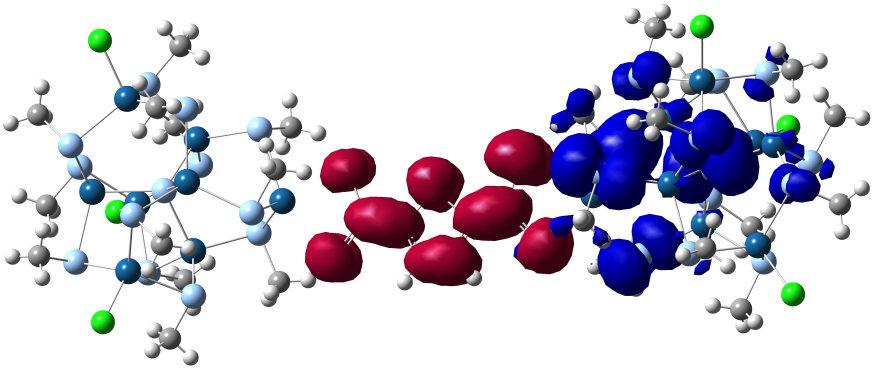

(a)

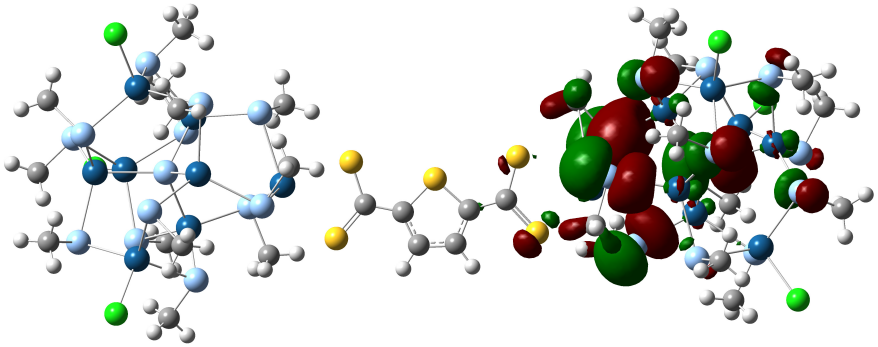

(b)

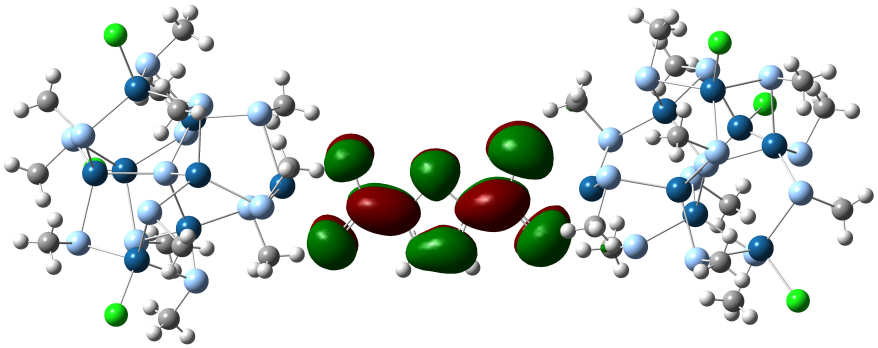

(c)

Figure 5.5: (a) Graphic depiction of the charge density difference evaluated for the 14^{th} excited state of dimer **d.8D** with a grid of 525'888 cubic volumes of 0.35 Å side length, under the unrelaxed excited density approximation. (b) and (c) are the hole and electron states of the first pair of NTOs describing the transition and accounting for most of the transition, with weight $\lambda_1 = 0.98$.

Figure 5.5 is an example of CDD calculated for a single excited state, the 14^{th} excited state of dimer **d.8D**, integrated with a dense grid of small volumes (525888 cubic volumes of 0.35 Å side length). For the relative dynamics result, a looser grid needs to be used (133244 cubic volumes of 0.57 Å side length) to allow the calculation and the following of the 150 excited states densities.

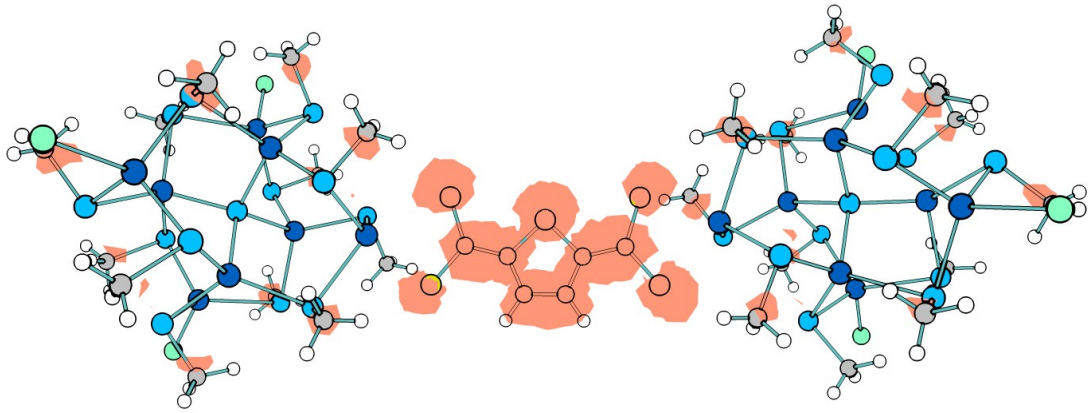

Figure 5.6: Graphic depiction of CDD evaluated for the overall excitation with a Gaussian laser pulse ($E_0 = 0.0015$ au, $t_0 = 10$ fs, $\sigma = 2.8$ fs, $\omega \propto 5$ eV). Only negative charge are dispayed, in orange, to have a better visualisation. The overall electron displacement is towards the bridge DTMT ligand. The image has been created with the ChemCraft software.

For an overall excitation the total charge density difference is calculated as the sum of the CDD weighted for the population coefficients, eq. (5.11), obtained from the dynamics simulation that considers all the dipole couplings, displayed in fig. 5.4b.

$$\Delta\rho^{ES}(\mathbf{r}) = \sum_i |c_i(t_f)|^2 \Delta\rho_i(\mathbf{r}) \tag{5.11}$$

From the CDD graphical visualisation, fig. 5.6, the information about the delocalisation of each state is lost and the results have to be interpreted with the knowledge obtained by the analysis of the static topology gathered.

We observe that, although the single transitions are more localised, there is still an overall displacement of electron density towards the bridging DTMT ligand. This is immediately visible when observing the increase of negative charge on the DTMT ligand, graphically displayed in fig. 5.6.

Conclusions

We had studied the topology of the excitation of a series of sub-nanometric sized CdSe clusters through all-atom TD-DFT electronic structure calculations. The focus of the analysis is the interplay between the inorganic core and organic ligands specifically designed to enhance the delocalisation of the excitation, and between cluster units connected by such ligands.

The results show that the mechanisms underlying the exciton delocalisation among nanostructures are not yet fully understood and that they are more complex than predicted hitherto. We find evidence conflicting with the intuitive idea that molecule with good exciton delocalisation capability should act as an enhancer of the electronic coupling between cluster units. Indeed, in all the clusters linked by DTMT we observe that the exciton localizes back into the inorganic core upon formation of an homodimer.

The study of the ground state and static properties is not sufficient to understand and predict the behaviour of exciton delocalisation over the two units of a dimer. A clear example is given by the study of the frontier orbitals of the clusters belonging to the capped homologous series confronted to the spherical bare $Cd_{13}Se_{13}$ cluster when linked to the DTMT molecule. While the first ones show delocalisation over the special ligand in the HOMO, increasing with the dimension of the cluster, and even in the virtual states for monomer **17D**, they do not show an enhanced coupling in the dimer, rather an unexpected re-localisation of the excitation happens. The **13D** monomer does not show delocalisation in the frontier orbitals, but yet a similar delocalisation in the excitation is appreciated. Nevertheless, the relative dimer **d.13D** shows coupling between inorganic units while at the same time a similar re-localisation to the clusters, arising in a weak coupling that recovers the simple model of coupled Frenkel excitons as in Kasha's

dimers.

Confronted with the previously studied Sulfur-based ligands,[25] the Sulfur within the aromatic backbone seems to have and hindrance effect rather than the expected enhancement of the delocalisation in the dimers.

The DTMT special ligand is more efficient than the most known PDTC in the displacement of charge, and that is evident from the constant presence of CT states spread all over the optical spectrum, but the tendency to a re-localisation plays the opposite role, cancelling out the expected enhancement of the coupling.

The study of a model push-pull dimer open to the research of systems that enhance a directional excitation energy transfer and charge transfer triggered by photo-excitation. The simulated dynamics of the population of the excited states driven by a short laser pulse shows the overall displacement of the electron density. We see that, even if there is more localisation in the dimers, by the sum of the contributions of the single excited eigenstates there still is an increase of electron density over the bridging ligand.

Many other studies are needed to obtain a comprehensive understanding of the role of exciton delocalising ligands and the mechanisms by which they act, both theoretical and experimental. The study of the coherences upon excitation is another missing tile to observe the oscillations of the electron density in the time domain during and after the interaction with an external field, that could help the tuning of the excitation to maximise the delocalisation and the energy transfer. The research for a good exciton delocalising ligand still remains an open and intriguing challenge.

References

(1) Chistyakov, A. A.; Zvaigzne, M. A.; Nikitenko, V. R.; Tameev, A. R.; Martynov, I. L.; Prezhdo, O. V. *Journal of Physical Chemistry Letters* **2017**, *8*, 4129–4139, DOI: 10.1021/acs.jpclett.7b00671.

(2) Choi, M.-J. et al. *Nature Communications* **2020**, *11*, 103.

(3) Muhammad, F.; Tahir, M.; Zeb, M.; Kalasad, M. N.; Mohd Said, S.; Sarker, M. R.; Sabri, M. F. M.; Ali, S. H. M. *Scientific Reports* **2020**, *10*, 4828.

(4) Lan, X.; Chen, M.; Hudson, M. H.; Kamysbayev, V.; Wang, Y.; Guyot-Sionnest, P.; Talapin, D. V. *Nature Materials* **2020**, *19*, 323–329.

(5) Xiang, C.; Wu, L.; Lu, Z.; Li, M.; Wen, Y.; Yang, Y.; Liu, W.; Zhang, T.; Cao, W.; Tsang, S.-W.; Shan, B.; Yan, X.; Qian, L. *Nature Communications* **2020**, *11*, 1646.

(6) Benson, O.; Santori, C.; Pelton, M.; Yamamoto, Y. *Phys. Rev. Lett.* **2000**, *84*, 2513–2516, DOI: 10.1103/PhysRevLett.84.2513.

(7) Muhammad, F.; Tahir, M.; Zeb, M.; Wahab, F.; Kalasad, M. N.; Khan, D. N.; Karimov, K. S. *Sensors and Actuators B: Chemical* **2019**, *285*, 504–512, DOI: https://doi.org/10.1016/j.snb.2019.01.084.

(8) Loss, D.; DiVincenzo, D. P. *Phys. Rev. A* **1998**, *57*, 120–126, DOI: 10.1103/PhysRevA.57.120.

(9) Frees, A.; Mehl, S.; Gamble, J. K.; Friesen, M.; Coppersmith, S. N. *npj Quantum Information* **2019**, *5*, 73.

(10) Bugu, S.; Ozaydin, F.; Ferrus, T.; Kodera, T. *Scientific Reports* **2020**, *10*, 3481.

(11) Fresch, B.; Hiluf, D.; Collini, E.; Levine, R. D.; Remacle, F. Molecular decision trees realized by ultrafast electronic spectroscopy, 2013, DOI: 10.1073/pnas.1314978110.

(12) Yan, T. M.; Fresch, B.; Levine, R. D.; Remacle, F. *Journal of Chemical Physics* **2015**, *143*, DOI: 10.1063/1.4928066.

(13) Donval, A.; Gross, N.; Oron, M. In *Quantum Information Science, Sensing, and Computation X*, ed. by Hayduk, M.; Donkor, E., SPIE: 2018; Vol. 10660, p 4, DOI: 10.1117/12.2299961.

(14) Remacle, F.; Speiser, S.; Levine, R. D. *Journal of Physical Chemistry B* **2001**, *105*, 5589–5591, DOI: 10.1021/jp0101211.

(15) Fresch, B.; Cipolloni, M.; Yan, T. M.; Collini, E.; Levine, R. D.; Remacle, F. *Journal of Physical Chemistry Letters* **2015**, *6*, 1714–1718, DOI: 10.1021/acs.jpclett.5b00514.

(16) Schuld, M.; Sinayskiy, I.; Petruccione, F. *Quantum Information Processing* **2014**, *13*, 2567–2586.

(17) Altaisky, M.; Zolnikova, N.; Kaputkina, N.; Krylov, V.; Lozovik, Y. E.; Dattani, N. *Photonics and Nanostructures - Fundamentals and Applications* **2017**, *24*, 24–28, DOI: https://doi.org/10.1016/j.photonics.2017.02.001.

(18) Altaisky, M. V.; Kaputkina, N. E.; Krylov, V. A. *Physics of Atomic Nuclei* **2018**, *81*, 792–798.

(19) Kilina, S.; Kilin, D.; Tretiak, S. Light-Driven and Phonon-Assisted Dynamics in Organic and Semiconductor Nanostructures, 2015, DOI: 10.1021/acs.chemrev.5b00012.

(20) Nirmal, M.; Dabbousi, B. O.; Bawendi, M. G.; Macklin, J. J.; Trautman, J. K.; Harris, T. D.; Brus, L. E. *Nature* **1996**, *383*, 802–804, DOI: 10.1038/383802a0.

(21) Soloviev, V. N.; Eichhöfer, A.; Fenske, D.; Banin, U. *J. Am. Chem. Soc.* **2001**, *123*, 2354–2364, DOI: 10.1021/ja003598j.

(22) Specht, J. F.; Knorr, A.; Richter, M. *Physical Review B - Condensed Matter and Materials Physics* **2015**, *91*, 155313, DOI: 10.1103/PhysRevB.91.155313.

(23) Collini, E.; Gattuso, H.; Bolzonello, L.; Casotto, A.; Volpato, A.; Dibenedetto, C. N.; Fanizza, E.; Striccoli, M.; Remacle, F. *Journal of Physical Chemistry C* **2019**, *123*, 31286–31293, DOI: 10.1021/acs.jpcc.9b11153.

(24) Zunger, A. *MRS Bulletin* **1998**, *23*, 35–42, DOI: 10.1557/S0883769400031250.

(25) Coden, M.; De Checchi, P.; Fresch, B. *Nanoscale* **2020**, *12*, DOI: 10.1039/d0nr05601d.

(26) Frisch, M. J. et al. Gaussian˜16 Revision C.01, Gaussian Inc. Wallingford CT, 2016.

(27) Plasser, F. TheoDORE: a Toolbox for a Detailed and Automated Analysis of Electronic Excited State Computations, 2019, DOI: 10.26434/chemrxiv.11395314.v1.

(28) Tian Lu, F. C. *J. Comput. Chem.* **2012**, *33*, 580–592, DOI: 10.1002/jcc.22885.

(29) Schmid, G., *Nanoparticles: From Theory to Applications*; Schmid, G., Ed.; Wiley-VCH: 2004.

(30) Brus, L. E. *The Journal of Chemical Physics* **1984**, *80*, 4403–4409, DOI: 10.1063/1.447218.

(31) Alivisatos, A. P.; Harris, A. L.; Levinos, N. J.; Steigerwald, M. L.; Brus, L. E. *The Journal of Chemical Physics* **1988**, *89*, 4001–4011, DOI: 10.1063/1.454833.

(32) Ekimov, A. I.; Kudryavtsev, I. A.; Efros, A. L.; Yazeva, T. V.; Hache, F.; Schanne-Klein, M. C.; Rodina, A. V.; Ricard, D.; Flytzanis, C. *Journal of the Optical Society of America B* **1993**, *10*, 100, DOI: 10.1364/josab.10.000100.

(33) C. R. Kagan C. B. Murray, M. N.; Bawendi, M. G. *Phys. Rev. Lett.* **1996**, *76*, 1517–1520.

(34) Efros, A. L.; Rosen, M.; Kuno, M.; Nirmal, M.; Norris, D.; Bawendi, M. *Physical Review B - Condensed Matter and Materials Physics* **1996**, *54*, 4843–4856, DOI: 10.1103/PhysRevB.54.4843.

(35) Soloviev, V. N.; Eichhöfer, A.; Fenske, D.; Banin, U. *J. Am. Chem. Soc.* **2000**, *122*, 2673–2674, DOI: 10.1021/ja9940367.

(36) Griffin, G. B.; Ithurria, S.; Dolzhnikov, D. S.; Linkin, A.; Talapin, D. V.; Engel, G. S. *Journal of Chemical Physics* **2013**, *138*, 014705, DOI: 10.1063/1.4772465.

(37) Behrens, S.; Fenske, D. *Berichte der Bunsengesellschaft für physikalische Chemie* **1997**, *101*, 1588–1592, DOI: 10.1002/bbpc.19971011106.

(38) Behrens, S.; Bettenhausen, M.; Eichhöfer, A.; Fenske, D. *Angewandte Chemie International Edition in English* **1997**, *36*, 2797–2799, DOI: 10.1002/anie.199727971.

(39) Muhammad, F.; Tahir, M.; Zeb, M.; Wahab, F.; Kalasad, M. N.; Khan, D. N.; Karimov, K. S. *Sensors and Actuators B: Chemical* **2019**, *285*, 504–512, DOI: https://doi.org/10.1016/j.snb.2019.01.084.

(40) Pietryga, J. M.; Park, Y. S.; Lim, J.; Fidler, A. F.; Bae, W. K.; Brovelli, S.; Klimov, V. I. Spectroscopic and device aspects of nanocrystal quantum dots, 2016, DOI: 10.1021/acs.chemrev.6b00169.

(41) Dai, Q.; Song, Y.; Li, D.; Chen, H.; Kan, S.; Zou, B.; Wang, Y.; Deng, Y.; Hou, Y.; Yu, S.; Chen, L.; Liu, B.; Zou, G. *Chemical Physics Letters* **2007**, *439*, 65–68, DOI: 10.1016/j.cplett.2007.03.034.

(42) Kudera, S.; Zanella, M.; Giannini, C.; Rizzo, A.; Li, Y.; Gigli, G.; Cingolani, R.; Ciccarella, G.; Spahl, W.; Parak, W. J.; Manna, L. *Advanced Materials* **2007**, *19*, 548–552, DOI: 10.1002/adma.200601015.

(43) Kilina, S.; Ivanov, S.; Tretiak, S. *J. Am. Chem. Soc.* **2009**, *131*, 7717–7726, DOI: 10.1021/ja9005749.

(44) Nguyen, K. A.; Day, P. N.; Pachter, R. *J. Phys. Chem. C* **2010**, *114*, 16197–16209, DOI: 10.1021/jp103763d.

(45) Azpiroz, J. M.; Matxain, J. M.; Infante, I.; Lopez, X.; Ugalde, J. M. *Phys. Chem. Chem. Phys.* **2013**, *15*, 10996–11005, DOI: 10.1039/C3CP51687C.

(46) Gao, Y.; Zhou, B.; Kang, S.-g.; Xin, M.; Yang, P.; Dai, X.; Wang, Z.; Zhou, R. *RSC Adv.* **2014**, *4*, 27146–27151, DOI: 10.1039/C4RA03202K.

(47) Wang, Y.; Liu, Y. H.; Zhang, Y.; Kowalski, P. J.; Rohrs, H. W.; Buhro, W. E. *Inorganic Chemistry* **2013**, *52*, 2933–2938, DOI: 10.1021/ic302327p.

(48) Kasuya, A. et al. Ultra-stable nanoparticles of CdSe revealed from mass spectrometry, 2004, DOI: 10.1038/nmat1056.

(49) Wang, Y.; Liu, Y.-H.; Zhang, Y.; Wang, F.; Kowalski, P. J.; Rohrs, H. W.; Loomis, R. A.; Gross, M. L.; Buhro, W. E. *Angewandte Chemie International Edition* **2012**, *51*, 6154–6157, DOI: 10.1002/anie.201202380.

(50) Hsieh, T. E.; Yang, T. W.; Hsieh, C. Y.; Huang, S. J.; Yeh, Y. Q.; Chen, C. H.; Li, E. Y.; Liu, Y. H. *Chemistry of Materials* **2018**, *30*, 5468–5477, DOI: 10.1021/acs.chemmater.8b02468.

(51) Xie, Y.; Du, N.; Yu, S.; Zhang, L.; Yang, M. *Journal of Physical Chemistry C* **2019**, *123*, 30714–30722, DOI: 10.1021/acs.jpcc.9b09152.

(52) Green, M. The nature of quantum dot capping ligands, 2010, DOI: 10.1039/c0jm00007h.

(53) Rossi, L. M.; Fiorio, J. L.; Garcia, M. A.; Ferraz, C. P. The role and fate of capping ligands in colloidally prepared metal nanoparticle catalysts, 2018, DOI: 10.1039/c7dt04728b.

(54) Boles, M. A.; Ling, D.; Hyeon, T.; Talapin, D. V. The surface science of nanocrystals, 2016, DOI: 10.1038/nmat4526.

(55) Voorhees, P. W. *Journal of Statistical Physics* **1985**, *38*, 231–252, DOI: 10.1007/BF01017860.

(56) Salvador, M. R.; Hines, M. A.; Scholes, G. D. *Journal of Chemical Physics* **2003**, *118*, 9380–9388, DOI: 10.1063/1.1568733.

(57) Dong, S.; Trivedi, D.; Chakrabortty, S.; Kobayashi, T.; Chan, Y.; Prezhdo, O. V.; Loh, Z. H. *Nano Letters* **2015**, *15*, 6875–6882, DOI: 10.1021/acs.nanolett.5b02786.

(58) Liu, J.; Kilina, S. V.; Tretiak, S.; Prezhdo, O. V. *ACS Nano* **2015**, *9*, 9106–9116, DOI: 10.1021/acsnano.5b03255.

(59) Harris, R. D.; Amin, V. A.; Lau, B.; Weiss, E. A. *ACS Nano* **2016**, *10*, 1395–1403, DOI: 10.1021/acsnano.5b06837.

(60) Harris, R. D.; Bettis Homan, S.; Kodaimati, M.; He, C.; Nepomnyashchii, A. B.; Swenson, N. K.; Lian, S.; Calzada, R.; Weiss, E. A. Electronic Processes within Quantum Dot-Molecule Complexes, 2016, DOI: 10.1021/acs.chemrev.6b00102.

(61) Jethi, L.; Mack, T. G.; Krause, M. M.; Drake, S.; Kambhampati, P. *ChemPhysChem* **2016**, *17*, 665–669, DOI: 10.1002/cphc.201501049.

(62) Houtepen, A. J.; Hens, Z.; Owen, J. S.; Infante, I. *Chemistry of Materials* **2017**, *29*, 752–761, DOI: 10.1021/acs.chemmater.6b04648.

(63) Azpiroz, J. M.; De Angelis, F. *ACS Applied Materials and Interfaces* **2015**, *7*, 19736–19745, DOI: 10.1021/acsami.5b05418.

(64) Amin, V. A.; Aruda, K. O.; Lau, B.; Rasmussen, A. M.; Edme, K.; Weiss, E. A. *Journal of Physical Chemistry C* **2015**, *119*, 19423–19429, DOI: 10.1021/acs.jpcc.5b04306.

(65) Frederick, M. T.; Weiss, E. A. *ACS Nano* **2010**, *4*, 3195–3200, DOI: 10.1021/nn1007435.

(66) Frederick, M. T.; Amin, V. A.; Cass, L. C.; Weiss, E. A. *Nano Letters* **2011**, *11*, 5455–5460, DOI: 10.1021/nl203222m.

(67) Frederick, M. T.; Amin, V. A.; Swenson, N. K.; Ho, A. Y.; Weiss, E. A. *Nano Letters* **2013**, *13*, 287–292, DOI: 10.1021/nl304098e.

(68) Azzaro, M. S.; Babin, M. C.; Stauffer, S. K.; Henkelman, G.; Roberts, S. T. *Journal of Physical Chemistry C* **2016**, *120*, 28224–28234, DOI: 10.1021/acs.jpcc.6b08178.

(69) Lian, S.; Weinberg, D. J.; Harris, R. D.; Kodaimati, M. S.; Weiss, E. A. *ACS Nano* **2016**, *10*, 6372–6382, DOI: 10.1021/acsnano.6b02814.

(70) Virgili, T.; Calzolari, A.; Suárez López, I.; Ruini, A.; Catellani, A.; Vercelli, B.; Tassone, F. *Nano Research* **2018**, *11*, 142–150, DOI: 10.1007/s12274-017-1613-4.

(71) Li, W.; Lu, T. F.; Ren, W.; Deng, L.; Zhang, X.; Wang, L.; Tang, J.; Kuznetsov, A. E. *Journal of Materials Chemistry C* **2018**, *6*, 8751–8761, DOI: 10.1039/c8tc03342k.

(72) Cohen, E.; Gdor, I.; Romero, E.; Yochelis, S.; Van Grondelle, R.; Paltiel, Y. Achieving Exciton Delocalization in Quantum Dot Aggregates Using Organic Linker Molecules, 2017, DOI: 10.1021/acs.jpclett.6b02980.

(73) Munro, A. M.; Chandler, C.; Garling, M.; Chai, D.; Popovich, V.; Lystrom, L.; Kilina, S. *Journal of Physical Chemistry C* **2016**, *120*, 29455–29462, DOI: 10.1021/acs.jpcc.6b08247.

(74) Teunis, M. B.; Nagaraju, M.; Dutta, P.; Pu, J.; Muhoberac, B. B.; Sardar, R.; Agarwal, M. *Nanoscale* **2017**, *9*, 14127–14138, DOI: 10.1039/c7nr04874b.

(75) Kaniyankandy, S.; Verma, S. *Journal of Physical Chemistry Letters* **2017**, *8*, 3228–3233, DOI: 10.1021/acs.jpclett.7b01259.

(76) Aruda, K. O.; Amin, V. A.; Thompson, C. M.; Lau, B.; Nepomnyashchii, A. B.; Weiss, E. A. *Langmuir* **2016**, *32*, 3354–3364, DOI: 10.1021/acs.langmuir.6b00689.

(77) Takahashi, K.; Nihira, T. *Tetrahedron Letters* **1989**, *30*, 5903–5906, DOI: 10.1016/S0040-4039(01)93501-4.

(78) Wu, Y. Y.; Meng, M.; Wang, G. Y.; Feng, P.; Liu, C. Y. *Chemical Communications* **2017**, *53*, 3030–3033, DOI: 10.1039/c7cc00119c.

(79) Turkoglu, G.; Cinar, M. E.; Ozturk, T. Thiophene-Based Organic Semiconductors, 2017, DOI: 10.1007/s41061-017-0174-z.

(80) Perepichka, I. F.; Perepichka, D. F., *Handbook of Thiophene-Based Materials*; Perepichka, I. F., Perepichka, D. F., Eds.; John Wiley & Sons, Ltd: Chichester, UK, 2009, pp 1–865, DOI: 10.1002/9780470745533.

(81) Liu, X.; Liu, X. *RSC Advances* **2019**, *9*, 24733–24741, DOI: 10.1039/c9ra03408k.

(82) Pron, A.; Leclerc, M. Imide/amide based π-conjugated polymers for organic electronics, 2013, DOI: 10.1016/j.progpolymsci.2013.08.007.

(83) Wu, Y.; Jing, Y.; Guo, X.; Zhang, S.; Zhang, M.; Huo, L.; Hou, J. *Polymer Chemistry* **2013**, *4*, 536–541, DOI: 10.1039/c2py20674a.

(84) Ravi, M.; Cohen, S.; Agranat, I.; Radhakrishnan, T. P. *Molecular and Crystal Structures of a Class of Push-Pull Quinonoid Compounds with Potential Nonlinear Optical Applications*; tech. rep. 3; 1996.

(85) Leu, W. C.; Fritz, A. E.; Digianantonio, K. M.; Hartley, C. S. *Journal of Organic Chemistry* **2012**, *77*, 2285–2298, DOI: 10.1021/jo2026004.

(86) Hinchliffe, A.; Mkadmh, A.; Nikolaidi, B.; Soscún, H. J.; Abu-Awwad, F. M. *Central European Journal of Chemistry* **2006**, *4*, 743–759, DOI: 10.2478/s11532-006-0037-x.

(87) Bureš, F. *RSC Adv.* **2014**, *4*, 58826–58851, DOI: 10.1039/C4RA11264D.

(88) La Rocca, G. C. In *Electronic Excitations in Organic Nanostructures*; Thin Films and Nanostructures, Vol. 31; Academic Press: 2003, pp 97–128, DOI: https://doi.org/10.1016/S1079-4050(03)31002-6.

(89) Scholes, G. D.; Rumbles, G. Excitons in nanoscale systems, 2006, DOI: 10.1038/nmat1710.

(90) Shinozuka, Y.; Matsuura, M. *Physical Review B* **1983**, *28*, 4878–4881, DOI: 10.1103/PhysRevB.28.4878.

(91) Dresselhaus, M.; Dresselhaus, G.; Cronin, S.; Gomes Souza Filho, A., *Solid State Properties*; Graduate Texts in Physics; Springer Berlin Heidelberg: Berlin, Heidelberg, 2018, DOI: 10.1007/978-3-662-55922-2.

(92) Davydov, A. S., *Theory of Molecular Excitons*; Springer US: 1971, DOI: 10.1007/978-1-4899-5169-4.

(93) Kasha, M.; Rawls, H. R.; El-Bayoumi, M. A. *Pure and Applied Chemistry* **1965**, *11*, 371–392, DOI: 10.1351/pac196511030371.

(94) Beljonne, D.; Curutchet, C.; Scholes, G. D.; Silbey, R. J. *Journal of Physical Chemistry B* **2009**, *113*, 6583–6599, DOI: 10.1021/jp900708f.

(95) Cassette, E.; Pensack, R. D.; Mahler, B.; Scholes, G. D. *Nature Communications* **2015**, *6*, 1–7, DOI: 10.1038/ncomms7086.

(96) Collini, E. *Advances in Science and Technology* **2014**, *93*, 225–234, DOI: 10.4028/www.scientific.net/ast.93.225.

(97) Moro, G. J.; Dall'Osto, G.; Fresch, B. *Chemical Physics* **2018**, *514*, 141–149, DOI: 10.1016/j.chemphys.2018.03.006.

(98) Caram, J. R.; Zheng, H.; Dahlberg, P. D.; Rolczynski, B. S.; Griffin, G. B.; Fidler, A. F.; Dolzhnikov, D. S.; Talapin, D. V.; Engel, G. S. *Journal of Physical Chemistry Letters* **2014**, *5*, 196–204, DOI: 10.1021/jz402336t.

(99) Fermi, E. *Zeitschrift für Physik* **1926**, *36*, 902–912, DOI: 10.1007/BF01400221.

(100) Hohenberg, P.; Kohn, W. *Phys. Rev.* **1964**, *136*, B864–B871, DOI: 10.1103/PhysRev.136.B864.

(101) Becke, A. D. *Phys. Rev. A* **1988**, *38*, 3098–3100, DOI: 10.1103/PhysRevA.38.3098.

(102) Runge, E.; Gross, E. K. U. *Phys. Rev. Lett.* **1984**, *52*, 997–1000, DOI: 10.1103/PhysRevLett.52.997.

(103) Plasser, F.; Lischka, H. *J. Chem. Theory Comput.* **2012**, *8*, 2777–2789, DOI: 10.1021/ct300307c.

(104) Plasser, F.; Bäppler, S. A.; Wormit, M.; Dreuw, A. *The Journal of Chemical Physics* **2014**, *141*, 024107, DOI: 10.1063/1.4885820.

(105) Roos, B. O. In, Lawley, K. P., Ed.; Advances in Chemical Physics, Vol. 69; Wiley: New York, 1987; Chapter THE COMPLETE ACTIVE SPACE SELF-CONSISTENT FIELD METHOD AND ITS APPLICATIONS IN ELECTRONICSTRUCTURE CALCULATIONS, pp 399–446.

(106) Shepard, R. In, Lawley, K. P., Ed., 1st; Ab Initio Methods in Quantum Chemistry II, Vol. 69; Wiley: New York, 1987, pp 63–200.

(107) Hestand, N. J.; Spano, F. C. *Accounts of Chemical Research* **2017**, *50*, 341–350, DOI: 10.1021/acs.accounts.6b00576.

(108) East, A. L. L.; Lim, E. C. *The Journal of Chemical Physics* **2000**, *113*, 8981–8994, DOI: 10.1063/1.1319345.

(109) Luzanov, A. V.; Prezhdo, O. V. *International Journal of Quantum Chemistry* **2005**, *102*, 582–601, DOI: 10.1002/qua.20438.

(110) Luzanov, A. V.; Zhikol, O. A. *International Journal of Quantum Chemistry* **2010**, *110*, 902–924, DOI: 10.1002/qua.22041.

(111) Martin, R. L. *The Journal of Chemical Physics* **2003**, *118*, 4775–4777, DOI: 10.1063/1.1558471.

(112) Amos, A. T.; Hall, G. G. *Proc. Roy. Soc.* **1961**, *A263,* 483–493.

(113) Luzanov, A. V.; Sukhorukov, A. A.; Umanskii, V. E. *Theoretical and Experimental Chemistry* **1976**, *10*, 354–361, DOI: 10.1007/BF00526670.

(114) Luzanov, A. V.; Zhikol, O. A. *International Journal of Quantum Chemistry* **2010**, *110*, 902–924, DOI: 10.1002/qua.22041.

(115) Plasser, F. *The Journal of Chemical Physics* **2016**, *144*, 194107, DOI: 10.1063/1.4949535.

(116) Becke, A. D. *The Journal of Chemical Physics* **1993**, *98*, 5648–5652, DOI: 10.1063/1.464913.

(117) Albert, V. V.; Ivanov, S. A.; Tretiak, S.; Kilina, S. V. *J. Phys. Chem. C* **2011**, *115*, 15793–15800, DOI: 10.1021/jp202510z.

(118) Hay, P. J.; Wadt, W. R. *The Journal of Chemical Physics* **1985**, *82*, 270–283, DOI: 10.1063/1.448799.

(119) Ditchfield, R.; Hehre, W. J.; Pople, J. A. *The Journal of Chemical Physics* **1971**, *54*, 724–728, DOI: 10.1063/1.1674902.

(120) Hehre, W. J.; Ditchfield, R.; Pople, J. A. *The Journal of Chemical Physics* **1972**, *56*, 2257–2261, DOI: 10.1063/1.1677527.

(121) Krishnan, R.; Binkley, J. S.; Seeger, R.; Pople, J. A. *The Journal of Chemical Physics* **1980**, *72*, 650–654, DOI: 10.1063/1.438955.

(122) Grimme, S.; Antony, J.; Ehrlich, S.; Krieg, H. *The Journal of Chemical Physics* **2010**, *132*, 154104, DOI: 10.1063/1.3382344.

(123) Grimme, S.; Ehrlich, S.; Goerigk, L. *Journal of Computational Chemistry* **2011**, *32*, 1456–1465, DOI: 10.1002/jcc.21759.

(124) Lin, Y.-S.; Li, G.-D.; Mao, S.-P.; Chai, J.-D. *J. Chem. Theory Comput.* **2013**, *9*, 263–272, DOI: 10.1021/ct300715s.

(125) Goerigk, L.; Hansen, A.; Bauer, C.; Ehrlich, S.; Najibi, A.; Grimme, S. *Phys. Chem. Chem. Phys.* **2017**, *19*, 32184–32215, DOI: 10.1039/C7CP04913G.

(126) Berardo, E.; Zwijnenburg, M. A. In, Stefan T. Bromley, M. A. Z., Ed., 1st; Series in Materials Science and Engineering; CRC Press: 6000 Broken Sound Parkway NW, 2016; Chapter Modeling Optical Properties and Excited-State Properties, pp 269–290.

(127) Weigend, F.; Ahlrichs, R. *Philosophical Transactions of the Royal Society A: Mathematical, Physical and Engineering Sciences* **2010**, *368*, 1245–1263, DOI: 10.1098/rsta.2009.0268.

(128) Soloviev, V. N.; Eichhöfer, A.; Fenske, D.; Banin, U. *J. Am. Chem. Soc.* **2000**, *122*, 2673–2674, DOI: 10.1021/ja9940367.

(129) Zwijnenburg, M. A. *Nanoscale* **2011**, *3*, 3780–3787, DOI: 10.1039/C1NR10486A.

(130) Zwijnenburg, M. A. *Nanoscale* **2012**, *4*, 3711–3717, DOI: 10.1039/C2NR30191A.

(131) Zwijnenburg, M. A. *Phys. Chem. Chem. Phys.* **2013**, *15*, 11119–11127, DOI: 10.1039/C3CP50800E.

(132) Yanai, T.; Tew, D. P.; Handy, N. C. *Chemical Physics Letters* **2004**, *393*, 51–57, DOI: https://doi.org/10.1016/j.cplett.2004.06.011.

(133) Berardo, E.; Hu, H.-S.; Shevlin, S. A.; Woodley, S. M.; Kowalski, K.; Zwijnenburg, M. A. *J. Chem. Theory Comput.* **2014**, *10*, 1189–1199, DOI: 10.1021/ct4010273.

(134) Zhao, Y.; Truhlar, D. G. *J. Phys. Chem. A* **2006**, *110*, 13126–13130, DOI: 10.1021/jp066479k.

(135) Yu, H. S.; He, X.; Li, S. L.; Truhlar, D. G. *Chem. Sci.* **2016**, *7*, 5032–5051, DOI: 10.1039/C6SC00705H.

(136) Yu, H. S.; He, X.; Truhlar, D. G. *J. Chem. Theory Comput.* **2016**, *12*, 1280–1293, DOI: 10.1021/acs.jctc.5b01082.

(137) Chai, J.-D.; Head-Gordon, M. *Phys. Chem. Chem. Phys.* **2008**, *10*, 6615–6620, DOI: 10.1039/B810189B.

(138) Peach, M. J. G.; Benfield, P.; Helgaker, T.; Tozer, D. J. *The Journal of Chemical Physics* **2008**, *128*, 044118, DOI: 10.1063/1.2831900.

(139) Rassolov, V. A.; Ratner, M. A.; Pople, J. A.; Redfern, P. C.; Curtiss, L. A. *Journal of Computational Chemistry* **2001**, *22*, 976–984, DOI: 10.1002/jcc.1058.

(140) Check, C. E.; Faust, T. O.; Bailey, J. M.; Wright, B. J.; Gilbert, T. M.; Sunderlin, L. S. *J. Phys. Chem. A* **2001**, *105*, 8111–8116, DOI: 10.1021/jp0119451.

(141) Böhm, M. C. *Berichte der Bunsengesellschaft für physikalische Chemie* **1984**, *88*, 778–778, DOI: 10.1002/bbpc.19840880821.

(142) Pritchard, B. P.; Altarawy, D.; Didier, B.; Gibson, T. D.; Windus, T. L. *J. Chem. Inf. Model.* **2019**, *59*, 4814–4820, DOI: 10.1021/acs.jcim.9b00725.

(143) Barros, C.; de Oliveira, P.; Jorge, F.; Neto, A. C.; Campos, M. *Molecular Physics* **2010**, *108*, 1965–1972, DOI: 10.1080/00268976.2010.499377.

(144) Döllefeld, H.; Weller, H.; Eychmüller, A. *J. Phys. Chem. B* **2002**, *106*, 5604–5608, DOI: 10.1021/jp013234t.

(145) Eichkorn, K.; Ahlrichs, R. *Chemical Physics Letters* **1998**, *288*, 235–242, DOI: 10.1016/S0009-2614(98)00306-6.

(146) Zheng, N.; Bu, X.; Lu, H.; Chen, L.; Feng, P. *Journal of the American Chemical Society* **2005**, *127*, 14990–14991, DOI: 10.1021/ja055376x.

(147) Mulliken, R. S. *The Journal of Chemical Physics* **1955**, *23*, 1833–1840, DOI: 10.1063/1.1740588.

(148) Reed, A. E.; Weinstock, R. B.; Weinhold, F. *The Journal of Chemical Physics* **1985**, *83*, 735–746, DOI: 10.1063/1.449486.

(149) Kilina, S. V.; Tamukong, P. K.; Kilin, D. S. *Accounts of Chemical Research* **2016**, *49*, 2127–2135, DOI: 10.1021/acs.accounts.6b00196.

(150) Fischer, S. A.; Crotty, A. M.; Kilina, S. V.; Ivanov, S. A.; Tretiak, S. *Nanoscale* **2012**, *4*, 904–914, DOI: 10.1039/C2NR11398H.

(151) Madrid-Úsuga, D.; Susa, C. E.; Reina, J. H. *Physical Chemistry Chemical Physics* **2019**, *21*, 12640–12648, DOI: 10.1039/c9cp01398a.

(152) Breuer, H.-P.; Petruccione, F. **2003**, 65–79.

(153) Breuer, H. P.; Petruccione, F., *The Theory of Open Quantum Systems*; Oxford University Press: 2007; Vol. 9780199213900, pp 1–656, DOI: 10.1093/acprof:oso/9780199213900.001.0001.

(154) Yan, Y.; Xu, R. *Annual Review of Physical Chemistry* **2005**, *56*, 187–219, DOI: 10.1146/annurev.physchem.55.091602.094425.

(155) May, V.; Kühn, O. In *Charge and Energy Transfer Dynamics in Molecular Systems*; Wiley-VCH Verlag GmbH & Co. KGaA: 2011, pp 67–190, DOI: 10.1002/9783527633791.ch3.

(156) Press, W. H.; Teukolsky, S. A.; Vetterling, W. T.; Flannery, B. P., *Numerical Recipes The Art Scientific Computing*, 3rd; Press, W. H., Ed.; Cambridge University Press: 2007.

(157) Schwanen, V.; Remacle, F. *Nano Letters* **2017**, *17*, 5672–5681, DOI: 10.1021/acs.nanolett.7b02568.

(158) Dall'Osto, G.; Coccia, E.; Guido, C. A.; Corni, S. *Physical Chemistry Chemical Physics* **2020**, *22*, 16734–16746, DOI: 10.1039/d0cp02557g.

(159) Wiberg, K. B.; Hadad, C. M.; LePage, T. J.; Breneman, C. M.; Frisch, M. J. *The Journal of Physical Chemistry* **1992**, *96*, 671–679, DOI: 10.1021/j100181a030.

Appendix A

Appendix A

A.1 Monomers Optical Spectra

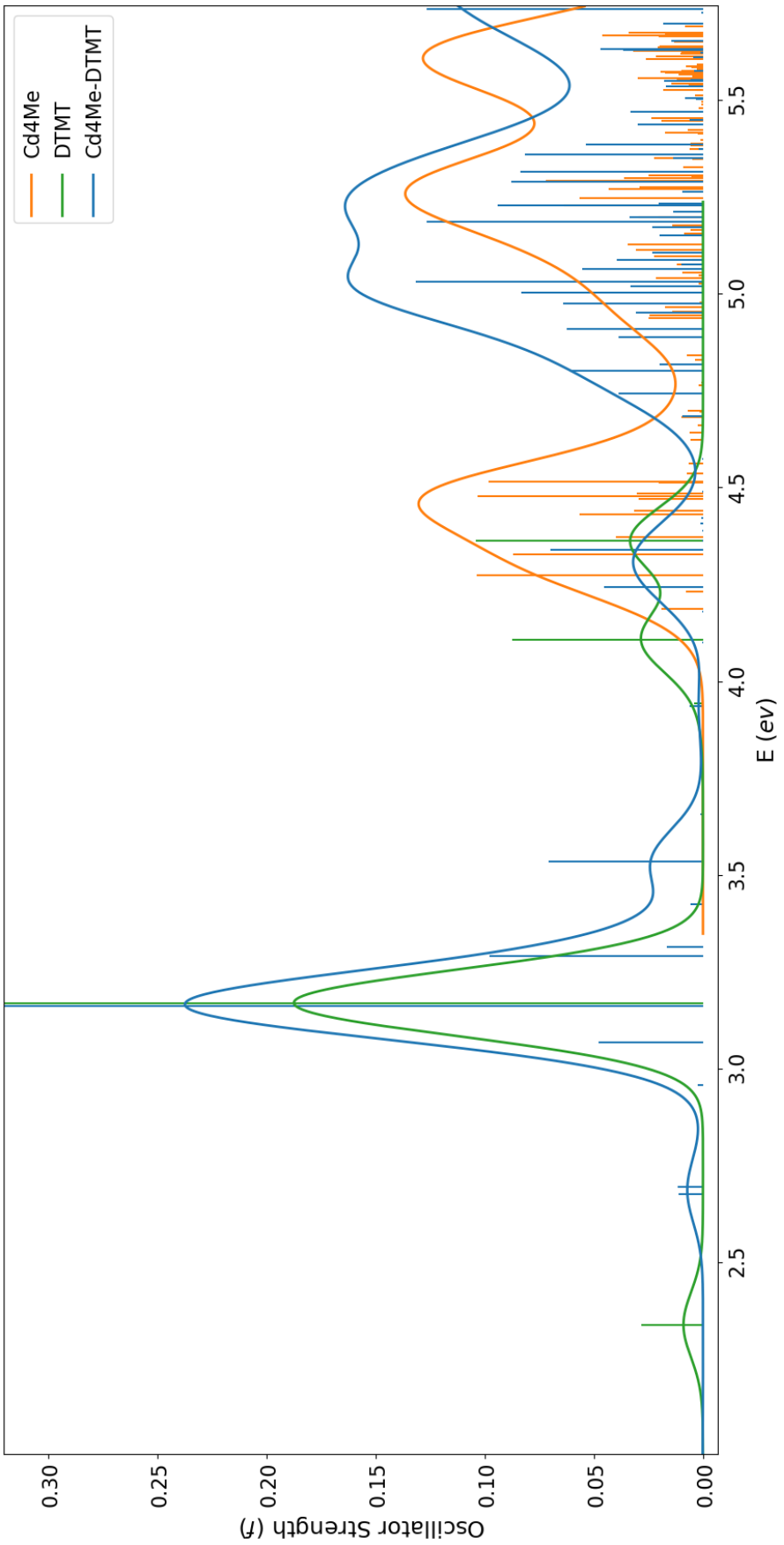

Figure A.1: Simulated optical spectrum of **4D** monomer in blue, the isolated cluster and ligand units respectively in orange and green lines.

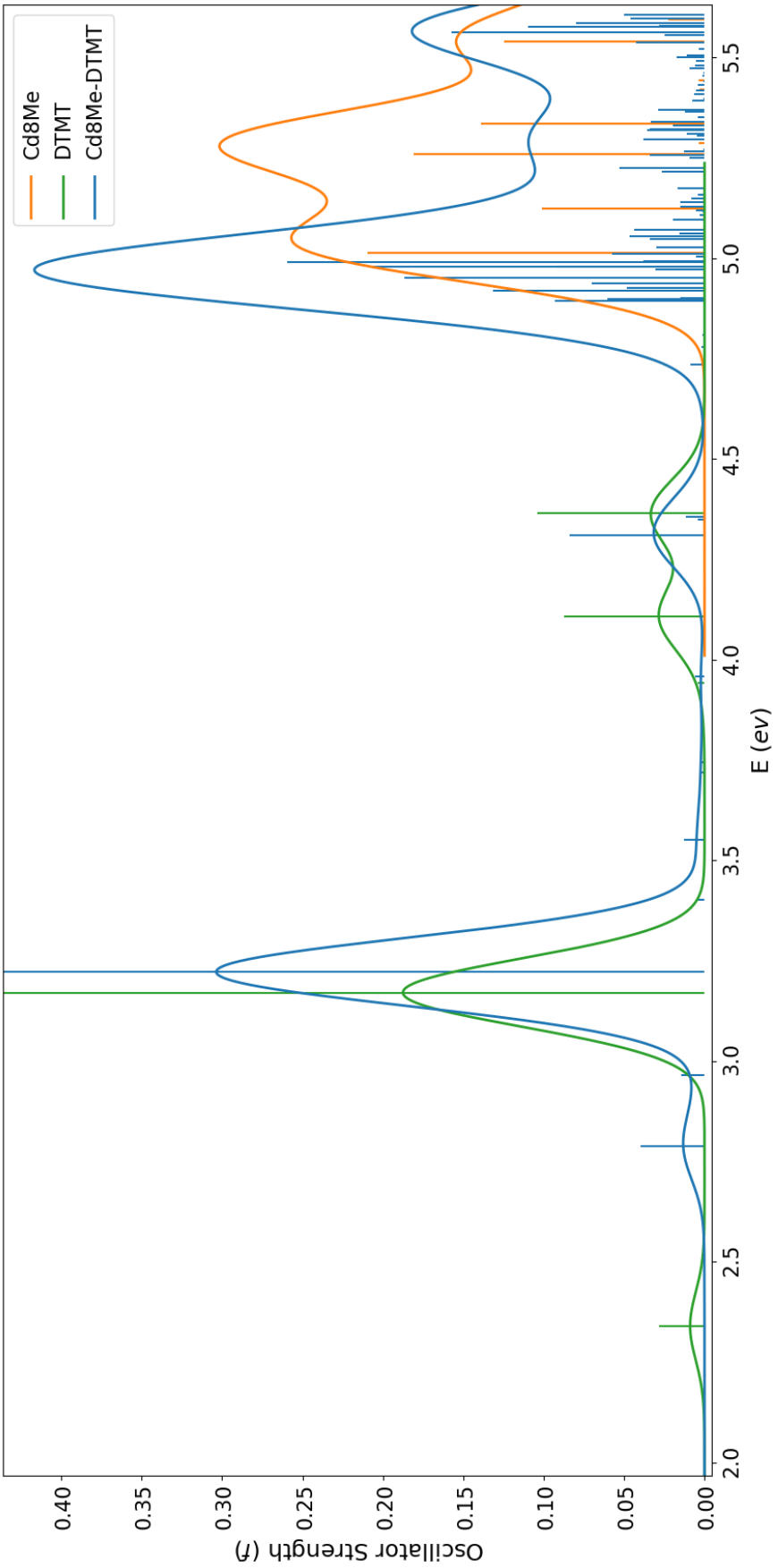

Figure A.2: Simulated optical spectrum of **8D** monomer in blue, the isolated cluster and ligand units respectively in orange and green lines.

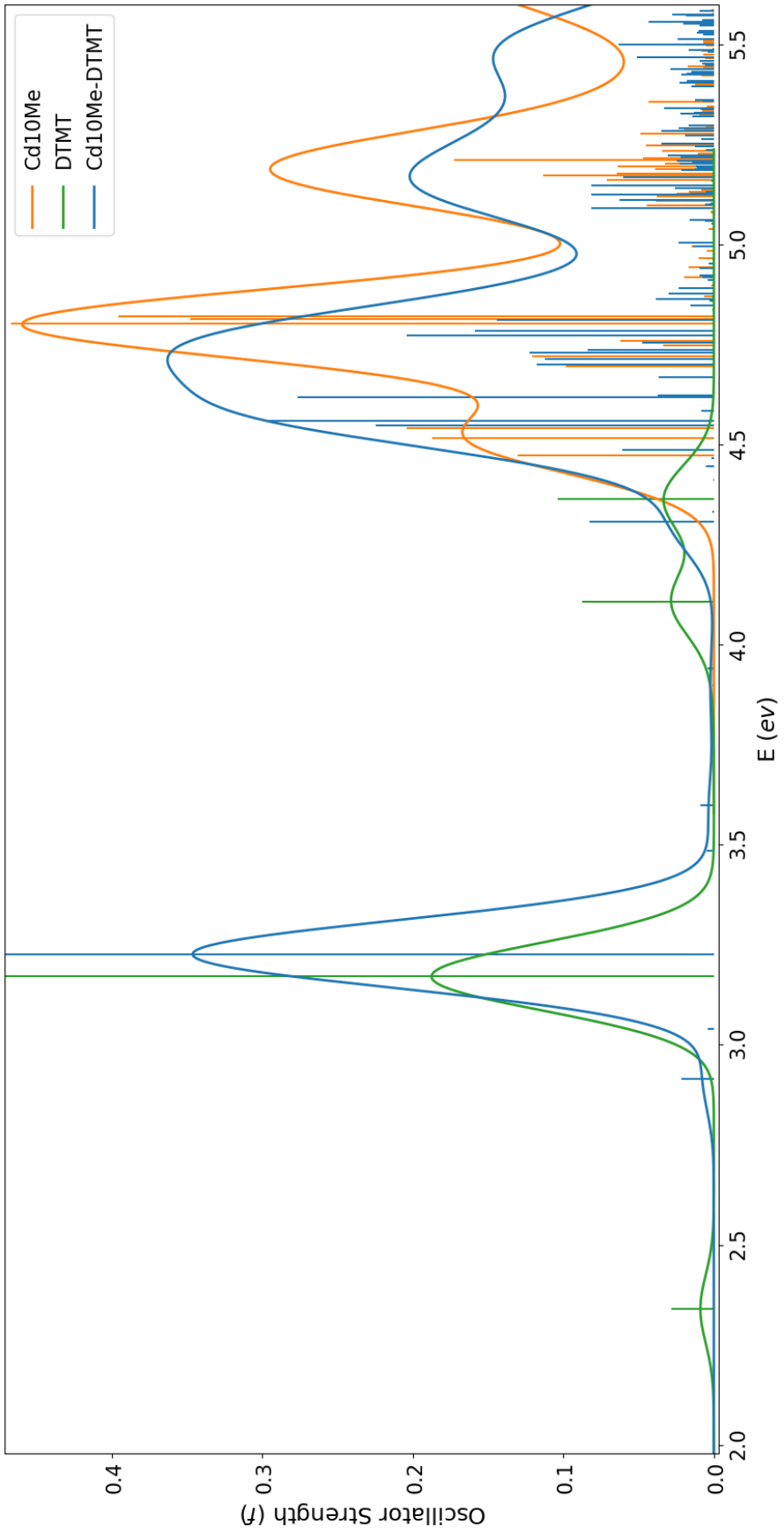

Figure A.3: Simulated optical spectrum of **10D** monomer in blue, the isolated cluster and ligand units respectively in orange and green lines.

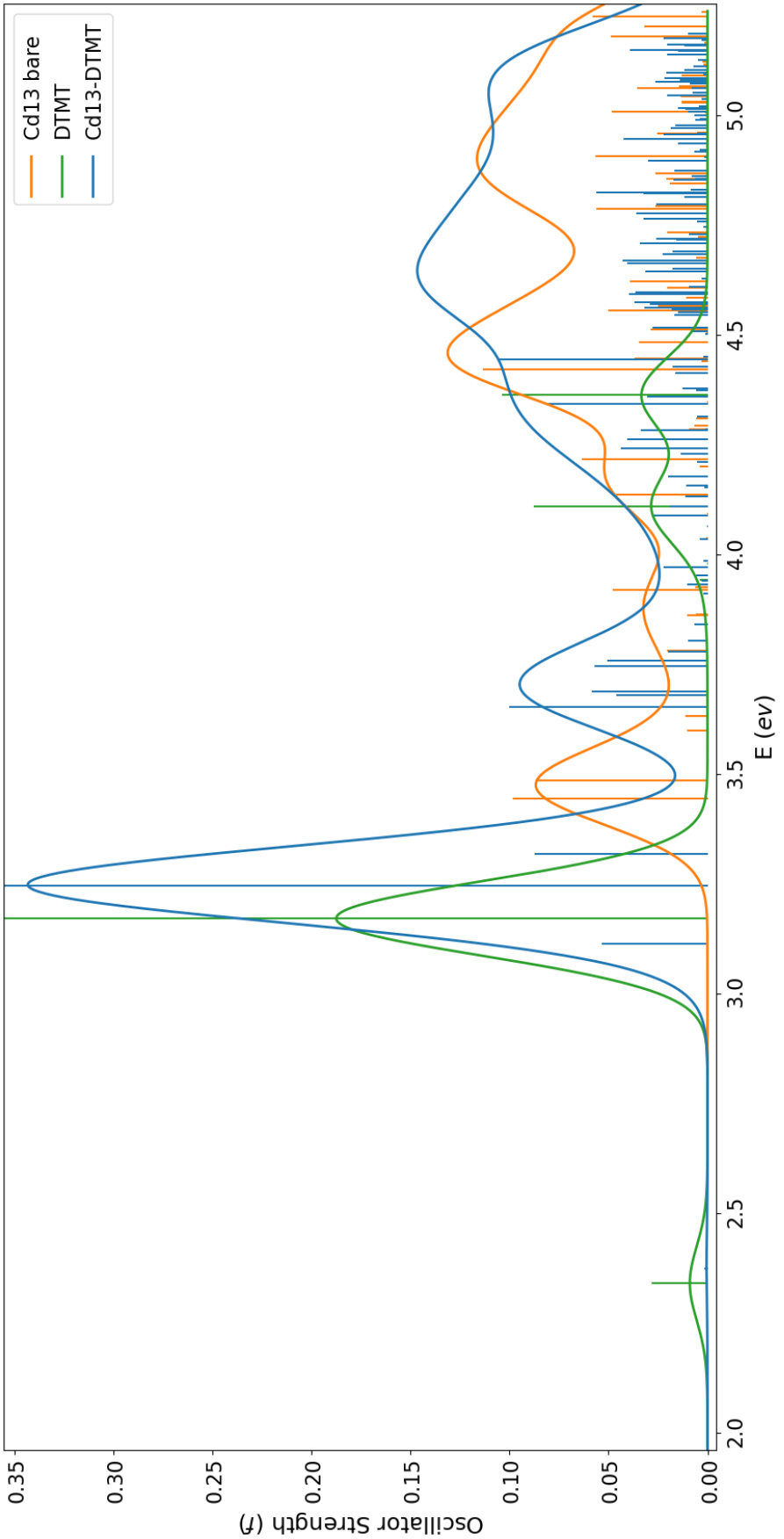

Figure A.4: Simulated optical spectrum of **13D** monomer in blue, the isolated cluster and ligand units respectively in orange and green lines.

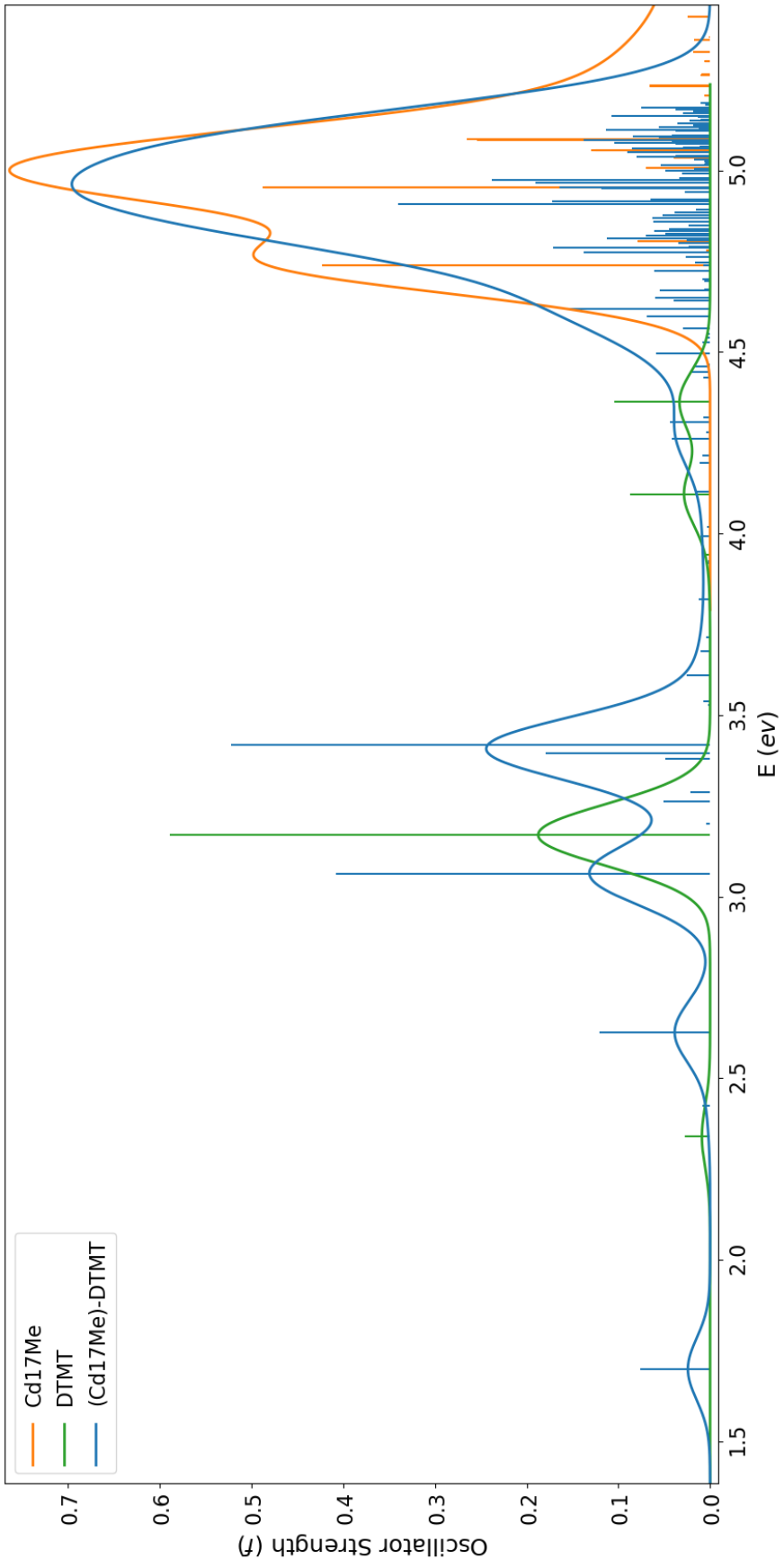

Figure A.5: Simulated optical spectrum of **17D** monomer in blue, the isolated cluster and ligand units respectively in orange and green lines.

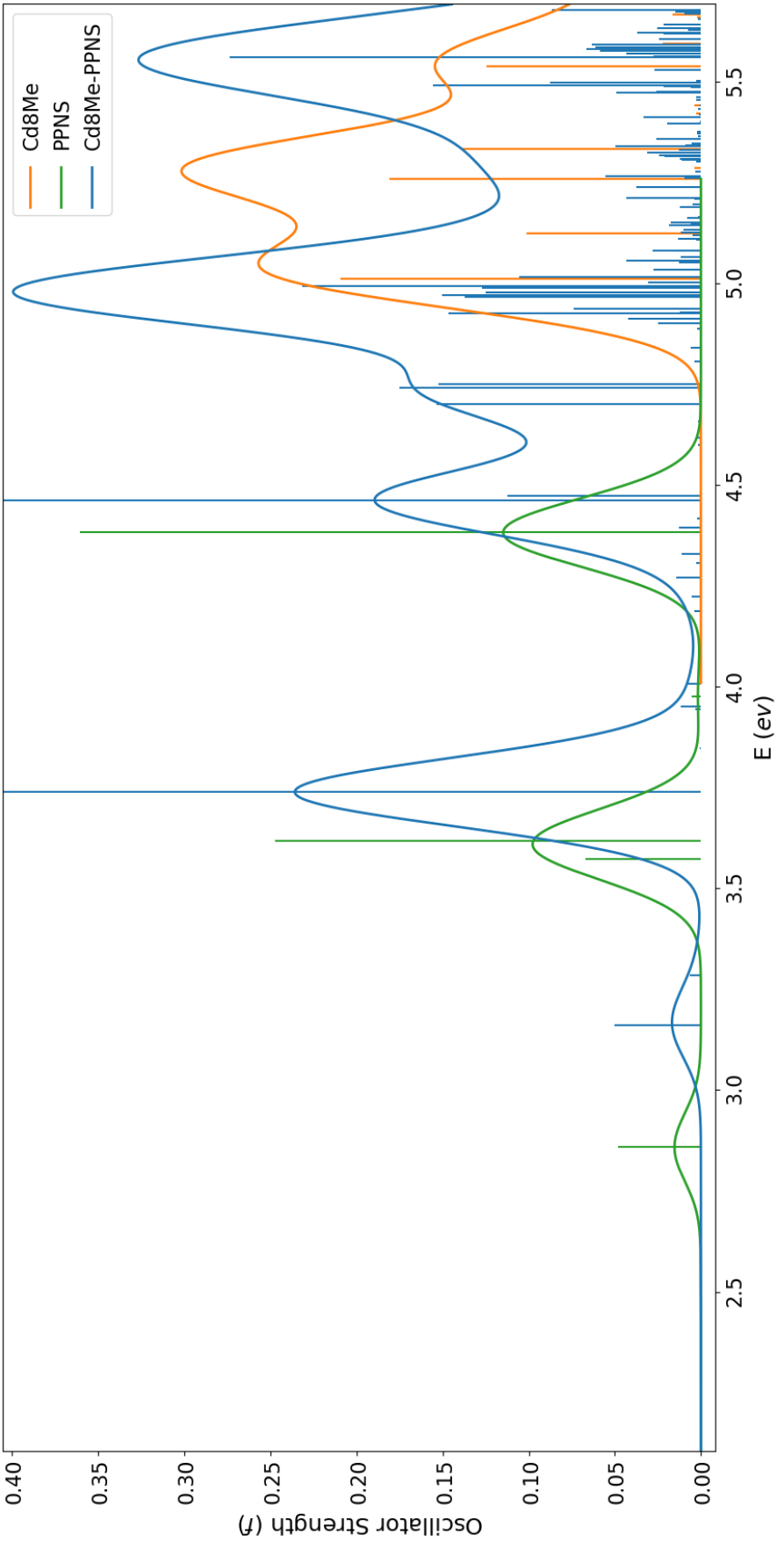

Figure A.6: Simulated optical spectrum of **8P** monomer in blue, the isolated cluster and ligand units respectively in orange and green lines.

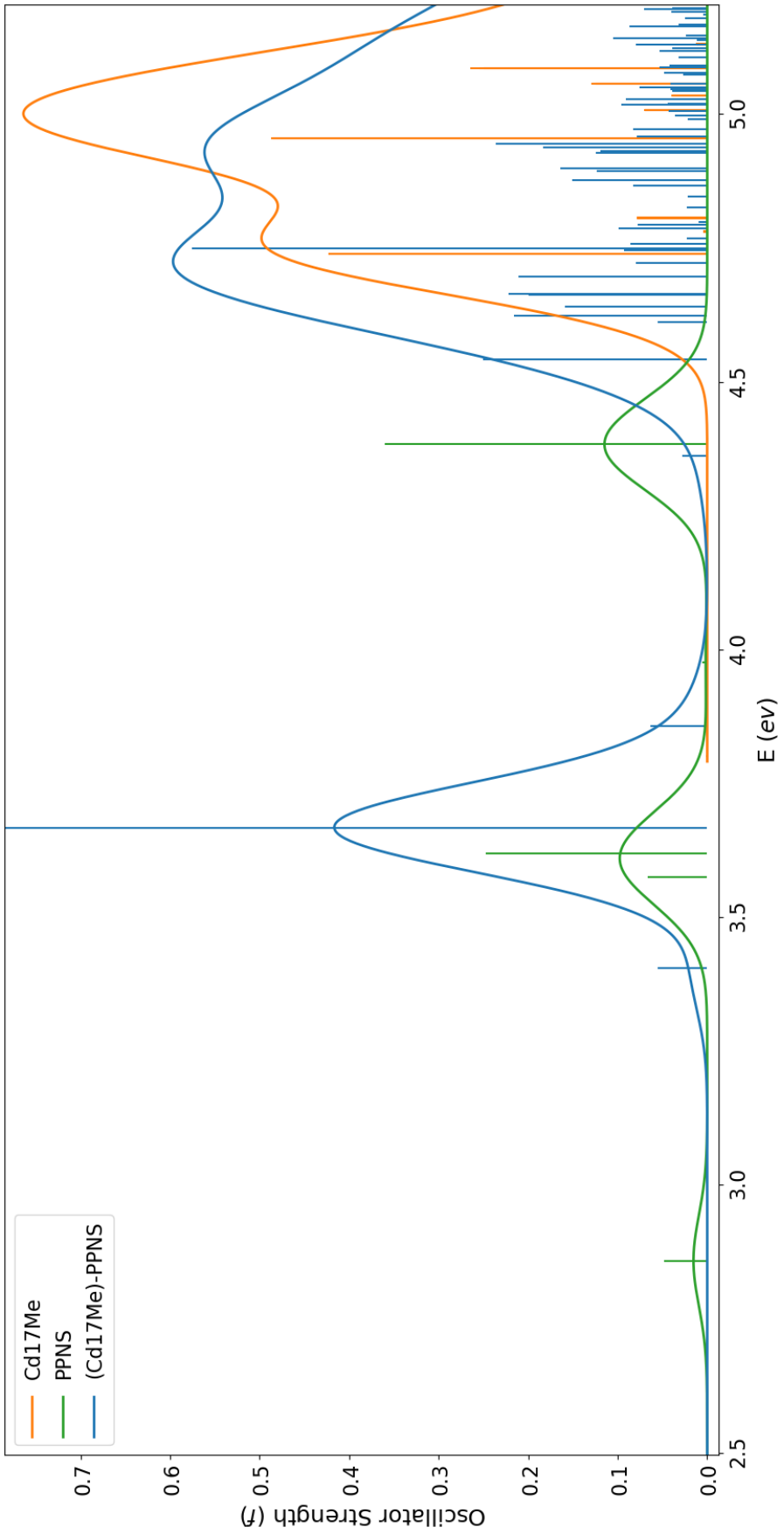

Figure A.7: Simulated optical spectrum of **17P** monomer in blue, the isolated cluster and ligand units respectively in orange and green lines.

A.2 Dimers Optical Spectra

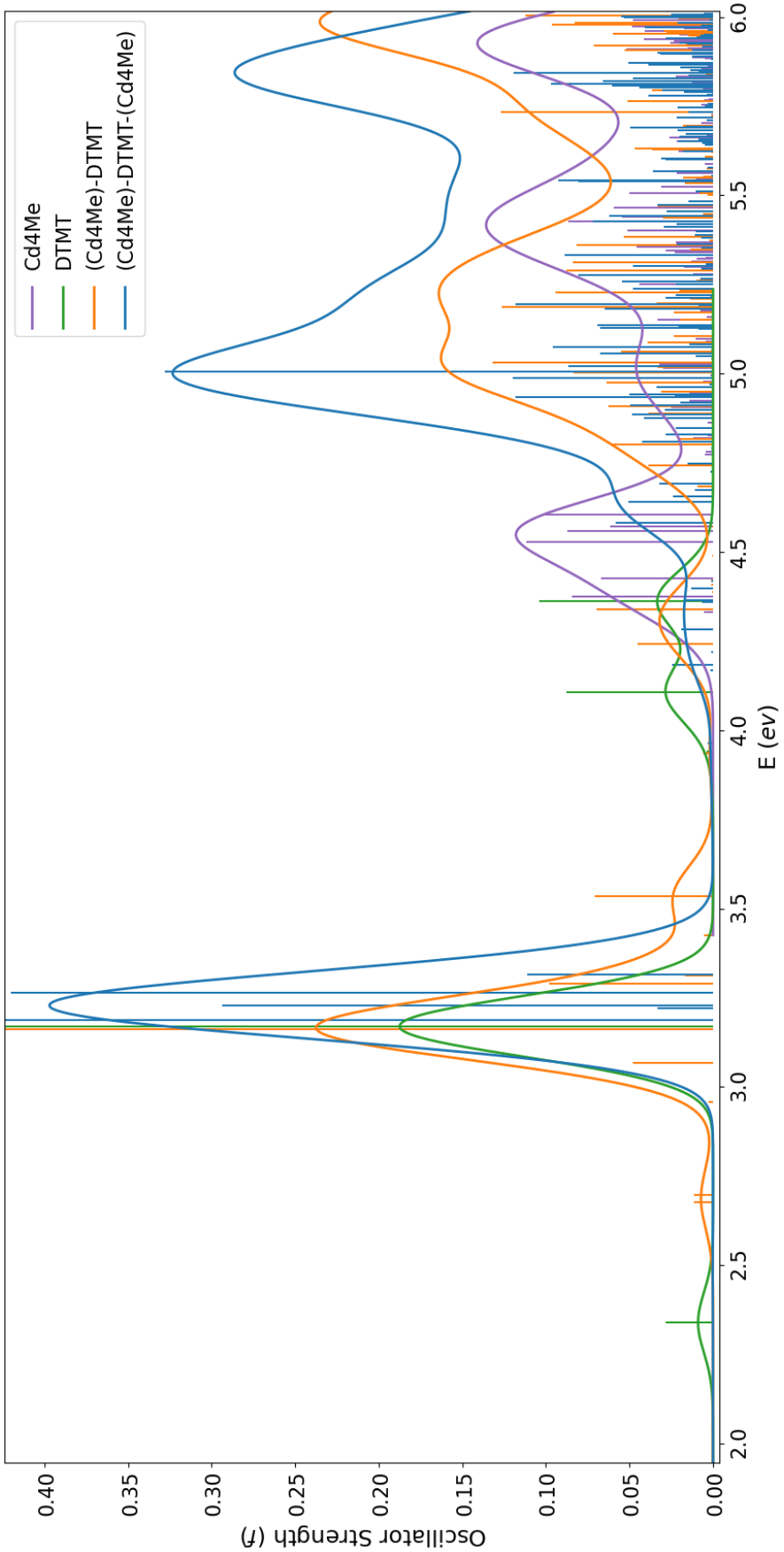

Figure A.8: Simulated optical spectrum of **d.4D** dimer in blue, its monomer spectrum in orange, the isolated cluster and ligand units respectively in purple and green lines.

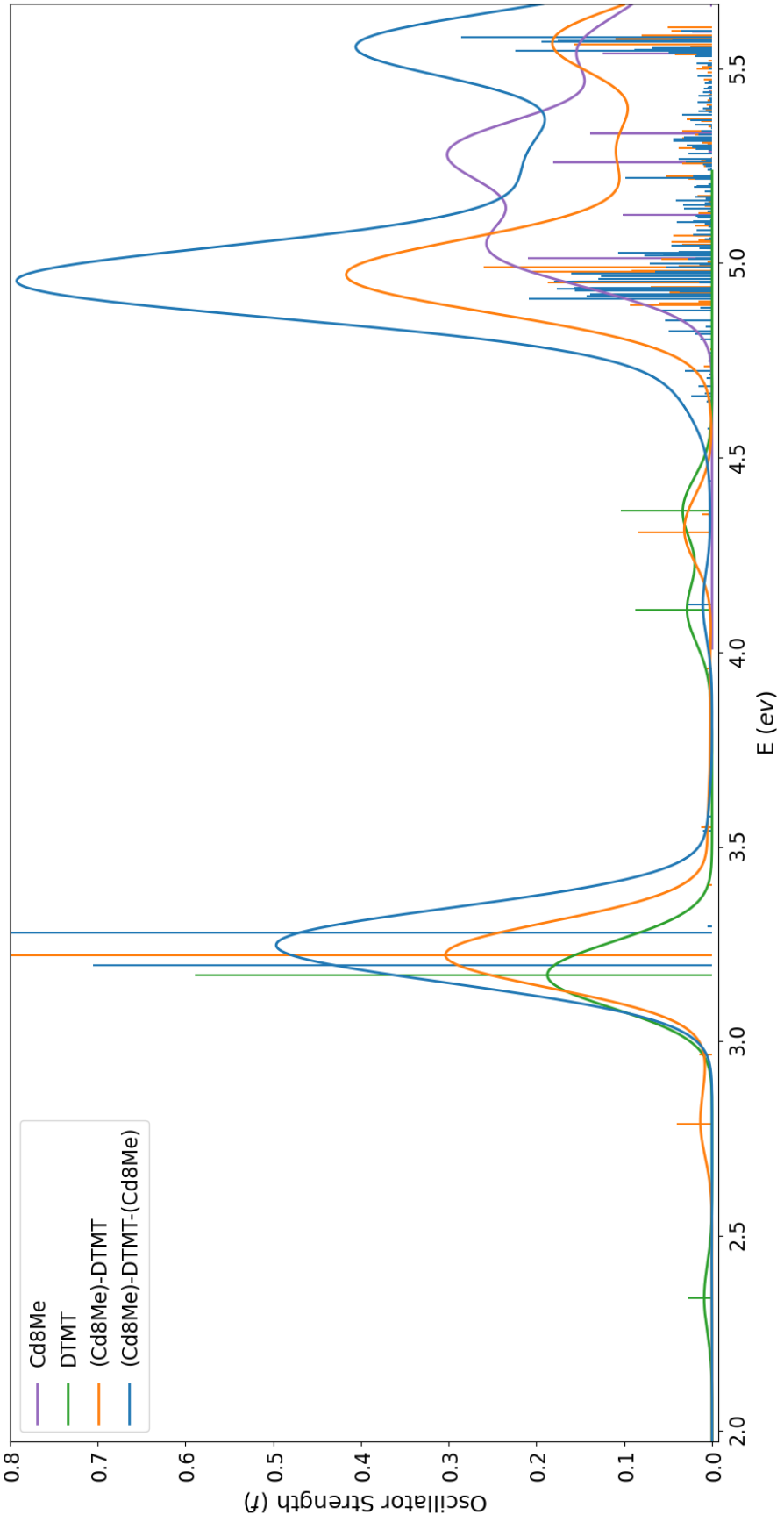

Figure A.9: Simulated optical spectrum of **d.8D** dimer in blue, its monomer spectrum in orange, the isolated cluster and ligand units respectively in purple and green lines.

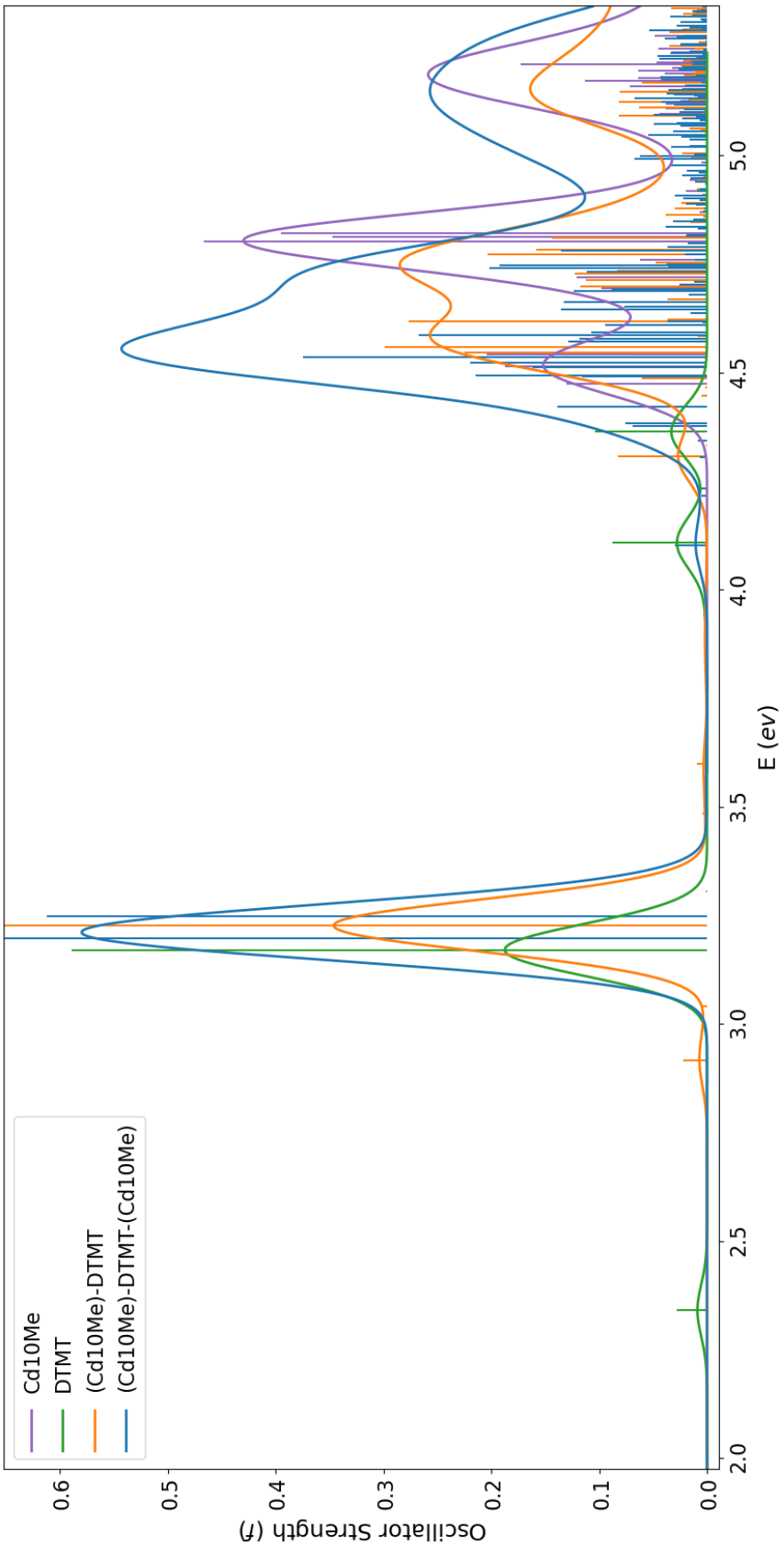

Figure A.10: Simulated optical spectrum of **d.10D** dimer in blue, its monomer spectrum in orange, the isolated cluster and ligand units respectively in purple and green lines.

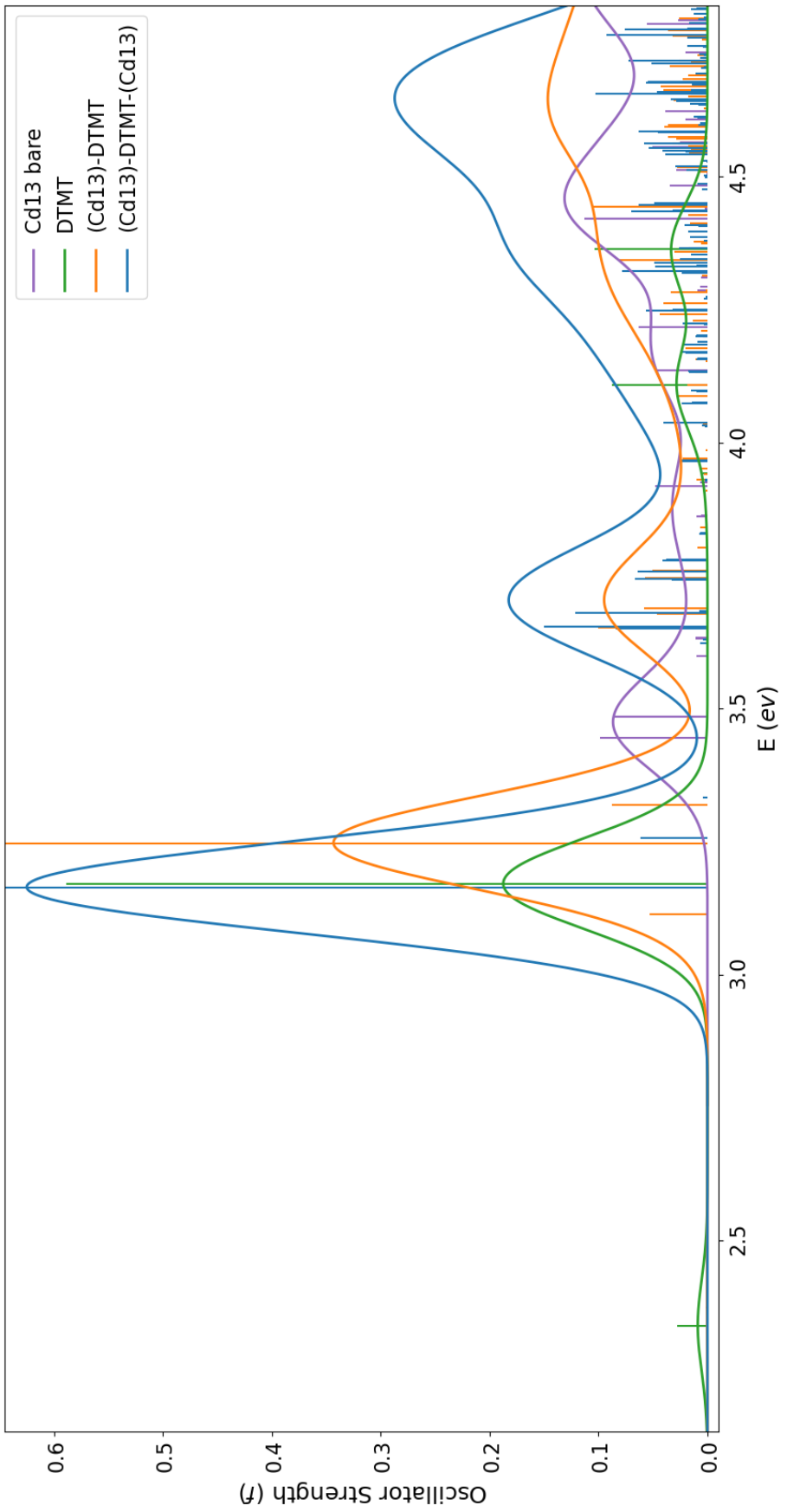

Figure A.11: Simulated optical spectrum of **d.13D** dimer in blue, its monomer spectrum in orange, the isolated cluster and ligand units respectively in purple and green lines.

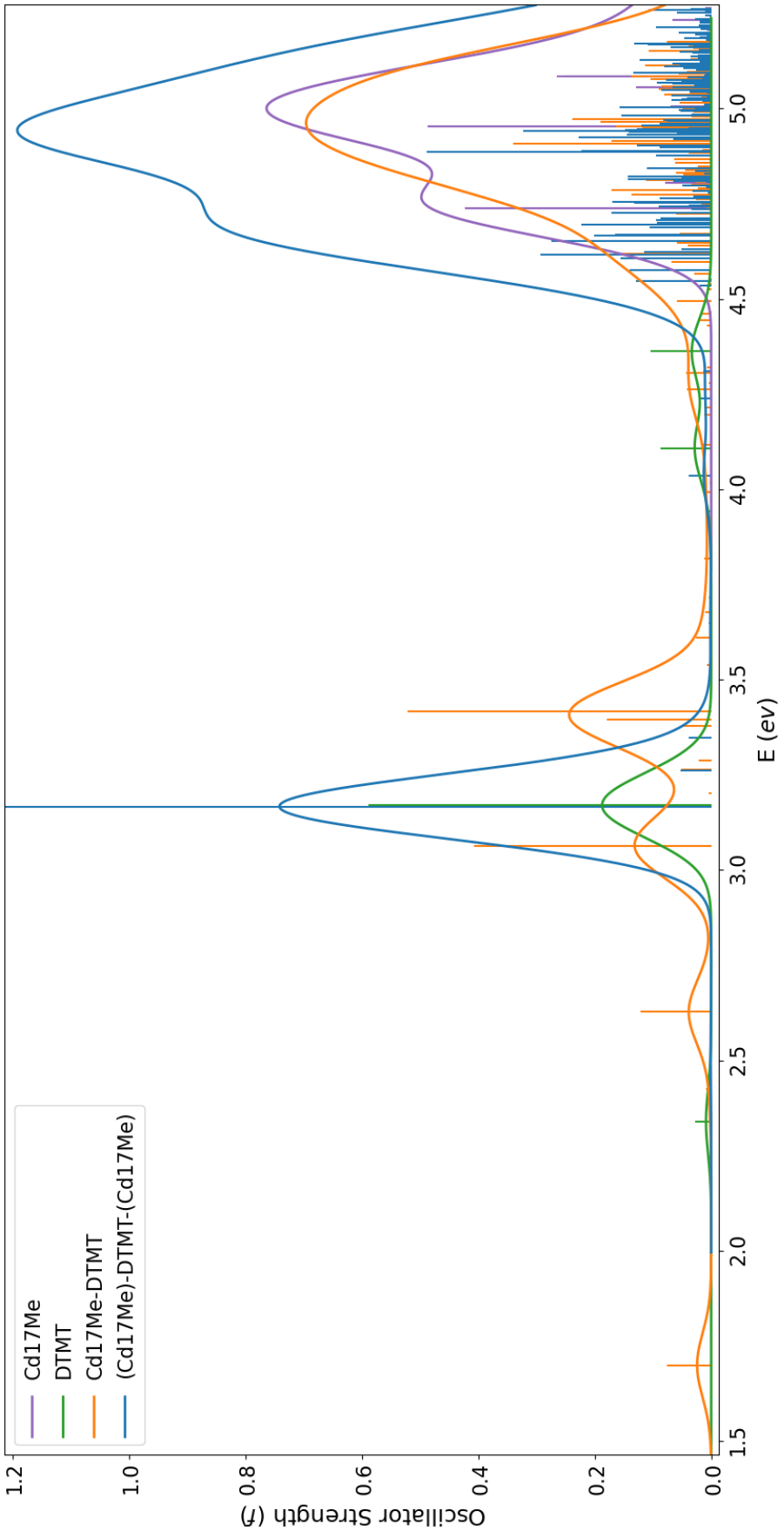

Figure A.12: Simulated optical spectrum of **d.17D** dimer in blue, its monomer spectrum in orange, the isolated cluster and ligand units respectively in purple and green lines.

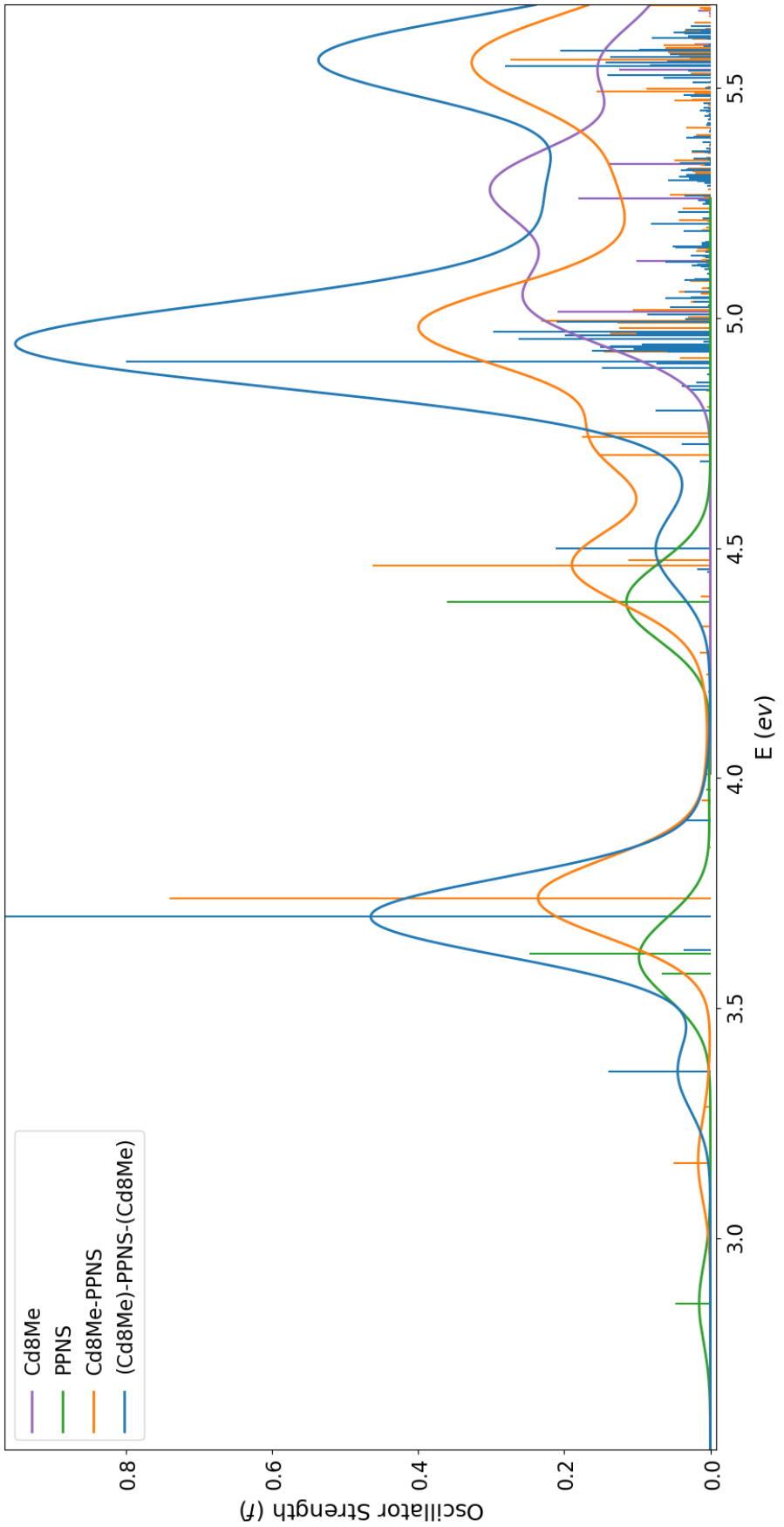

Figure A.13: Simulated optical spectrum of **d.8P** dimer in blue, its monomer spectrum in orange, the isolated cluster and ligand units respectively in purple and green lines.

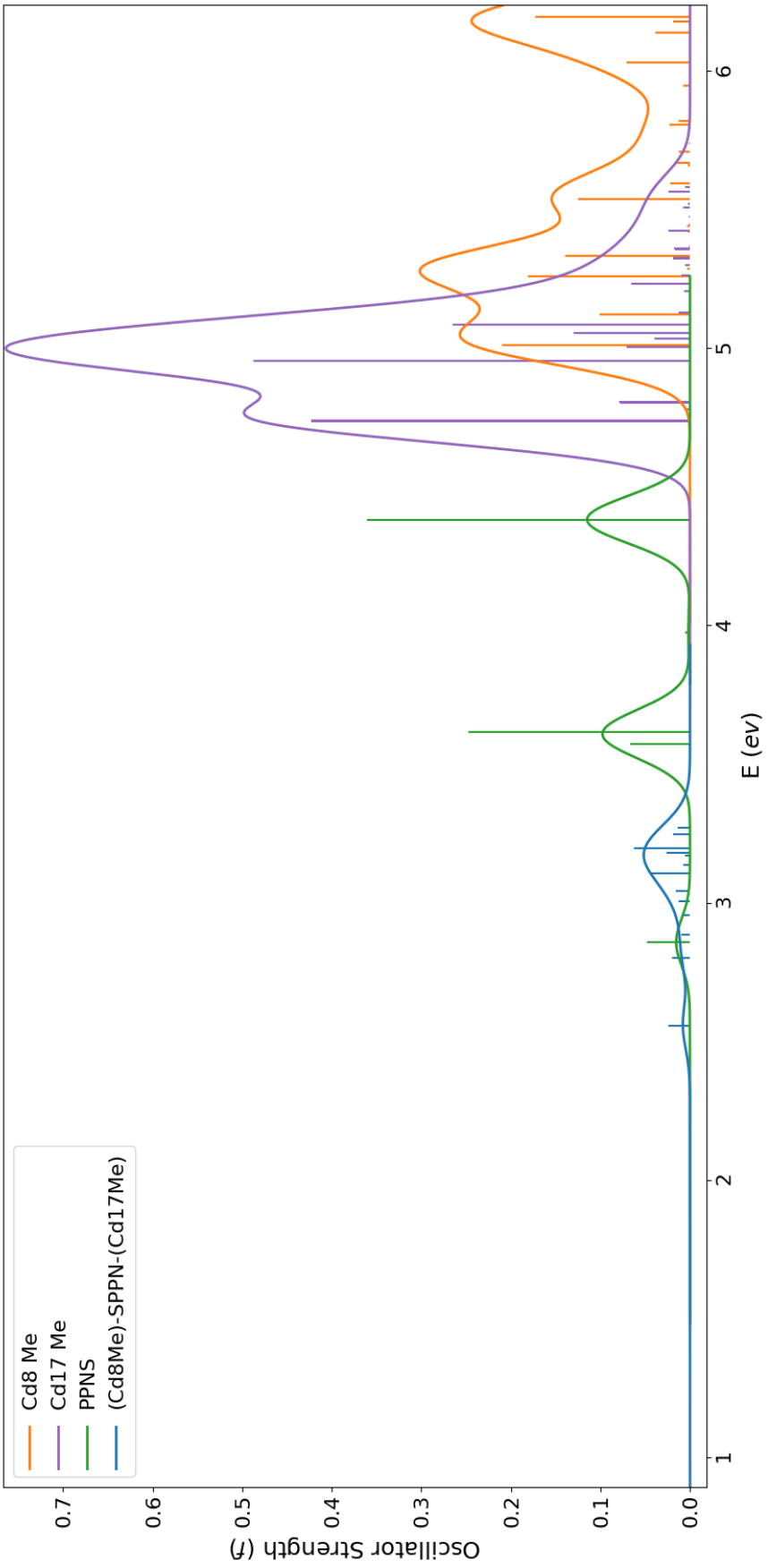

Figure A.14: Simulated optical spectrum of **d.H** dimer in blue, the isolated clusters respectively in orange (**Cd8**) and purple (**Cd17**), and ligand and green lines.

A.3 Monomers Descriptors Spectra

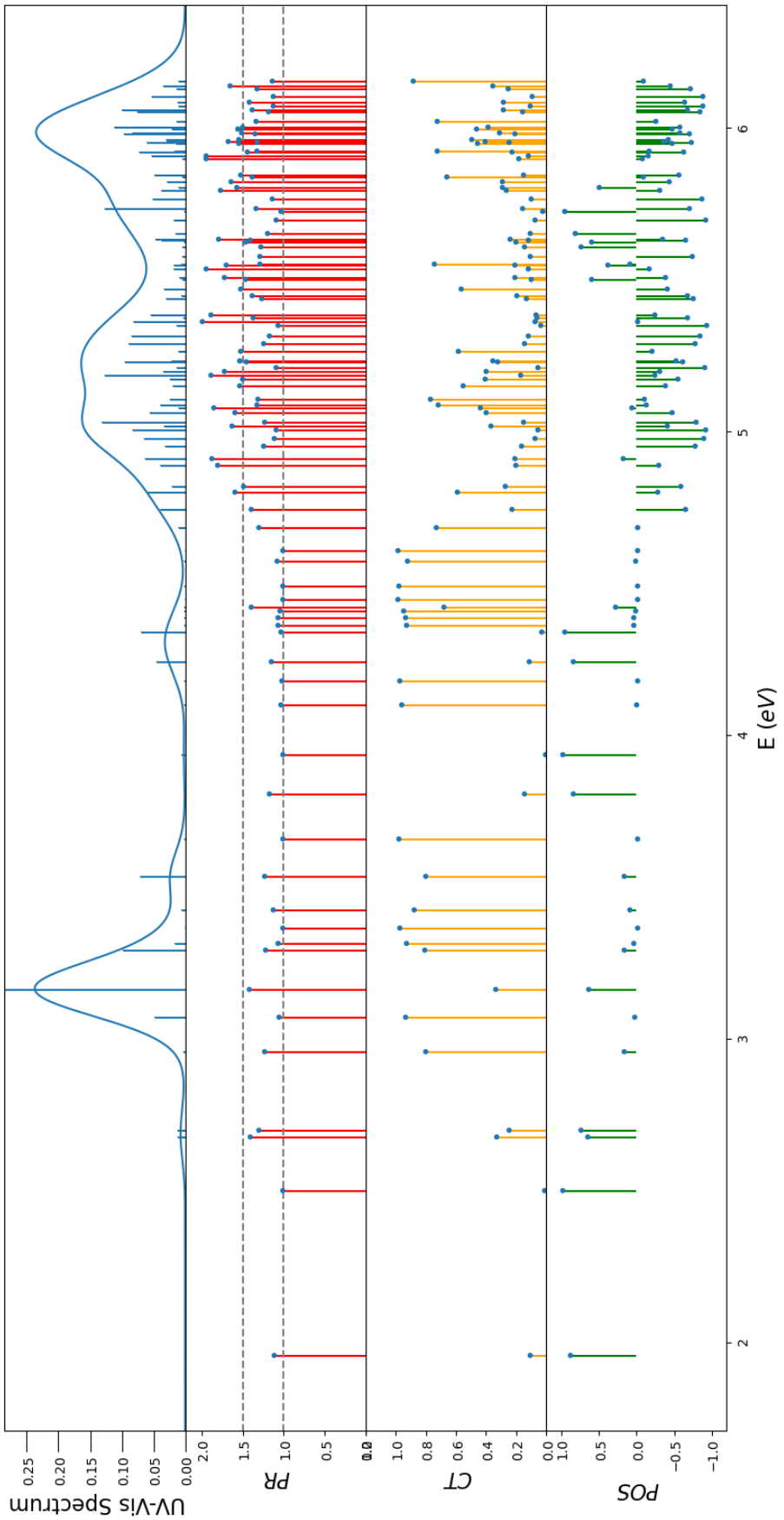

Figure A.15: **4D**

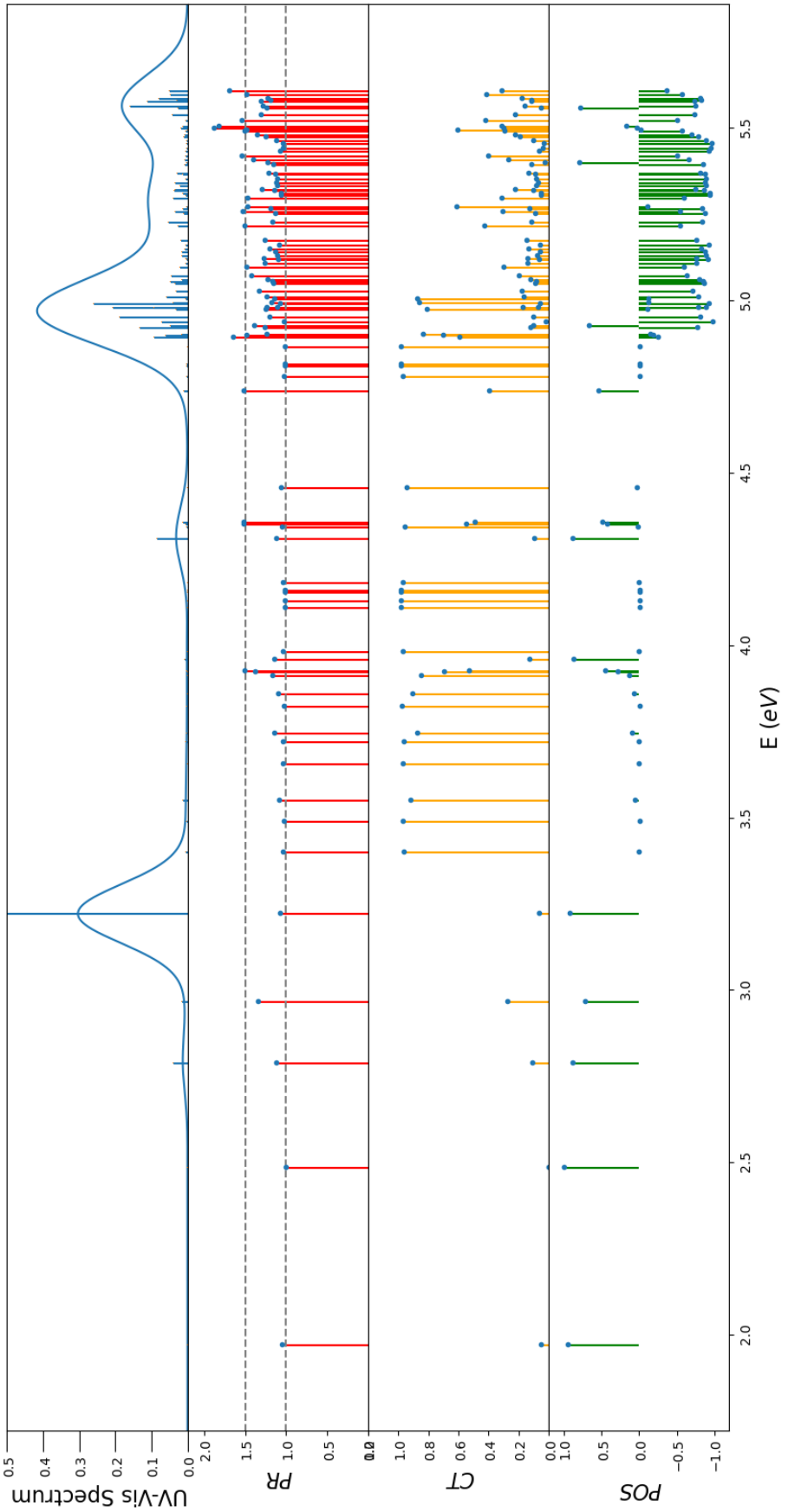

Figure A.16: **8D**

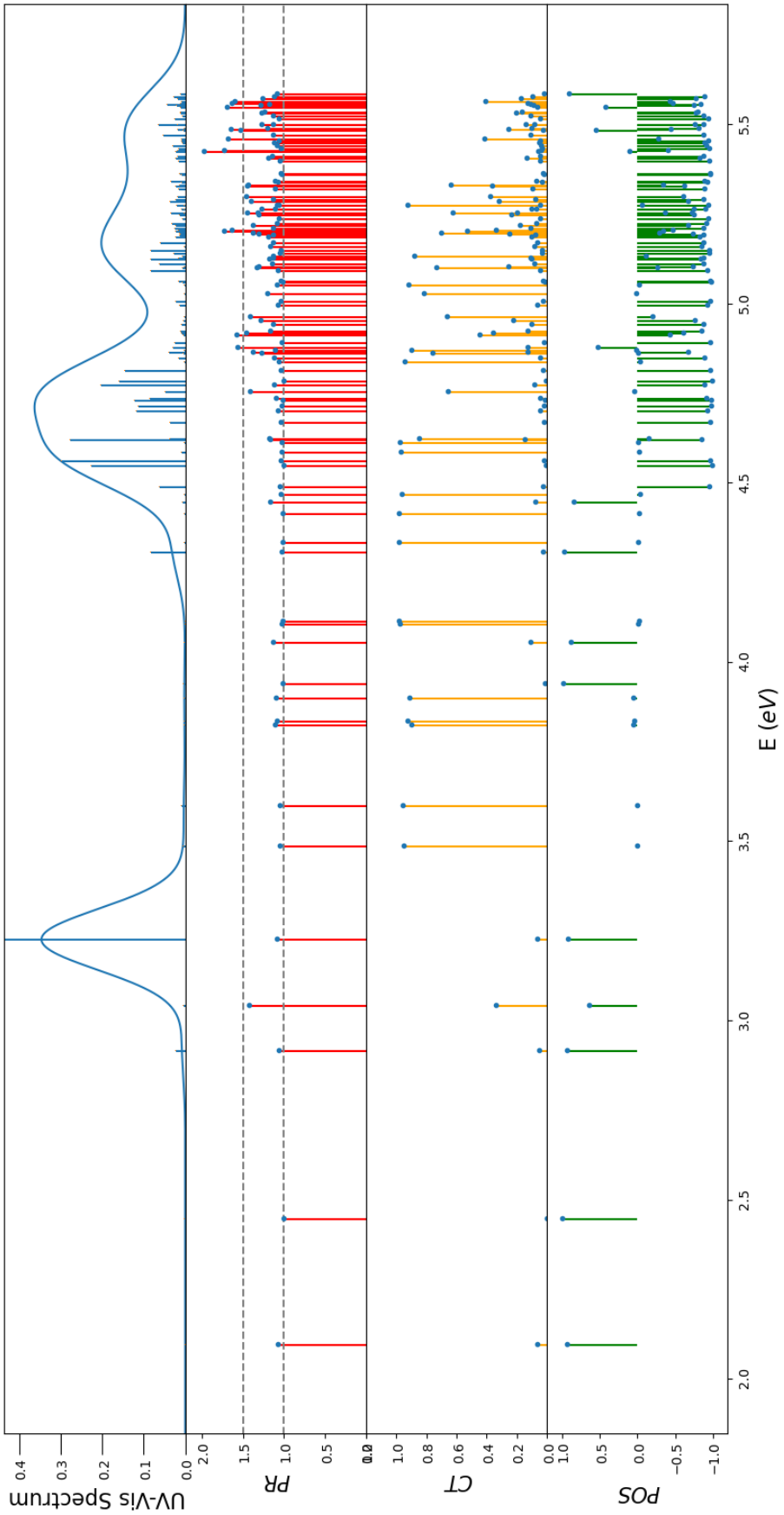

Figure A.17: **10D**

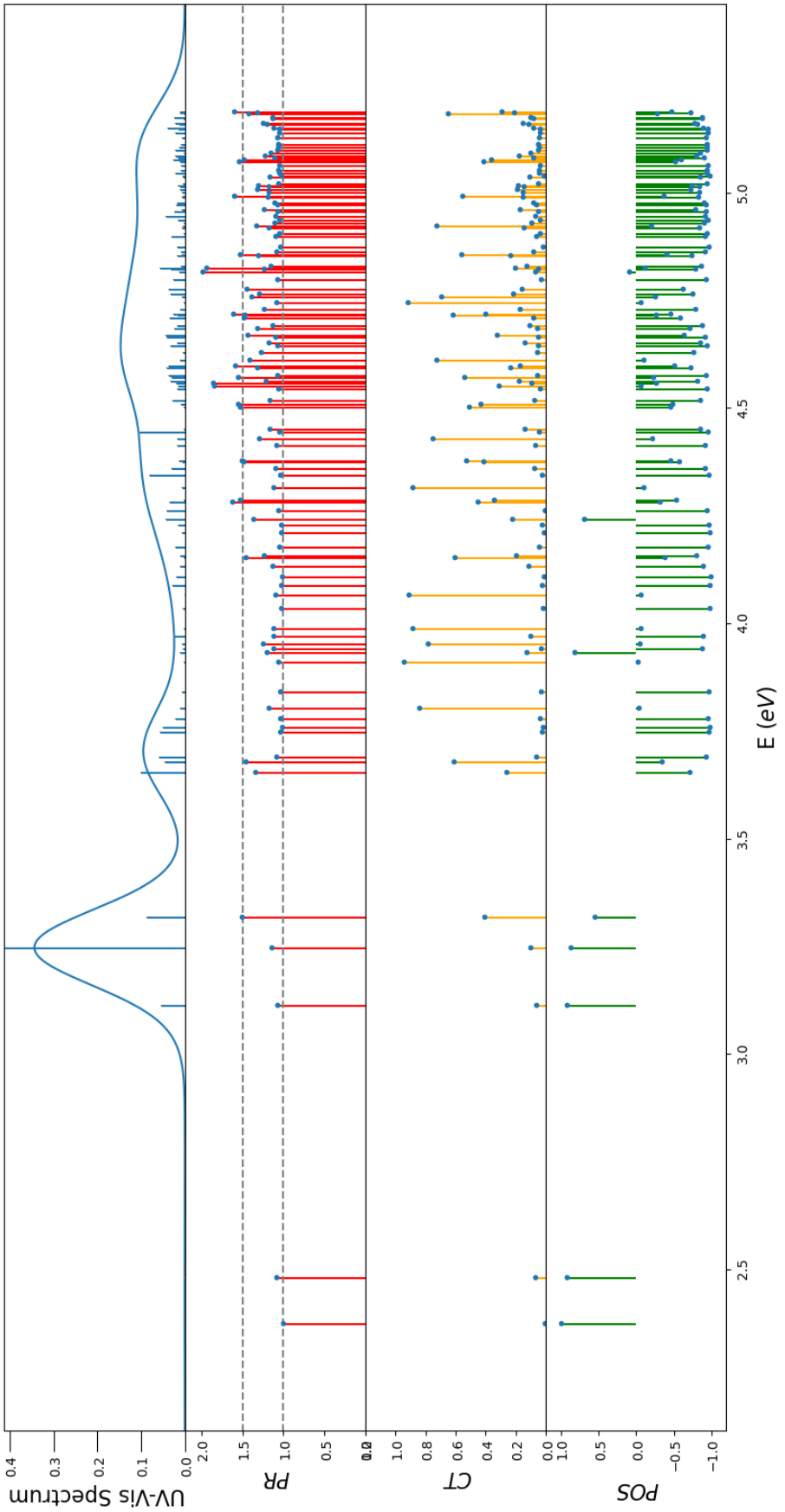

Figure A.18: **13D**

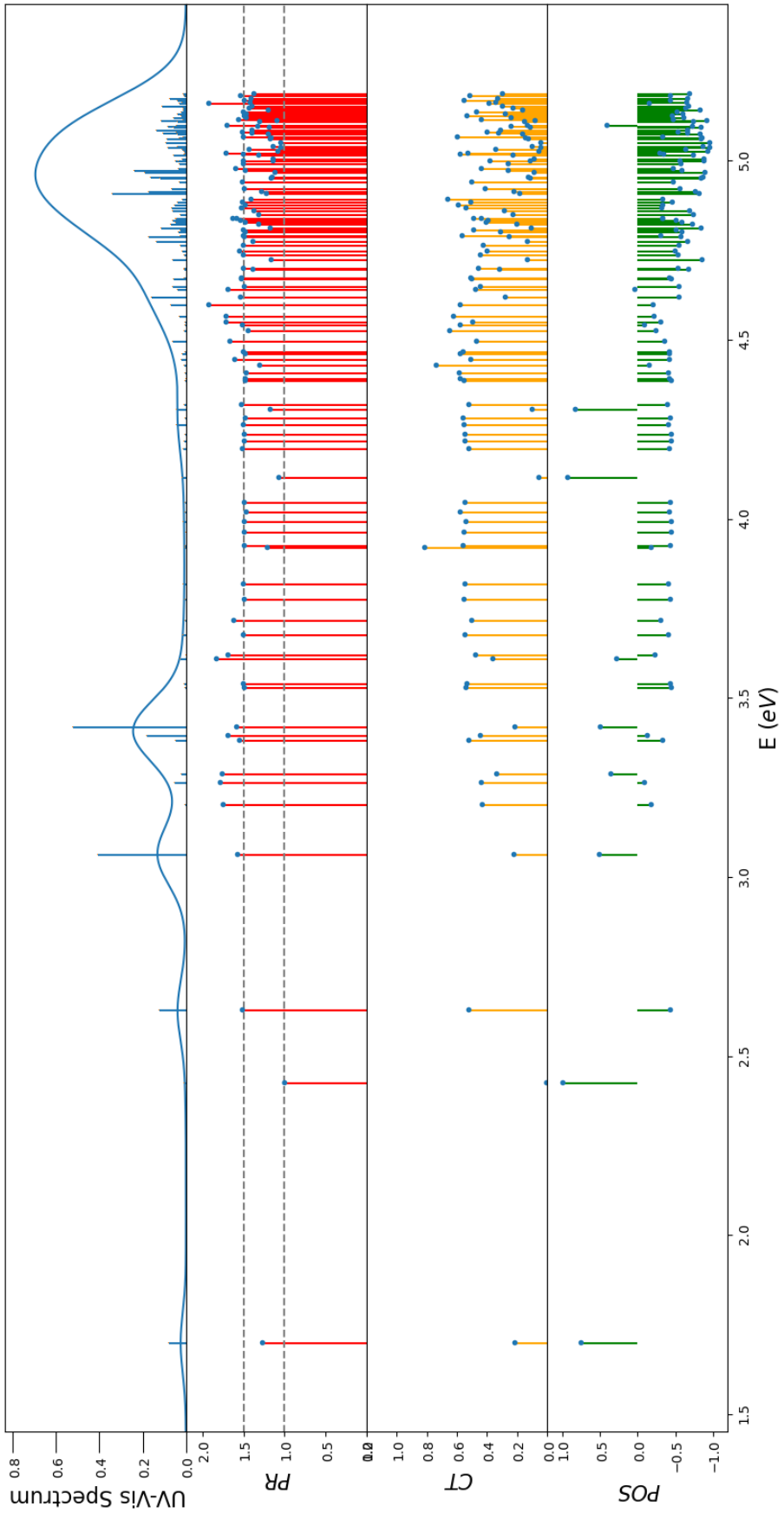

Figure A.19: **17D**

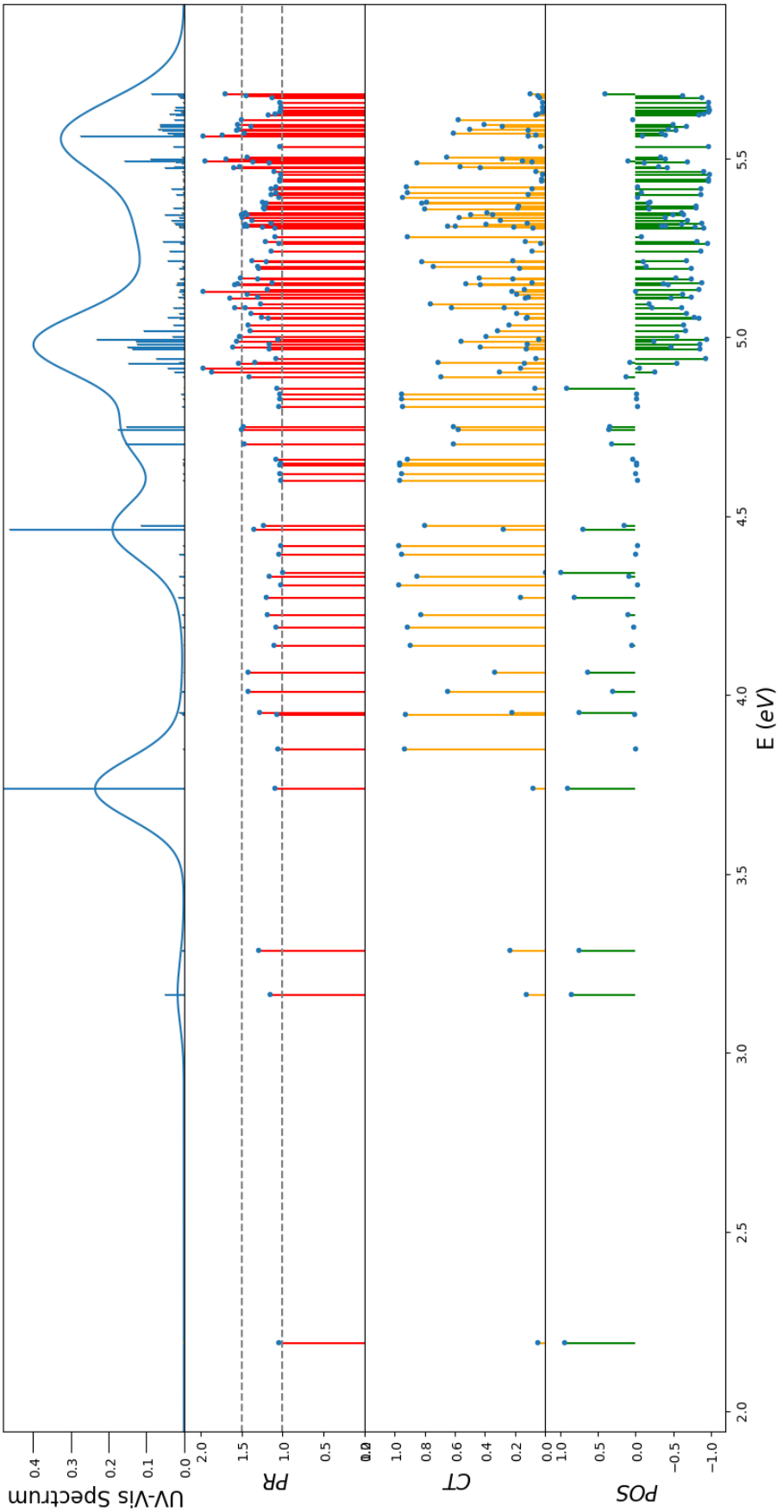

Figure A.20: **8P**

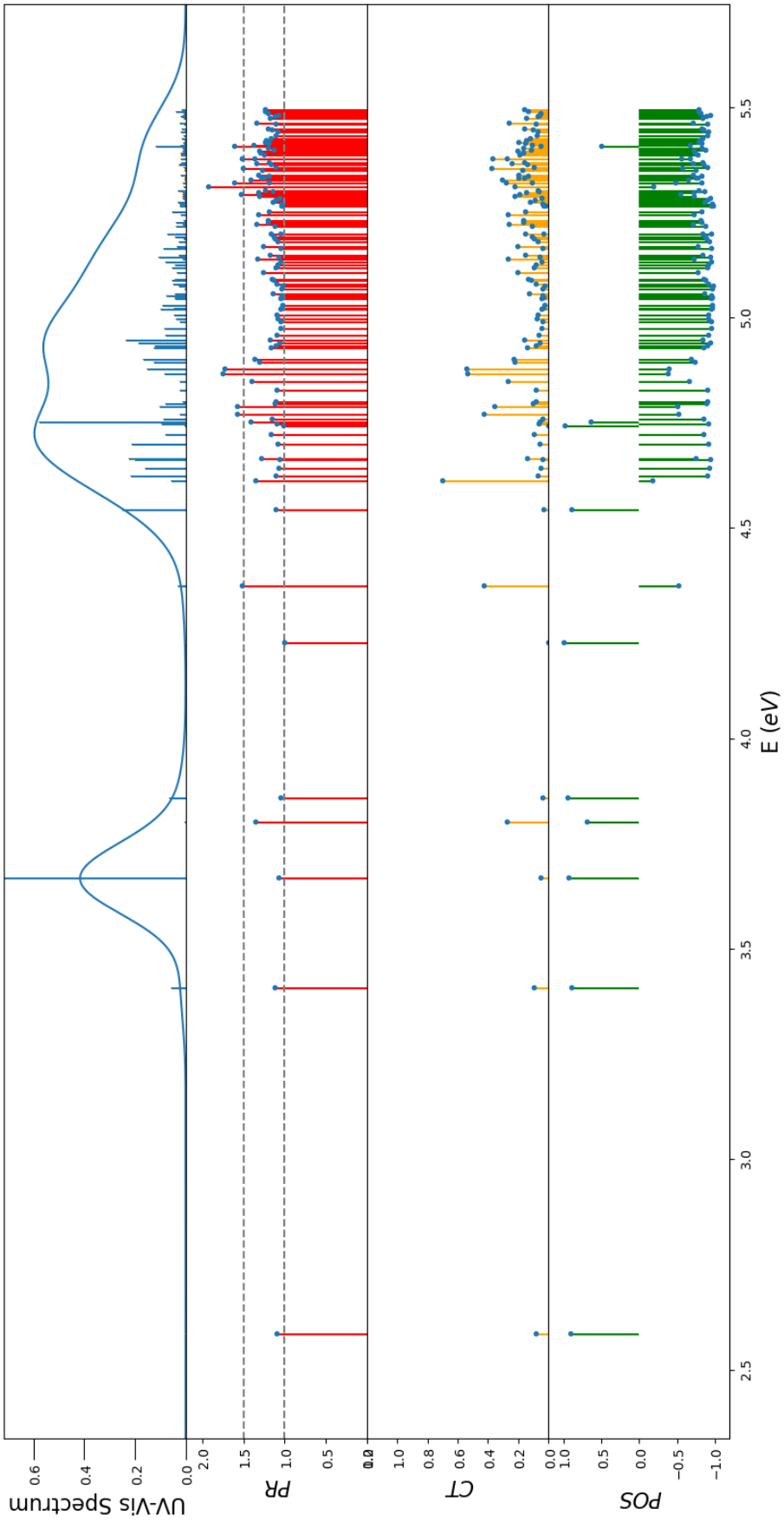

Figure A.21: **17P**

A.4 Dimers Descriptors Spectra

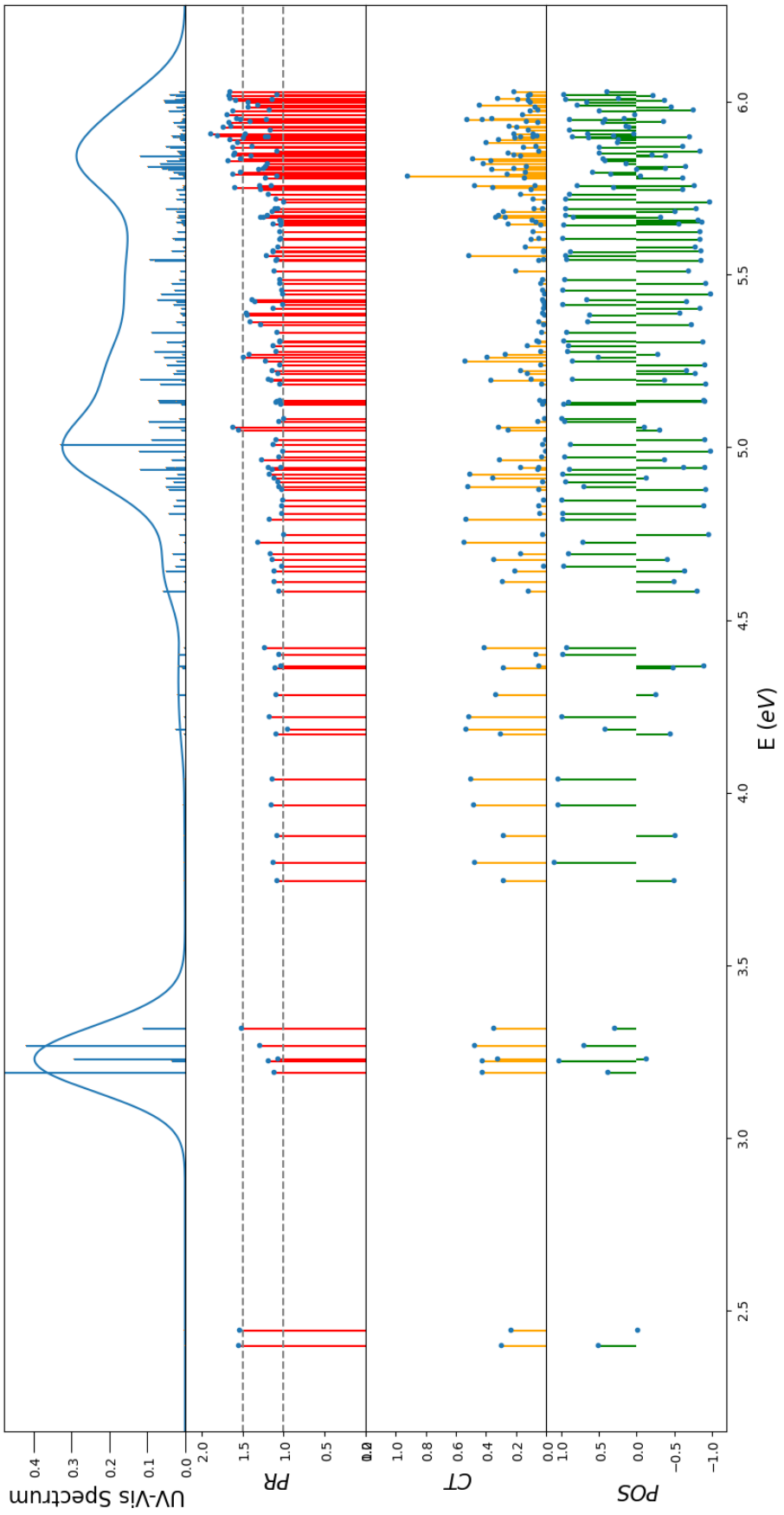

Figure A.22: **d.4D**, symmetric partition.

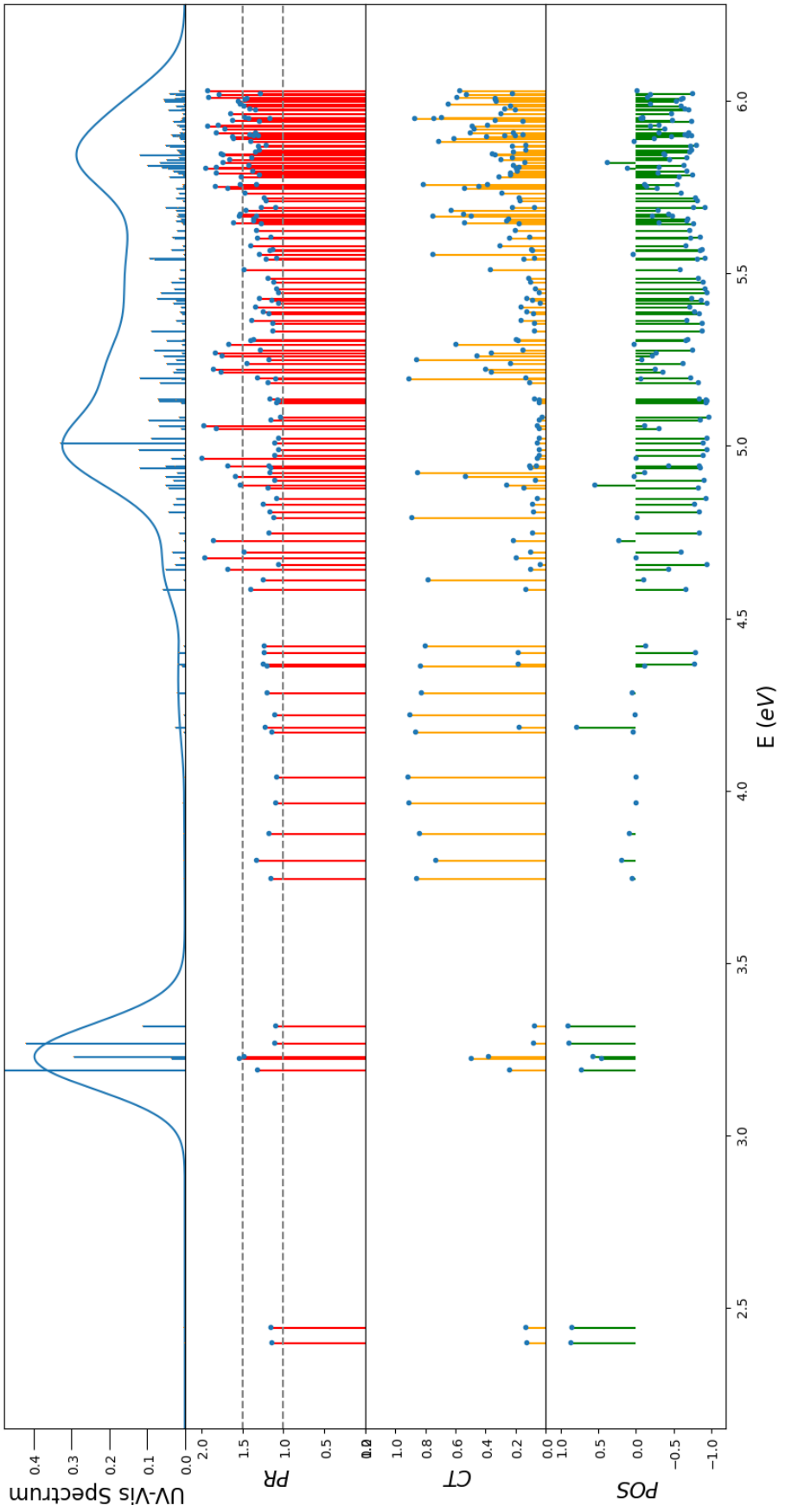

Figure A.23: **d.4D**, clusters to ligand partition.

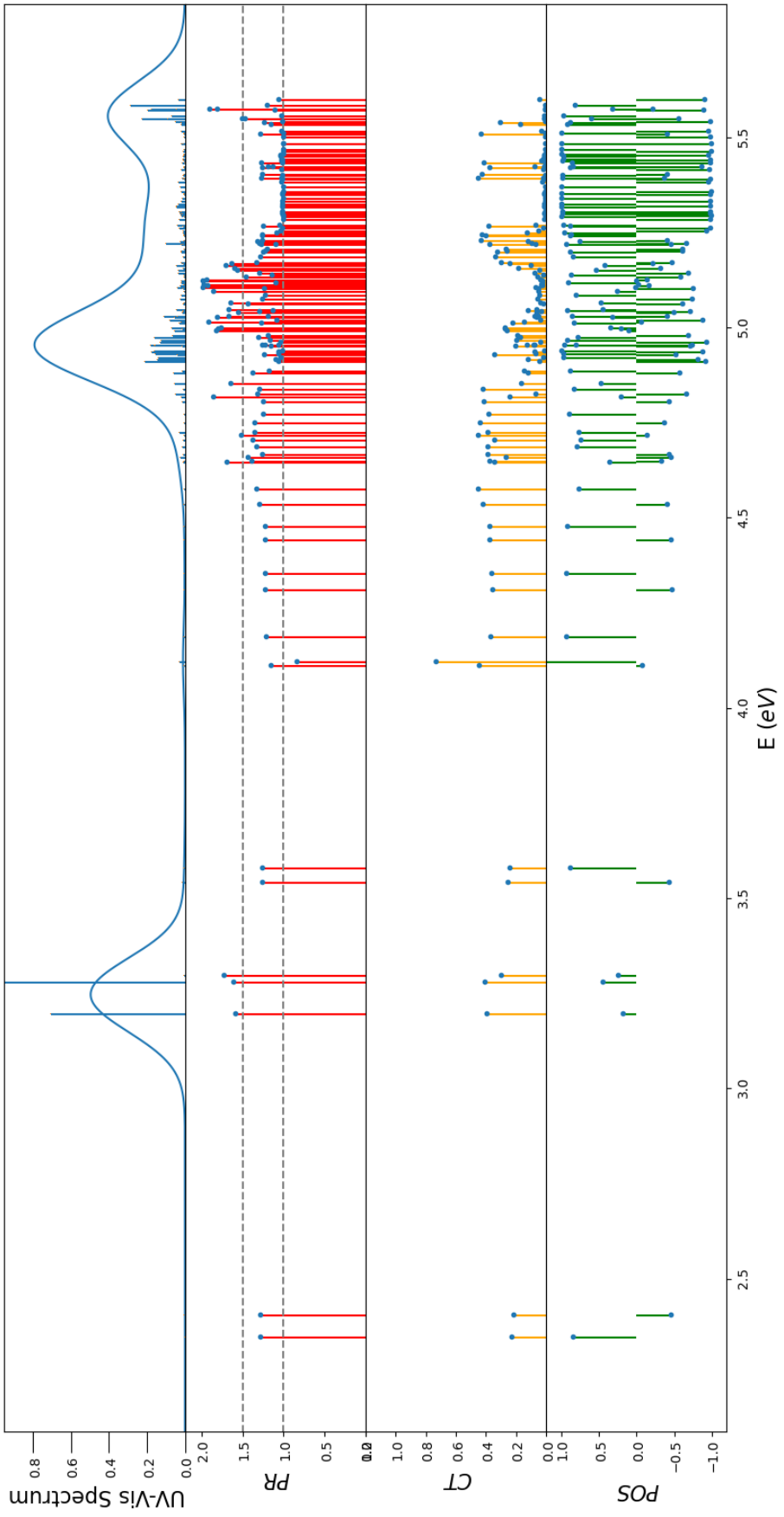

Figure A.24: **d.8D**, symmetric partition.

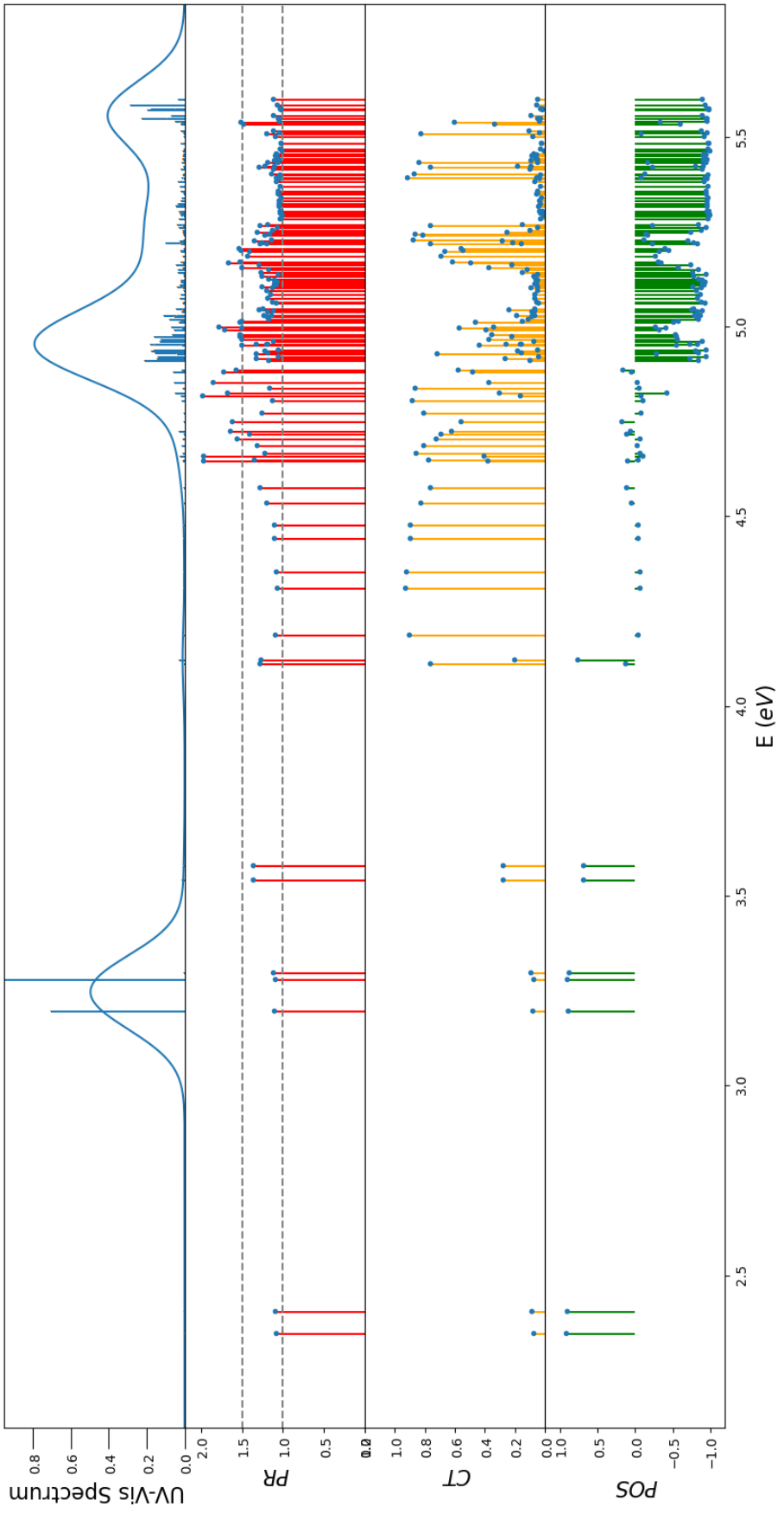

Figure A.25: **d.8D**, clusters to ligand partition.

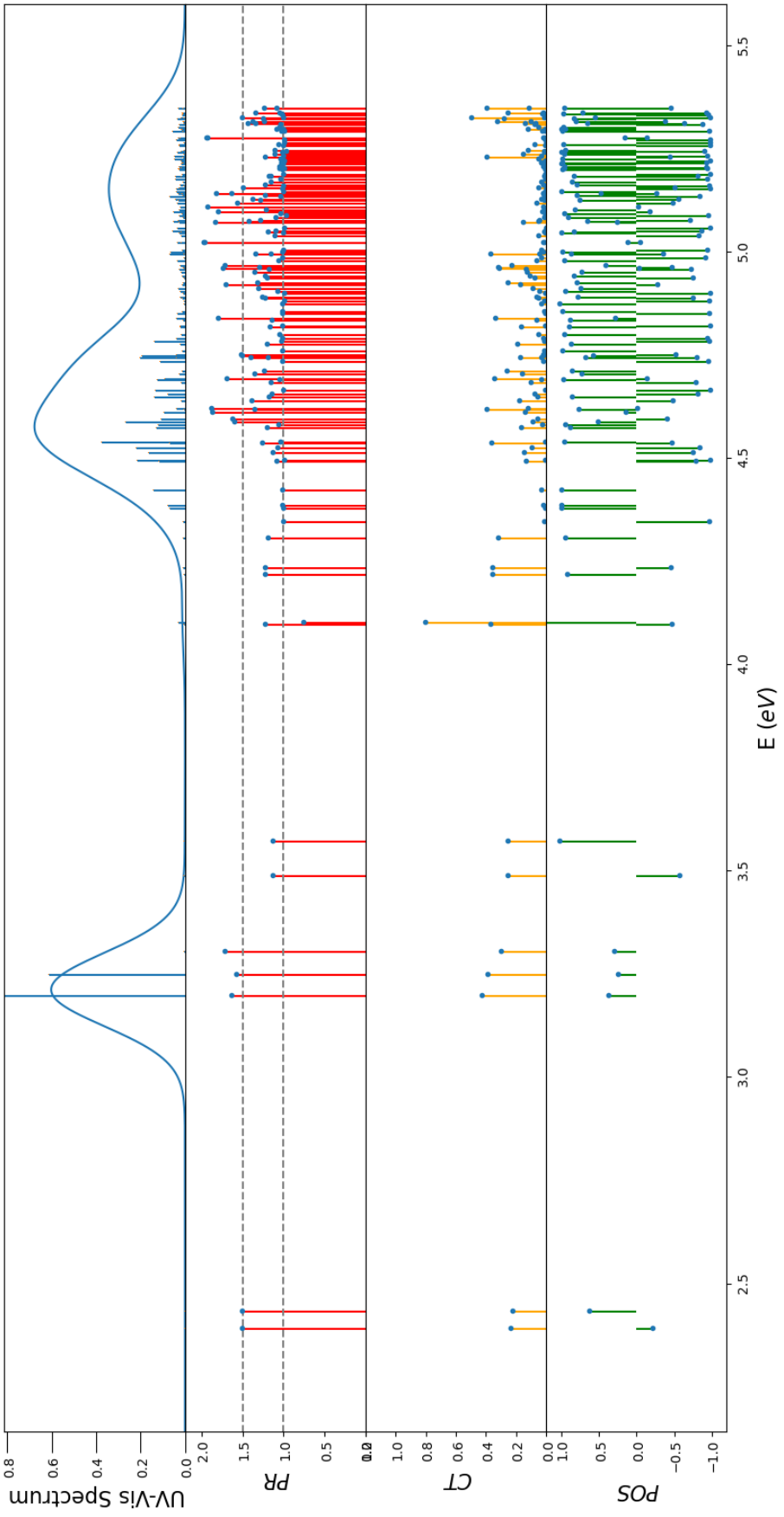

Figure A.26: **d.10D**, symmetric partition.

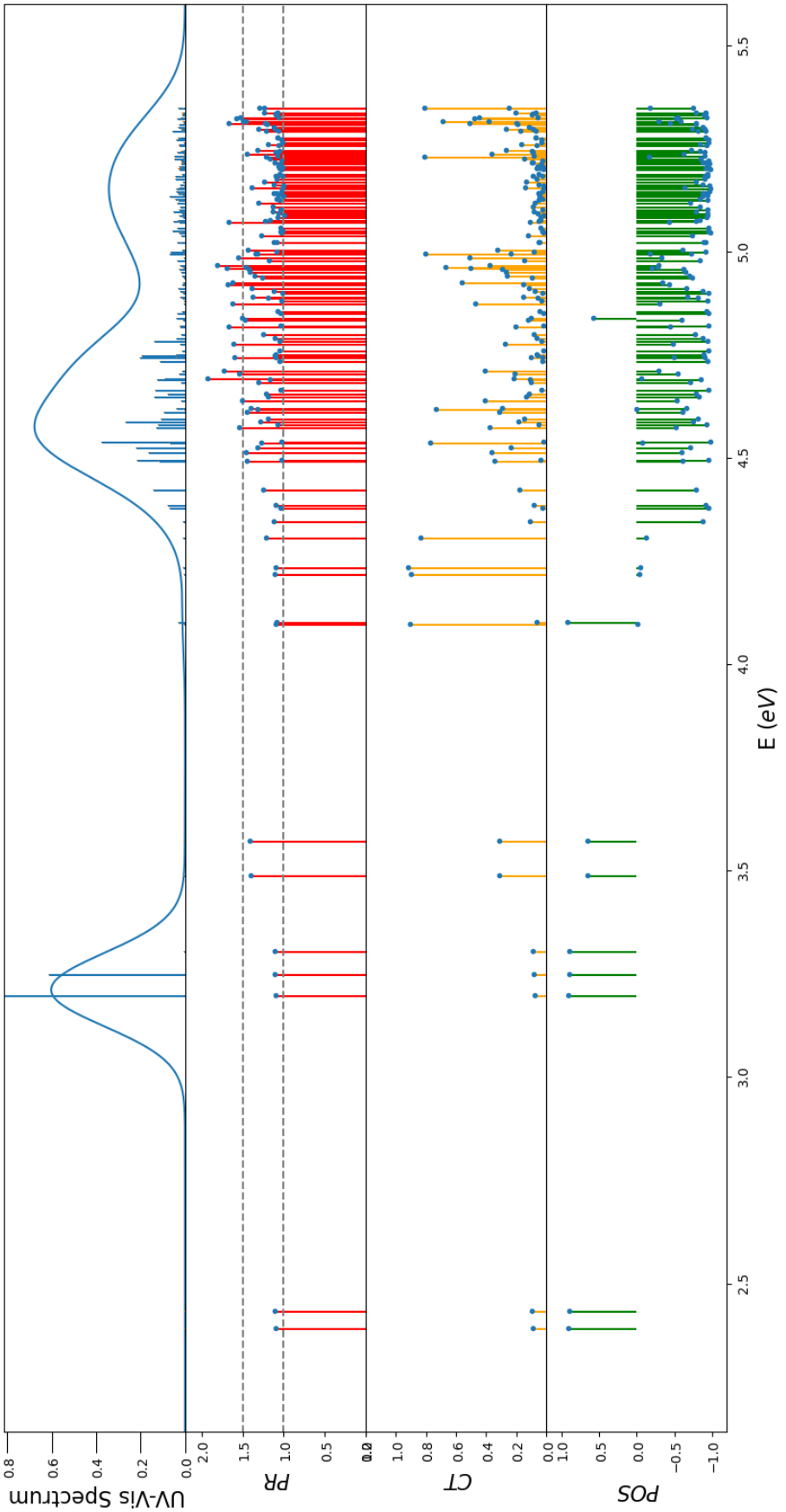

Figure A.27: **d.10D**, clusters to ligand partition.

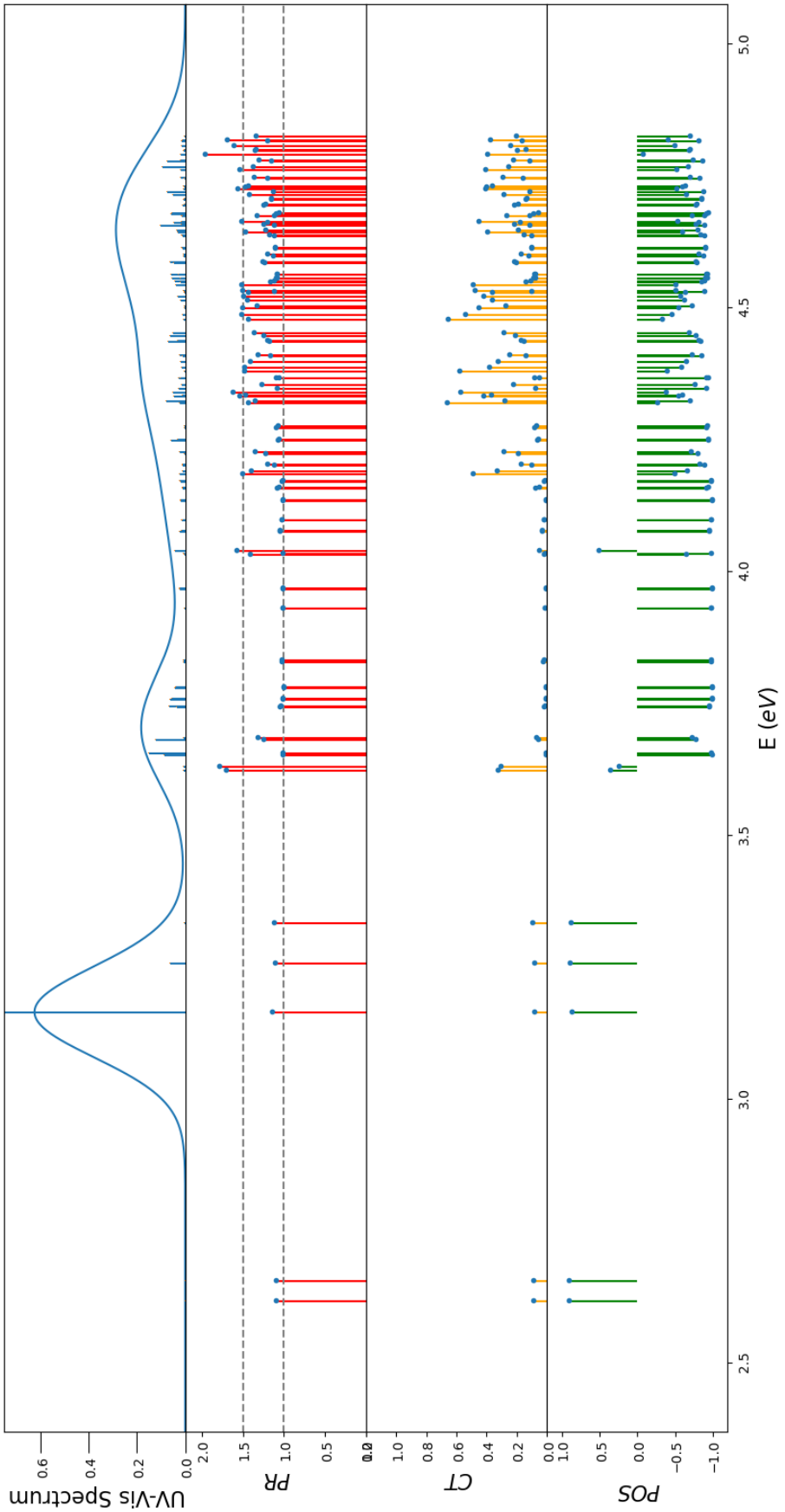

Figure A.28: **d.13D**, clusters to ligand partition.

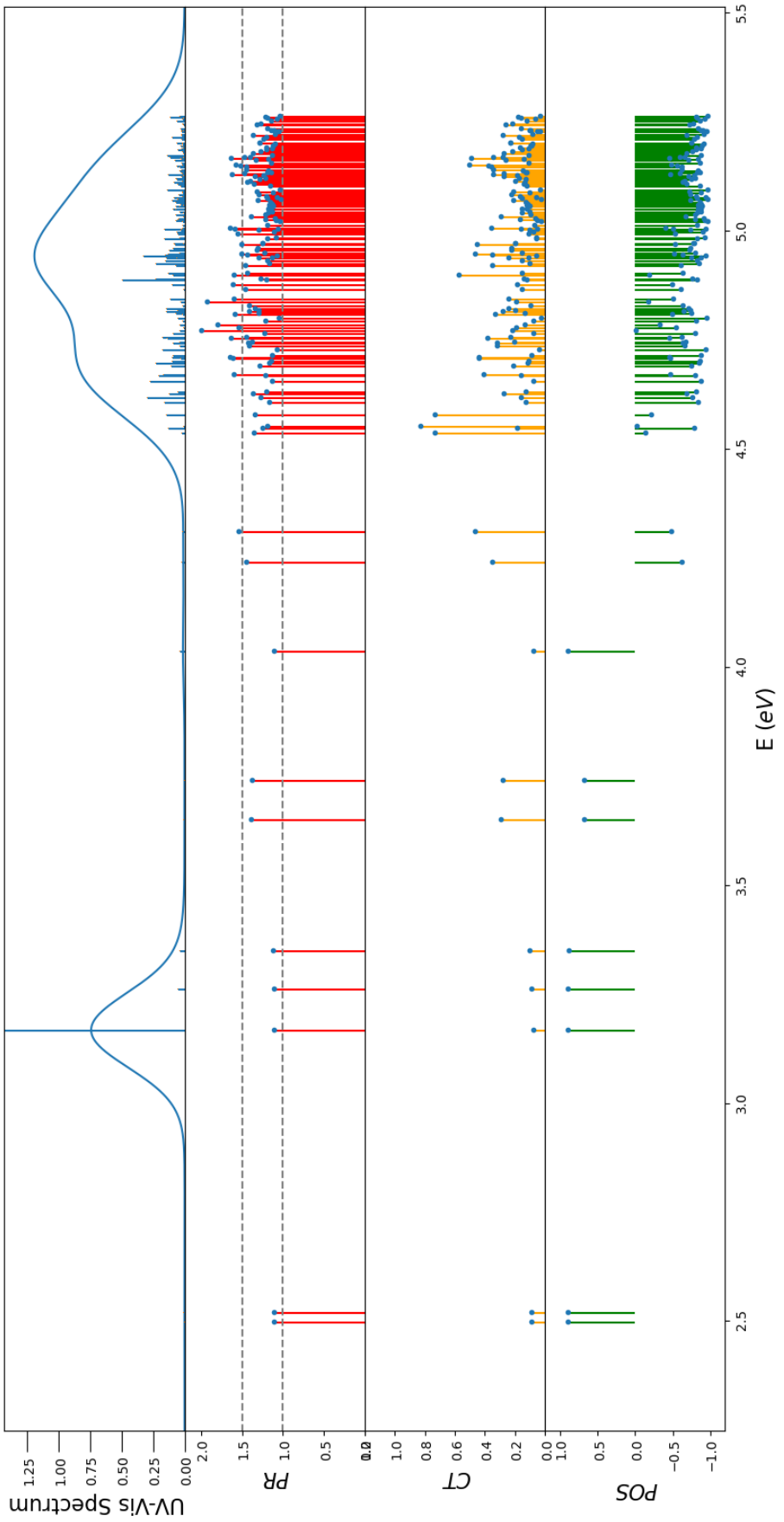

Figure A.29: **d.17D**, clusters to ligand partition.

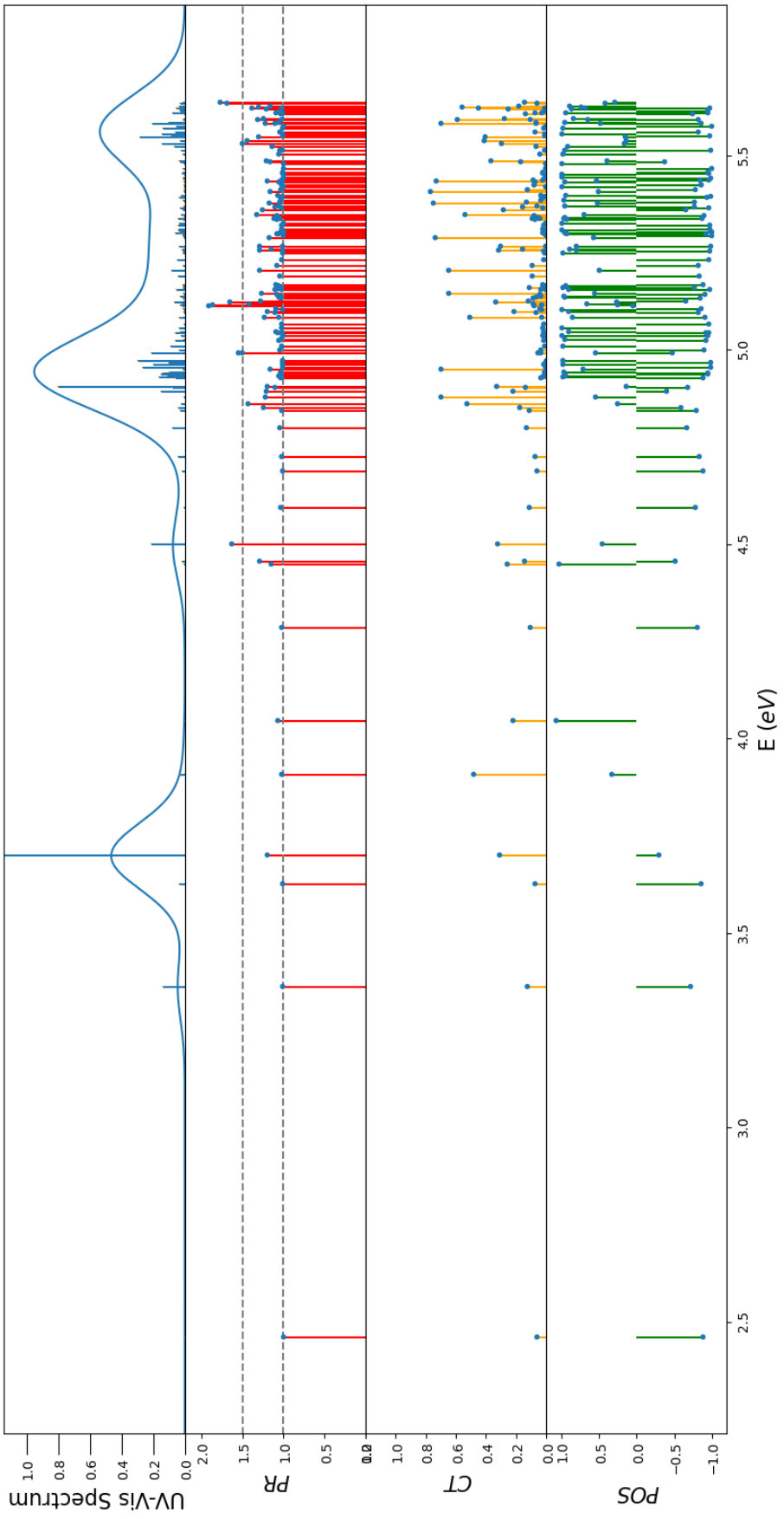

Figure A.30: **d.8P**, symmetric partition.

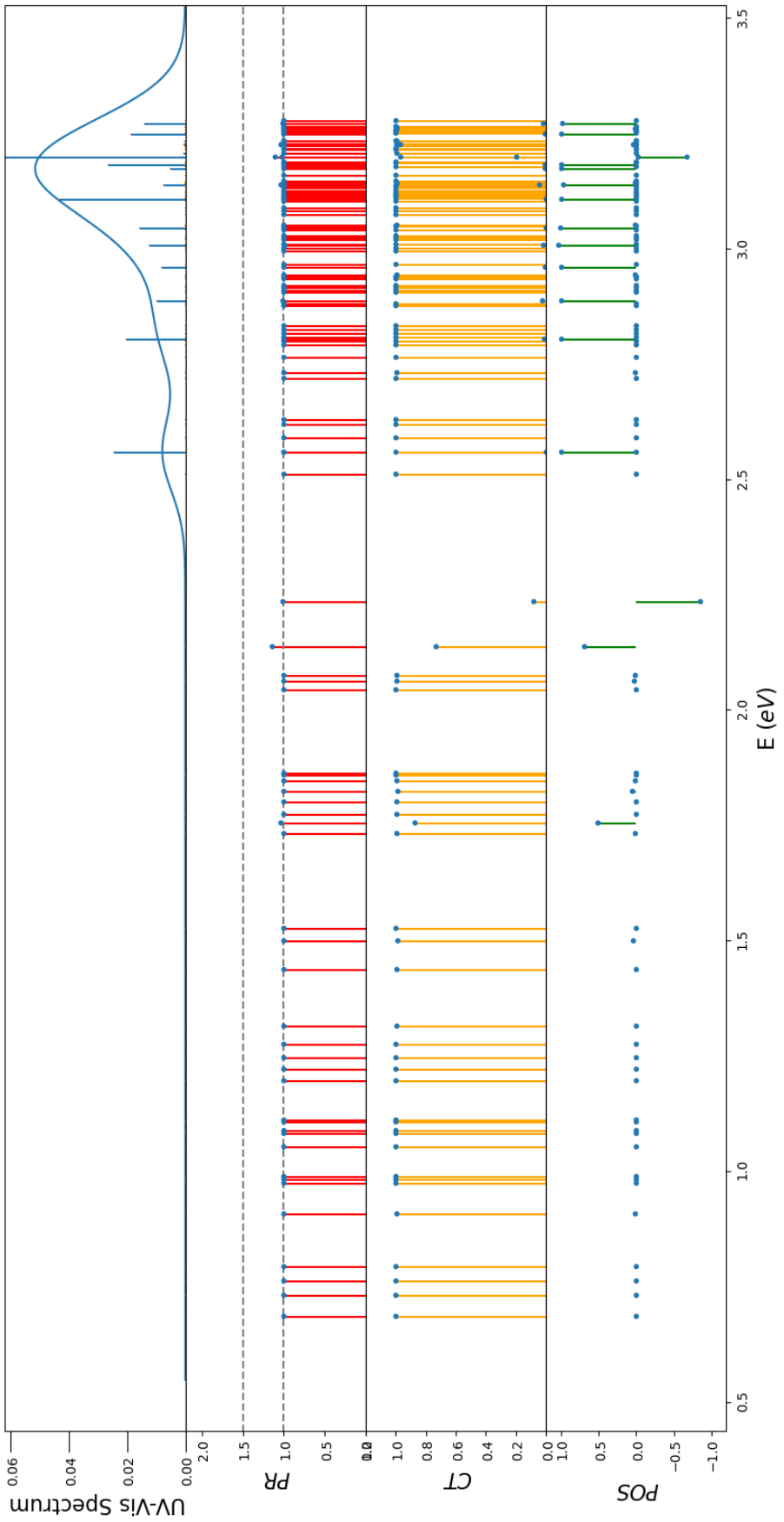

Figure A.31: **d.H**, symmetric partition.

A.5 Selected Molecular Orbitals

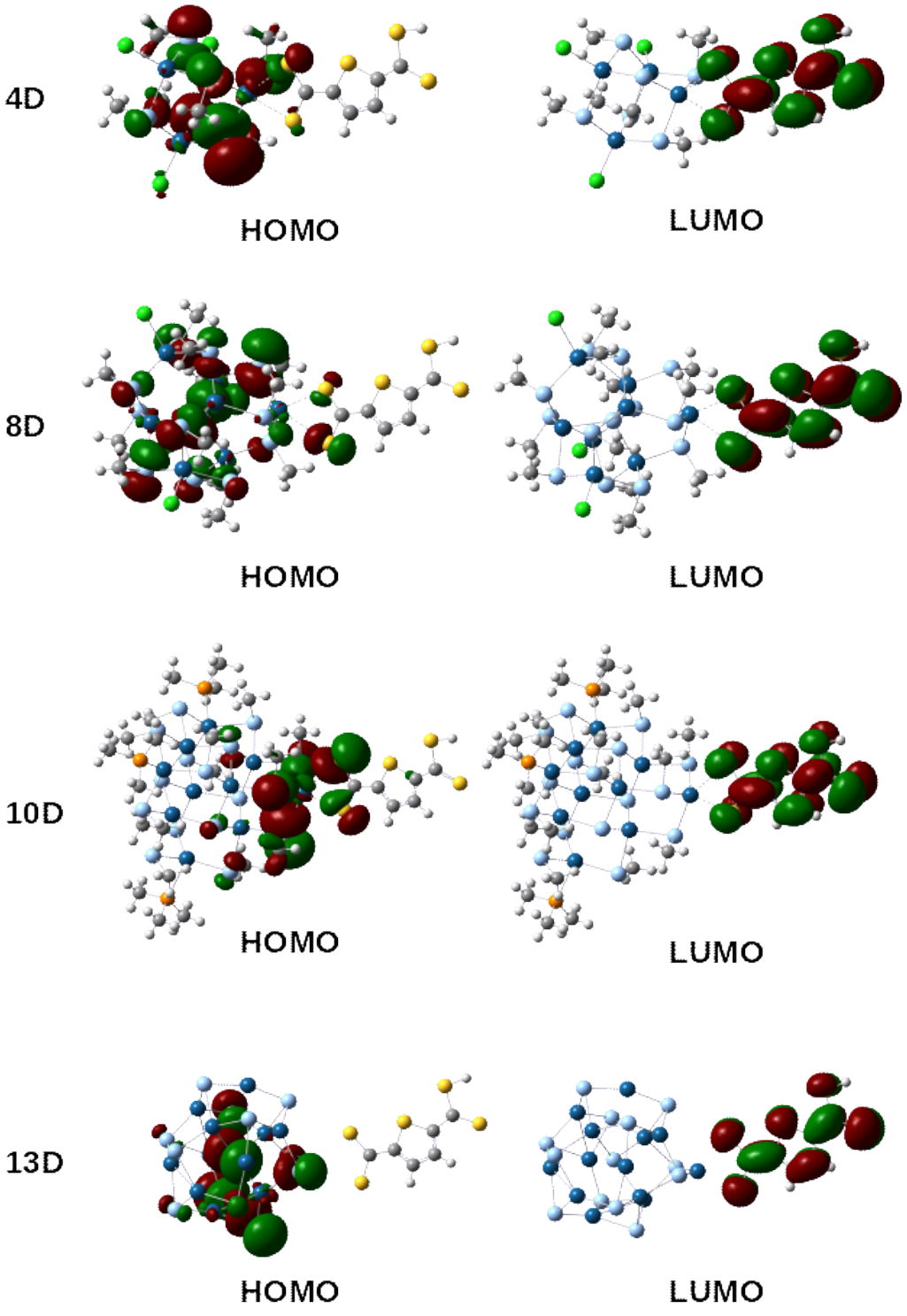

Figure A.32: First frontier orbitals of the monomers formed by inorganic cluster and DTMT ligand.

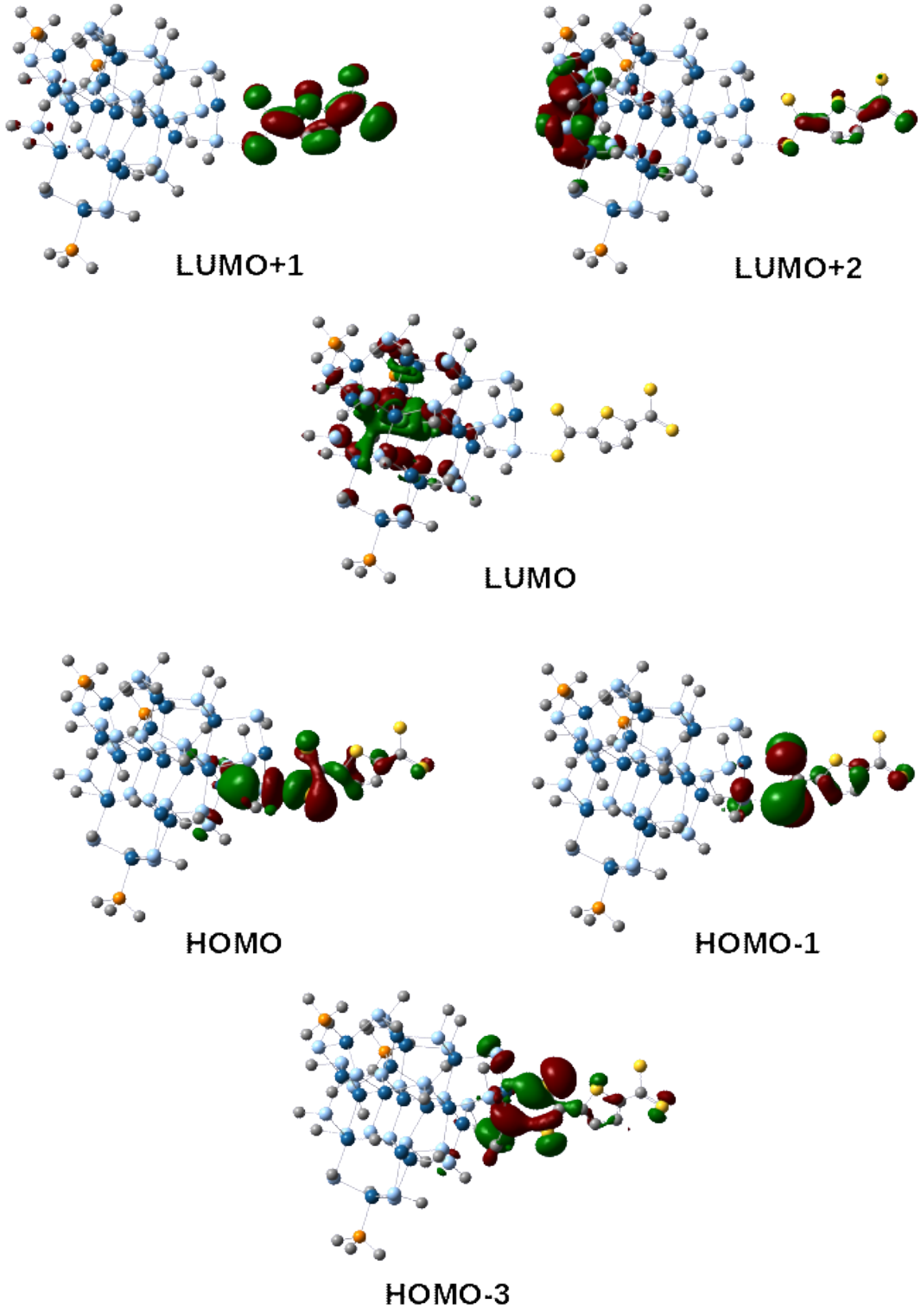

Figure A.33: Frontier orbitals of **17D** monomer. Orbitals separated by less than 40 meV are diplayed side-by-side.

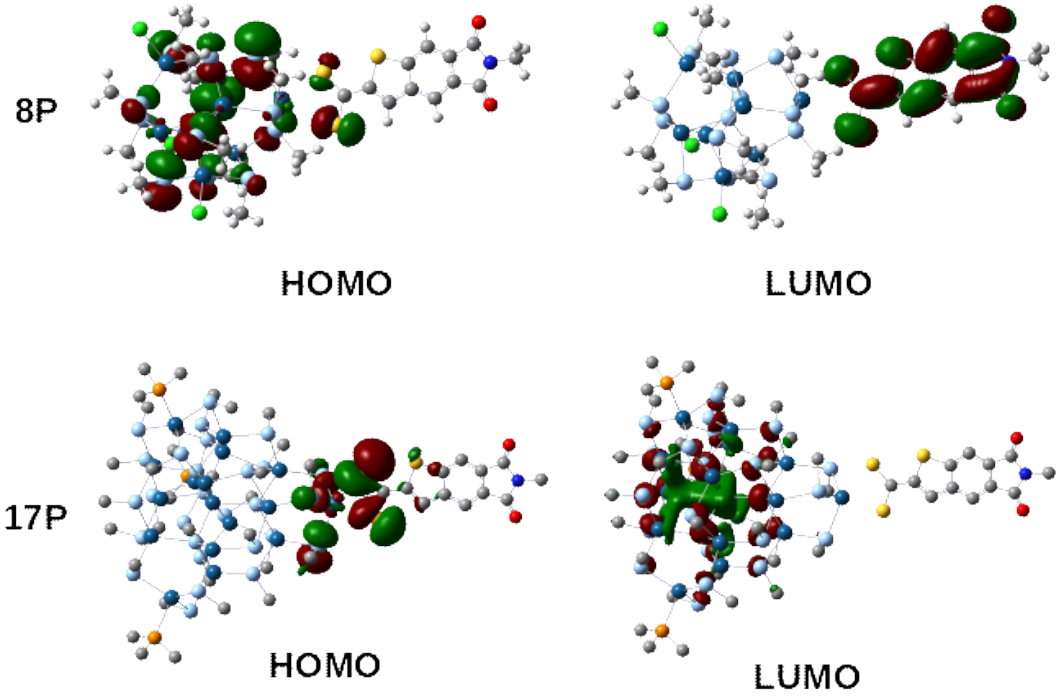

Figure A.34: First frontier orbitals of the monomers formed by inorganic cluster and PPNS ligand.

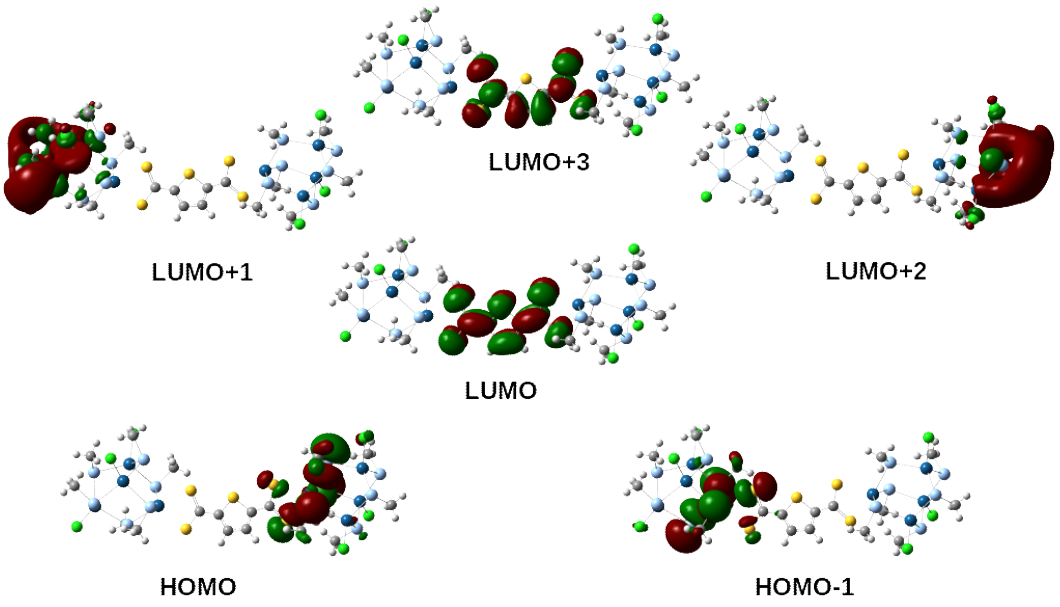

Figure A.35: Frontier orbitals of the **d.4D** dimer.

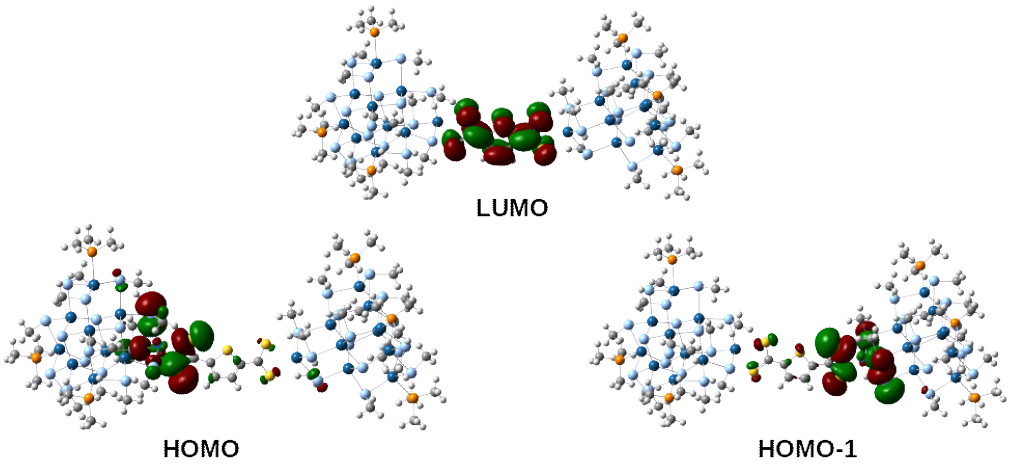

Figure A.36: Frontier orbitals of the **d.10D** dimer.

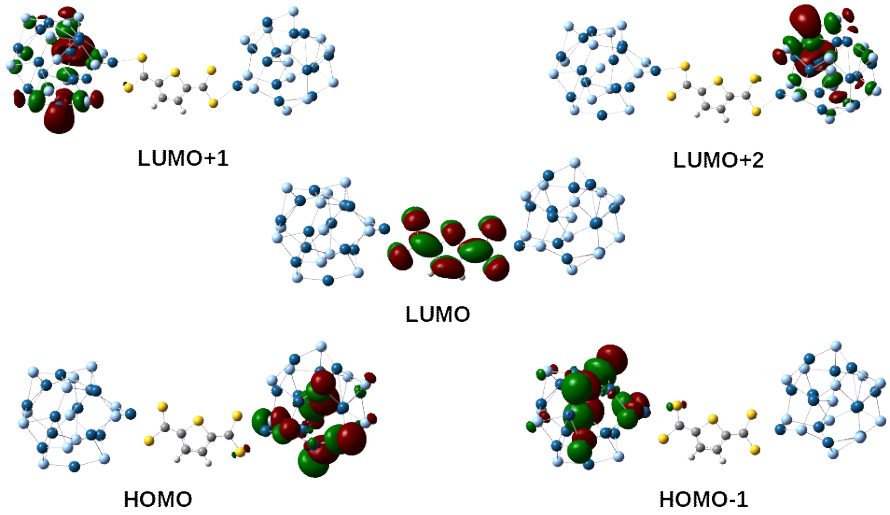

Figure A.37: Frontier orbitals of the **d.13D** dimer.

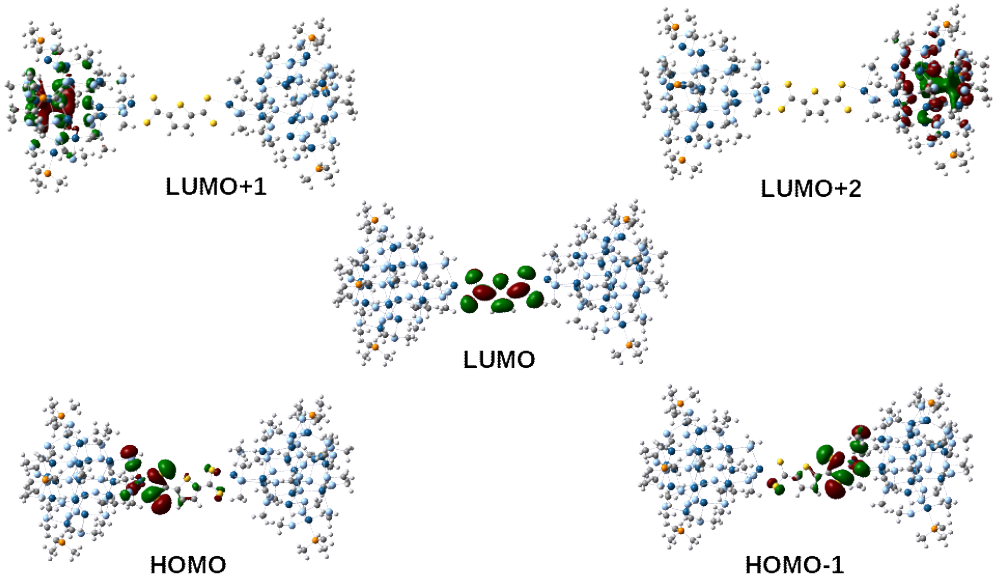

Figure A.38: Frontier orbitals of the **d.17D** dimer.

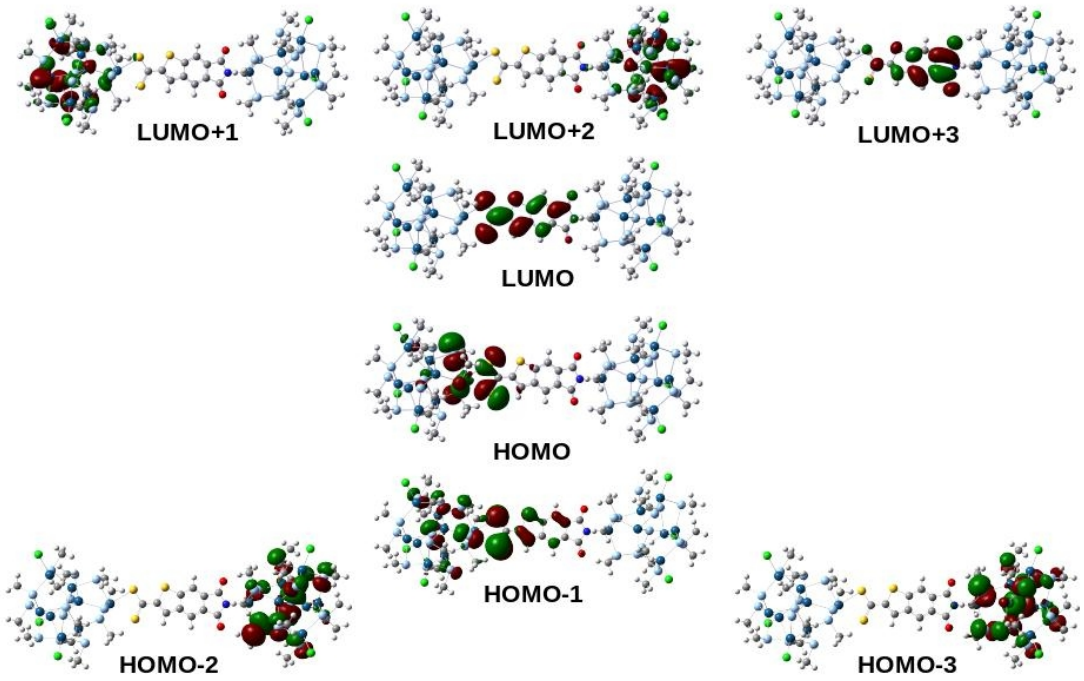

Figure A.39: Frontier orbitals of the **d.17D** dimer.

A.6 Selected NTOs

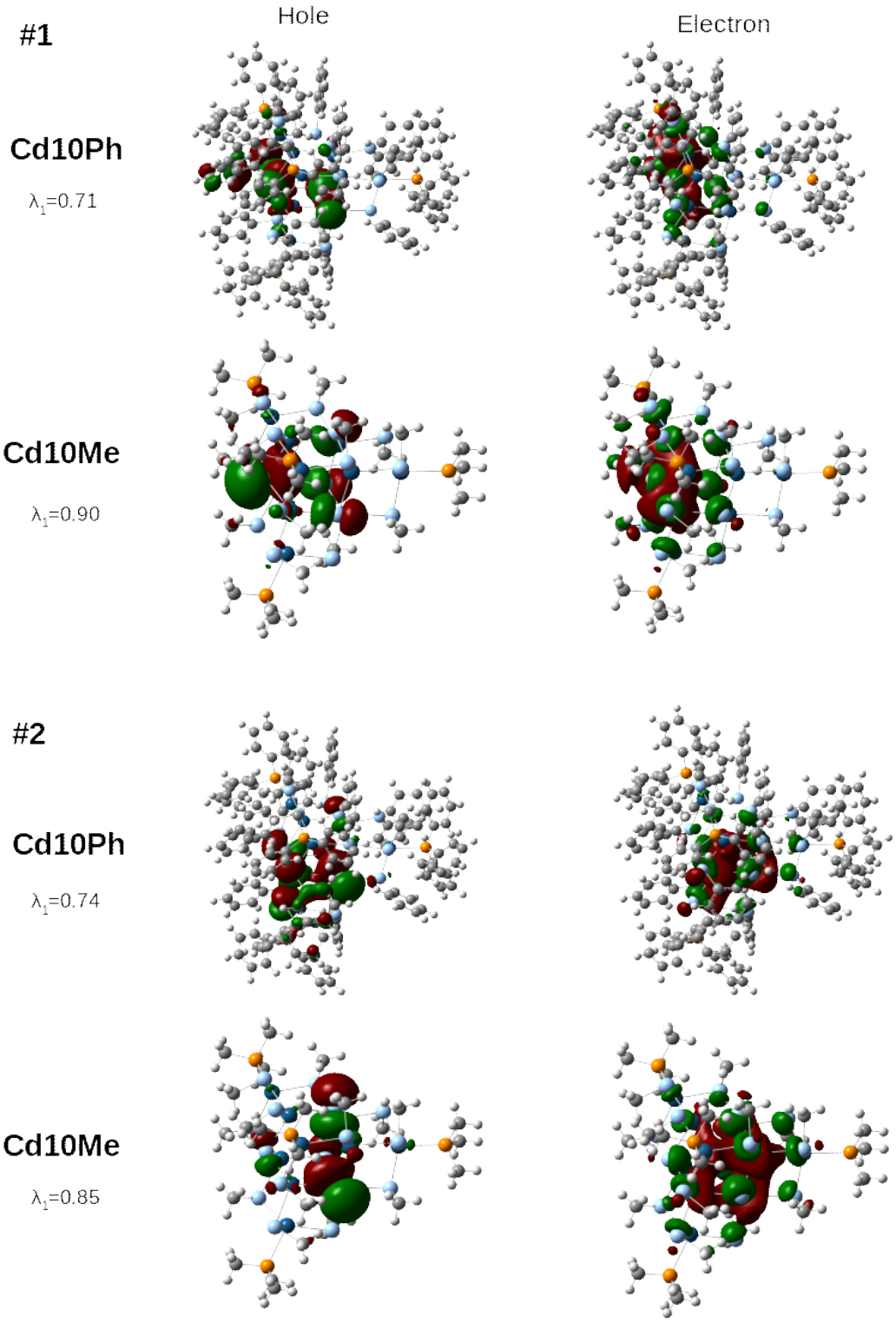

Figure A.40: Natural transition orbitals of the first two transition for **Cd10Ph** and **Cd10Me** clusters.

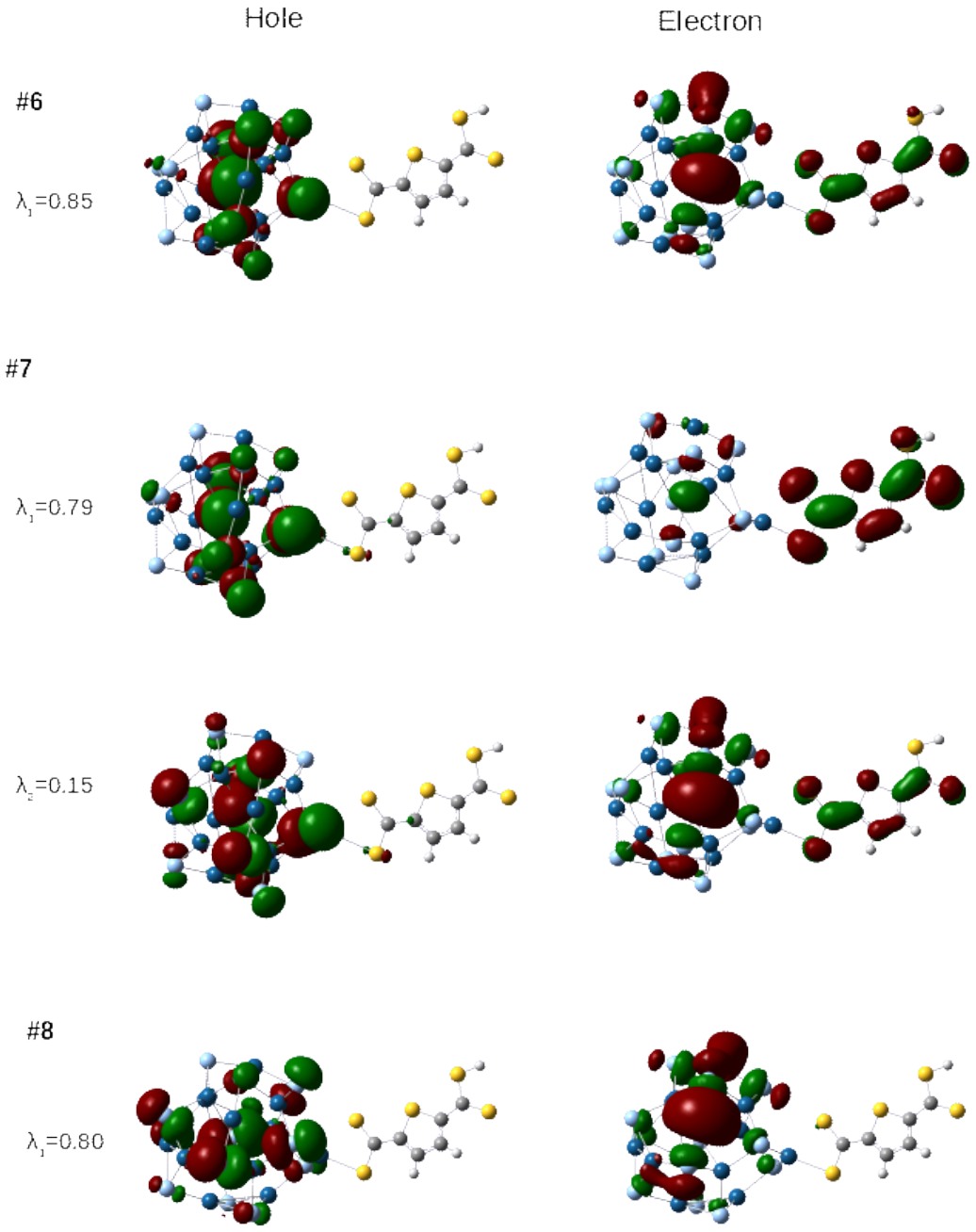

Figure A.41: Natural Transition orbitals (NTOs) of transitions 6 to 8 of monomer **13D**. The singular value (λ_i) of every couple is reported on the left, each row representing a couple of hole and electron orbitals